UNIVERSITY OF COPENHAGEN
FACULTY OF SCIENCE

PhD thesis

The phenomenological study on alternative black holes and dark matter distribution

Zhen Li

Advisors: Steen H. Hansen and Adriano Agnello

Submitted: March 31, 2024

This thesis has been submitted to the PhD School of The Faculty of Science, University of Copenhagen

Zhen Li, DARK, Niels Bohr Institute, University of Copenhagen
Jagtvej 128, 2200 Copenhagen N, Denmark

Publications related to this thesis

This thesis is based on the following single-author and first-author publications:

- *Scalar perturbation around rotating regular black hole: Superradiance instability and quasinormal modes,*
  Zhen Li, Phys.Rev.D, 107, 044013 (2023). arxiv: 2210.14062.
- *Superradiance and quasinormal modes of the gravitational perturbation around rotating hairy black hole,*
  Zhen Li, Phys.Lett.B, 841, 137902 (2023). arxiv: 2212.08112.
- *Energy extraction from rotating regular black hole via Comisso-Asenjo mechanism,*
  Zhen Li, Xiao-Kan Guo and Faqiang Yuan, Phys.Rev.D, 108, 044067 (2023). arxiv: 2304.08831.
- *Energy extraction via Comisso-Asenjo mechanism from rotating hairy black hole,*
  Zhen Li, Faqiang Yuan, Phys.Rev.D 108, 024039 (2023). arxiv: 2304.12553.
- *A phenomenological model for dark matter phase space distribution,*
  Zhen Li, Steen H. Hansen, MNRAS 529, 1877 (2024). arxiv: 2312.12304.

Abstract

Black holes and dark matter stand out as two of the most intriguing and mysterious subjects in modern physics. Significant progress has been made in understanding black holes through gravitational waves and imaging observations. However, due to the precision limitations of observations, we can not exclude the possibility of alternative black holes beyond general relativity. Moreover, general relativity itself faces challenges, such as the spacetime singularity problem. Therefore, there is a need for more phenomenological studies on alternative black holes, enabling potential comparisons with observations. Concerning dark matter, numerous outstanding simulations aim to address the distribution of dark matter by assuming the collisionless nature of dark matter particles. Several universal properties of dark matter halos have been observed. Unfortunately, a satisfactory theory to predict these properties is lacking. Consequently, there is a quest for a phenomenological model that can provide a unified description of the observed empirical laws in simulations and also inspire theoretical investigations.

In this thesis, we employ several phenomenological studies on both black holes and dark matter distributions.

We consider two alternative black holes: the rotating regular black hole and the rotating hairy black hole, corresponding to the violation of two theorems in general relativity, namely the singularity theorem and the no hair theorem, respectively. The scalar field was investigated around the rotating regular black hole, while the gravitational field was studied in the regime of the rotating hairy black hole. These investigations allow us to discuss the phenomenology of superradiance and quasinormal modes around these two alternative black holes. Additionally, we also study the energy extraction from these two alternative black holes via magnetic reconnection. The effects of the new parameters, which characterize the deviation from Kerr black holes, were presented, and the physical implications were also discussed.

For dark matter distribution, we propose and analyze a new phenomenological model of dark matter phase space distribution, which could semi-analytically provide NFW-like density profile and analytically give velocity magnitude as well as components distributions that closely align with simulation data. Particularly noteworthy is the ability of our model that could accurately capture radial velocity data across the entire velocity range and the lower velocity regime of tangential data. While certain discrepancies exist, our model demonstrates strong predictive performance in reproducing universal properties observed in simulations. These results suggest that our model may be relevant for describing the distribution of dark matter particles.

Dansk resumé

Sorte huller og mørkt stof skiller sig ud som to af de mest fascinerende og mystiske emner inden for moderne fysik. Der er gjort betydelige fremskridt med at forstå sorte huller gennem observationer af gravitationsbølger og billeddannelse. Dog på grund af præcisionsbegrænsningerne i observationerne kan vi ikke udelukke muligheden for alternative sorte huller ud over den generelle relativitetsteori. Desuden står den generelle relativitetsteori selv over for udfordringer, såsom singularitetsproblemet i rumtiden. Derfor er der behov for flere fænomenologiske studier af alternative sorte huller, der muliggør potentielle sammenligninger med observationer. Vedrørende mørkt stof sigter talrige fremragende simuleringer mod at adressere fordelingen af mørkt stof ved at antage mørkt stofs partiklers kollisionsløse natur. Adskillige universelle egenskaber ved mørkt stofhaloer er blevet observeret. Desværre mangler der en tilfredsstillende teori til at forudsige disse egenskaber. Som følge heraf er der en søgen efter en fænomenologisk model, der kan give en forenet beskrivelse af de observerede empiriske love i simuleringer og også inspirere teoretiske undersøgelser.

I denne afhandling anvender vi flere fænomenologiske studier både på sorte huller og mørkt stofs fordelinger.

Vi overvejer to alternative sorte huller: det roterende regelmæssige sorte hul og det roterende hårede sorte hul, der svarer til overtrædelse af to teoremer i den generelle relativitetsteori, nemlig singularitetsteoremet og ingen-hår-teoremet, henholdsvis. Skalarfeltet blev undersøgt omkring det roterende regelmæssige sorte hul, mens det gravitationelle felt blev undersøgt i regime for det roterende hårede sorte hul. Disse undersøgelser tillader os at diskutere fænomenologien af superradiance og kvasinormale tilstande omkring disse to alternative sorte huller. Derudover studerer vi også energiudvindingen fra disse to alternative sorte huller via magnetisk genforbindelse. Virkningerne af de nye parametre, der karakteriserer afvigelsen fra Kerr sorte huller, blev præsenteret, og de fysiske implikationer blev også diskuteret.

For mørkt stofs fordeling foreslår og analyserer vi en ny fænomenologisk model af mørkt stofs fasepladsfordeling, som kunne give en analytisk NFW-lignende densitetsprofil og hastighedsmagnitude samt komponentsfordelinger, der tæt matcher simuleringsdata. Især bemærkelsesværdig er vores models evne til nøjagtigt at fange radiale hastighedsdata på tværs af hele hastighedsområdet og det lavere hastighedsregime af tangentiale data. Mens visse uoverensstemmelser eksisterer, demonstrerer vores model stærk forudsigende præstation i reproduktion af universelle egenskaber observeret i simuleringer. Disse resultater antyder, at vores model kan være relevant for at beskrive fordelingen af mørkt stofs partikler.

Acknowledgements

I would like to thank my supervisors Steen H. Hansen and Adriano Agnello for giving me this opportunity to pursue my PhD. I really enjoy the time working with them. I wish to thank for their enthusiastic support and helpful guidance throughout my entire PhD journey. I also want to thank my colleagues at DARK for their unwavering support. It has been a privilege to work with such a dedicated group.

During my study exchange at the University of St Andrews, I had a great discussion with HongSheng Zhao, Keith Horne, Indranil Banik, Nicholas Boardman, Alfie Russell, and visitor Philip Mannheim. During my study exchange at the University of Zurich, I enjoyed working with Aurel Schneider, Jozef Bucko, and Timothée Schaeffer. I learned a lot from them.

I would also like to thank my collaborators and my friends Xiao-Kan Guo and Faqiang Yuan. Their impressive work and advice have improved my study a lot.

I am deeply grateful for the financial support from the China Scholarship Council. My entire PhD journey would not have been possible without their invaluable support. I also want to express my gratitude to DARK for financially supporting my PhD studies.

The life of studying abroad is not easy. I sincerely thank my Chinese friends ShanZhong Han, Yun Huang, ShiWen Yang, Qian Lv, Zhong Han, CunYang Li, Lei Li, JiaMei Lin, Jian Liu, XueZhi Zhuo, LingZhi Liu, ChunYu Lin, MeiRu Pan, LingYu Zhang, Xin Qian, Xin Li, Qing Gao, GuoZhen Ma, Ping Chang, and many others, for their accompany, foods, drinks, games, smiles, jokes, ... They make me feel at home in Denmark.

Thanks to my father, ZeGuang Li, my mother, XianQing Zhu, and my brother, Dong Li, for their endless encouragement and unconditional support. My family is a forever harbor to me. To my deeply loved grandmother, XiuFeng Zhu, I really want to share this moment with you. I hope you are surrounded by eternal serenity and joy in heaven. I miss you so much.

Last but not least, I wish to express my heartfelt and deepest thanks to my fiancée, JiangRong Liu, for her love, patience, and belief in me. You are my greatest blessing. You are not only my partner but also my biggest supporter and cheerleader. I LOVE YOU!

Contents

Chapter 1

Introduction

1.1 Current status and motivations for black hole phenomenology

We are currently experiencing a golden age in the study of black holes. For centuries, black holes remained purely theoretical concepts. However, recent breakthroughs, such as the first detection of gravitational waves in 2015 by the LIGO-Virgo Collaboration [1] and the first black hole image in 2019 by the Event Horizon Telescope [2], have confirmed their existence in our universe. Despite the success of general relativity (GR) as the best theory of gravity so far, it still faces significant theoretical and experimental challenges. One notable challenge is the spacetime singularity problem, which suggests spacetime incompleteness inside black holes and at the beginning of our universe [3, 4]. In these regimes, the laws of physics break down due to the infinite spacetime curvature, presenting a fundamental challenge. Another possible issue is the no hair theorem of black holes. The name "hair" is nothing but a property of the black hole. No hair theorem suggests that, besides mass, spin, and electric charge, no other properties can be observed outside the event horizon of the black hole [5, 6, 7, 8, 9]. All information is gone except for these three properties. With the existence of unknown dark energy and dark matter, it remains uncertain whether these mysterious substances contribute additional properties, or "hair" to black holes.

To address these challenges, various alternative gravity theories and black hole metrics have been proposed. Instead of delving into more theoretical alternative gravity theories, a pragmatic approach involves working with alternative black hole spacetime metrics. By utilizing these metrics, we can investigate their effects on observations and thereby test these alternative black holes. In response to the spacetime singularity problem and no hair theorem, researchers have put forth the concepts of regular [10, 11, 12, 13, 14, 15, 16] and hairy black holes [17, 18] along with their rotating counterparts. These alternative black holes provide avenues for studying deviations from the predictions of GR and examining their potential impact on observational data. As we explore these alternatives, we move closer to a comprehensive understanding of black holes and gravity. Given the current precision of gravitational wave measurements and black hole imaging, providing a definitive answer about black holes remains challenging. To study the properties of black holes, more advanced and diverse observations are necessary. Therefore,

a comprehensive study of black hole phenomenology is crucial to offer additional observational insights.

In future gravitational wave observations, it is anticipated that the quasinormal modes will be detected in the final phase (or ringdown phase) of two merging black holes [19, 20, 21, 22]. In this phase, the spacetime can be seen as a gravitational perturbation field propagating around a black hole. Because fields or matter will more or less fall into the black hole and also propagate to infinity, the perturbation fields will oscillate with a damped amplitude. Quasinormal modes refer to the frequencies of a damped perturbation field around a black hole. The quasinormal modes are directly determined by the black hole properties. Hence, quasinormal modes play a pivotal role in distinguishing black holes. It is important to investigate the quasinormal modes of alternative black holes so that we can compare them with upcoming gravitational wave observations of quasinormal modes. This will allow us to test the possibility of black holes beyond GR.

Quasinormal modes are not limited to gravitational perturbations. Scalar and vector fields can also exhibit quasinormal modes when they evolve as perturbation fields around a black hole. Furthermore, perturbation fields could be enormously amplified through the so-called superradiance phenomena. When the frequency of the perturbation fields is within a certain range, the fields will become unstable in the rotating black hole spacetime, and they could be scattered by the rotating black hole with amplified amplitude. This instability is caused by the interaction between the fields and the black hole spacetime. Superradiance is governed by the properties of the black hole as well as the perturbation fields. Thus, this mechanism provides a valuable tool to explore unknown fields around black holes. As an example, a ultralight scalar field, whose Compton wavelength is comparable to the event horizon size of a rotating black hole, will become unstable and the superradiance phenomena will occur. As a result, a superradiant scalar field cloud will form around the rotating black hole, which is usually called a gravitational atom. This superradiant scalar cloud is actually a quasinormal condensate state of scalar fields that can emit gravitational waves [23, 24].

Beyond gravitational waves, the non-gravitational high-energy phenomenology around black holes is particularly intriguing. These phenomena offer an independent means of detecting the physics surrounding black holes. The magnetic fields in the vicinity of black holes are exceptionally strong. The magnetic lines could be anti-parallel in the equatorial plane of a rotating black hole, which could easily cause magnetic reconnection. This process will emit an amount of energy from the magnetic fields. Since the magnetic fields are maintained by the rotation energy of a black hole, it is equally correct to say that magnetic reconnection can potentially extract energy from the rotating black holes. A novel study shows that magnetic reconnection happening within the ergosphere can indeed extract significant amounts of energy from a rotating black hole [25]. The nature of different black hole models influences the energy extraction process, leading to high-energy phenomenology that can be observed to distinguish between various black hole models.

In this thesis, we will delve into the phenomenology of quasinormal modes, superradiance, and magnetic reconnection around both rotating regular black holes and rotating hairy black holes.

1.2 Current status and motivations for dark matter distributions

As mentioned in the above section, dark matter remains one of the most mysterious phenomena observed in our universe. Dark matter comprises about 25% of the energy density of the current universe and is approximately five times more abundant than normal matter [26]. Its elusive nature, interacting only through gravitational forces, poses a significant challenge for direct detection and study in space and underground experiments [27, 28, 29]. Dark matter plays a crucial role in governing galaxy formation and influencing the destiny of the cosmos. It is also essential to understand the distribution of dark matter halos in galaxies. Additionally, the velocity distribution of dark matter is of great importance for direct detection experiments [30, 31, 32, 33], especially if dark matter interacts with normal matter through non-gravitational portals. Assuming dark matter is collisionless, cosmological simulations emerge as the most promising approach to experimentally address questions about its distribution.

Several universal properties, such as density profiles, have been discovered through various simulation programs [34, 35, 36, 37, 38, 39, 40]. However, despite these advancements, a satisfactory theory capable of predicting the properties observed in simulations is still lacking [41, 42, 43, 44, 45, 46, 47, 48]. The distribution of dark matter particles is believed to satisfy the phase space collisionless Boltzmann equation, yielding Maxwell-Boltzmann distributions—a concept known as the standard halo model. However, this model contradicts simulation data in several aspects, such as density profiles and velocity distributions [45, 46, 47, 48]. This discrepancy may stem from the highly nonlinear nature of self-gravitating systems [43, 44], such as dark matter halos. Addressing this challenge requires a more comprehensive understanding of the complex interactions within these systems.

Consequently, adopting a pragmatic approach, a phenomenological model seems to be a valuable avenue given the current status. On one hand, such a model could serve as a practical tool for describing simulation data. On the other hand, it has the potential to fuel motivation and inspiration for the development of more rigorous theoretical models. A phenomenological model might manifest through a single function, elucidating aspects such as density profiles (e.g., NFW profile [34]) or velocity distributions (e.g., generalized Maxwell-Boltzmann distribution [46]). However, a more plausible and comprehensive approach for a phenomenological model would involve predicting a multitude of universal properties observed in simulation data. In this context, a phenomenological phase space distribution emerges as a logical choice. Such a distribution not only includes empirical laws but also facilitates deductions of various properties, thereby maintaining internal consistency. The integration of these empirical laws into a phenomenological phase space distribution holds the potential to inspire and guide theoretical investigations.

We have proposed a phenomenological model for the phase space distribution of dark matter. This model potentially leads to an NFW-like density profile, velocity distribution, and other properties that align with simulation data. However, it is important to note that there are some discrepancies with the existing data, which need confirmation through further simulations.

1.3 Thesis outline

In the upcoming chapters, Chapters 3 and 4 will focus on the phenomenology of alternative black holes, while Chapter 5 will delve into the study of a new phenomenological model of dark matter distributions. We now outline the structure of the remaining chapters in this thesis.

Chapter 2 will serve as an introduction to the theoretical background relevant to this thesis, providing readers to comprehend the concepts discussed in subsequent chapters.

In Chapter 3, we will explore the phenomena of superradiance and quasinormal modes associated with alternative black holes. Specifically, we will investigate the scalar field around rotating regular black holes and gravitational perturbations around rotating hairy black holes. Superradiance will be studied using the matching-asymptotic method, while quasinormal modes will be analyzed using the continued fraction method. The impact of new parameters of alternative black holes on these two phenomenology will be thoroughly examined and discussed.

Moving on to Chapter 4, we will discuss the energy extraction from alternative black holes through the newly proposed magnetic reconnection (Comisso-Asenjo mechanism). Our study will explore how the energy extraction process is influenced by the rotation of regular black holes and hairy black holes, as well as other parameters.

In Chapter 5, we will present and discuss a new phenomenological model of dark matter phase space distributions. We will calculate analytical properties such as density profile, anisotropy, velocity distributions, and compare velocity components distributions with simulation data. The fitting results will be illustrated and discussed.

Chapter 6 will summarize the key results and findings of this thesis. We will also explore possible ways to enhance the study and discuss future prospects.

Chapter 7 will present the appendix, focusing on the error estimation of the approximation method used in Chapter 2, the special functions used in this thesis, and the contour plots of the MCMC samples used in Chapter 5. The aim is to provide a comprehensive understanding of the methodology employed in this study.

Chapter 2

Theoretical background

It is always helpful to enhance the understanding of a discussion by providing some theoretical background at the beginning. As introduced in the introduction, our research related to the alternative black holes which go beyond the two well-known theorems in GR. Therefore, we will begin by showing the rotating black holes predicted by GR, specifically the Kerr black hole. Subsequently, we will present a brief introduction on these two theorems. We will also illustrate the collisionless Boltzmann equation for describing the distributions of dark matter. Additionally, we will show the Maxwell-Boltzmann distribution, i.e., the standard halo model, which is an important solution to the collisionless Boltzmann equation.

2.1 Kerr black hole

The Kerr black hole is an exact solution to Einstein's equations, describing a stationary axisymmetric spacetime, or a rotating black hole. In Boyer-Lindquist coordinates, the metric for the Kerr black hole can be written as:

$$\begin{aligned} ds^2 = &-\left[\frac{\Delta - a^2\sin^2\theta}{\Sigma}\right]dt^2 + \frac{\Sigma}{\Delta}dr^2 + \Sigma d\theta^2 \\ &- 2a\sin^2\theta\left[1 - \frac{\Delta - a^2\sin^2\theta}{\Sigma}\right]dtd\phi \\ &+ \sin^2\theta\left[\Sigma + a^2\sin^2\theta\left(2 - \frac{\Delta - a^2\sin^2\theta}{\Sigma}\right)\right]d\phi^2 \end{aligned} \tag{2.1}$$

where $\Delta = r^2 - 2Mr + a^2$ and $\Sigma = r^2 + a^2\cos^2\theta$. It only has two parameters, the black hole mass M and spin $a = J/M$ with J is the total angular momentum of black hole. Kerr black hole has two horizons that could be obtained by solving equation $\Delta = 0$, which gives us

$$r_+ = M + \sqrt{M^2 - a^2} \tag{2.2}$$

$$r_- = M - \sqrt{M^2 - a^2} \tag{2.3}$$

r_+ and r_- are usually called event (outer) and inner horizon respectively. Unlike the Schwarzschild black hole, the Kerr black hole has an ergosphere and ergoregion,

which refers to the region lying between the radius r_{s+} and r_{s+} given by

$$r_{s+} = M + \sqrt{M^2 - a^2 \cos^2 \theta} \tag{2.4}$$

$$r_{s-} = M - \sqrt{M^2 - a^2 \cos^2 \theta} \tag{2.5}$$

these two radius are obtained by making the metric time component $g_{tt} = 0$. r_{s+} and r_{s+} are dependent on the polar angle θ. Inside the ergosphere, an observer is force to move and cannot remain static because the spacetime itself is also rotating. An observer could escape from the ergoregion to infinity since it is outside the event horizon. The angular velocity of a Kerr black hole is defined as

$$\Omega_H = \frac{a}{2Mr_+} = \frac{a}{r_+^2 + a^2} \tag{2.6}$$

2.2 Singularity theorem and no hair theorem in GR

The singularity is the spacetime region where the curvature of spacetime is infinite, and all physical laws thus break down. The singularity theorem is a robust theorem in GR proved by Hawking, Penrose, and others [3, 4]. They have demonstrated that a singularity must exist in spacetime when the following conditions are satisfied,

- Chronology of time, i.e., there is no close time-like geodesic, or time travel.
- GR is right.
- Strong energy condition holds.
- There is matter or energy exist in the spacetime.

With the above conditions, they proved that a geodesic can only be extended for a limited duration as measured by the observer moving along it, leading to the existence of a singularity [49]. In the case of the Kerr black hole, the singularity is a ring rather than a point observed from an Euclidean coordinates.

A hair of a black hole refers to a parameter in the spacetime metric that could be observed externally. The no hair theorem does not imply that there are no parameters observable outside a black hole, instead, it asserts that all stationary black hole metrics in GR can be fully determined by only three independent parameters: mass, spin, and electric charge. Beyond these three, no other distinctive features, or hair, exist in stationary black holes according to GR [5, 6, 7, 8, 9]. This theorem also implies that all other information, apart from these three parameters, disappears after an object falls into a black hole.

2.3 Collisionless Boltzmann equation and standard halo model

The observations of galaxy cluster collisions suggest that dark matter particles can pass through each other without collisions [50, 51, 52]. Therefore, a dark matter halo is considered a collisionless system, which can be described by the collisionless Boltzmann equation (CBE),

$$\frac{df}{dt} = \frac{\partial f}{\partial t} + \vec{v} \cdot \nabla f - \nabla\phi \cdot \frac{\partial f}{\partial \vec{v}} = 0 \tag{2.7}$$

where $f(\vec{x}, \vec{v}, t)$ represents the phase space distributions, and ϕ denotes the mean gravitational potential. The CBE is derived from the phase space continuity equation or Liouville's theorem. The dark matter halo can be considered to be in a steady state, i.e., $\frac{\partial f}{\partial t} = 0$. Then for the steady-state solutions of CBE, we have the famous Jeans theorem:

The steady-state solution of the CBE depends solely on the phase-space coordinates through integrals of motion. Equivalently, any function of these integrals is a steady-state solution of the CBE.

For a spherical isotropic system, the binding energy $\epsilon = \phi - \frac{1}{2}mv^2$ serves as the sole integral of motion, implying that f is a function of ϵ only. A solution for f corresponding to the Maxwell-Boltzmann distribution can be derived,

$$f(\epsilon) \propto e^{\epsilon/\epsilon_0} \tag{2.8}$$

where ϵ_0 is a normalization parameter. This phase space distribution is usually called standard halo model (SHM). To determine the corresponding density profile, we need to solve the Poisson equation, in spherical coordinates,

$$\frac{d}{dr}(r^2 \frac{d\phi}{dr}) = -4\pi G r^2 \rho(r) \tag{2.9}$$

$$\rho(r) = \int f(\vec{v}, r) d\vec{v} = 4\pi \int_0^\phi f(\epsilon)\sqrt{2(\phi - \epsilon)} d\epsilon \tag{2.10}$$

which give us

$$\rho(r) \propto \frac{1}{r^2} \tag{2.11}$$

However, this density profile could not match the observed density in the simulation, which typically follows $\rho(r) \propto 1/r$ in the inner region and $\rho(r) \propto 1/r^3$ in the outer region of the dark matter halo [34]. This discrepancy may be attributed to the spherical isotropic assumption of the system. In addition, the SHM usually predicts more particles at the high velocity tails in the velocity distributions [45, 46, 47, 48]. Anyway, these issues have motivated physicists to explore alternative possibilities for the dark matter phase space distribution.

Chapter 3

Superradiance and quasinormal modes of alternative black holes

This chapter is built upon the content of two single-author papers:

- **Scalar perturbation around rotating regular black hole: Superradiance instability and quasinormal modes**
  Author: **Zhen Li**
  Published in Phys.Rev.D, 107, 044013 (2023). arxiv: 2210.14062.

- **Superradiance and quasinormal modes of the gravitational perturbation around rotating hairy black hole**
  Author: **Zhen Li**
  Published in Phys.Lett.B, 841, 137902 (2023). arxiv: 2212.08112.

3.1 Scalar perturbation around rotating regular black hole

Abstract: Black holes provide a natural laboratory to study particle physics and astrophysics. When black holes are surrounded by matter fields, there will be plenty of phenomena which can have observational consequences, from which we can learn about the matter fields as well as black hole spacetime. In this work, we investigate the massive scalar field in the vicinity of a newly proposed rotating regular black hole inspired by quantum gravity. We will especially investigate how this nonsingular spacetime will affect the superradiance instability and quasinormal modes of the scalar filed. We derive the superradiant conditions and the amplification factor by using the matching-asymptotic method, and the quasinormal modes are computed through continued fraction method. In the Kerr limit, the results are in excellent agreements with previous research. We also demonstrate how the quasinormal modes will change as a function of black hole spin, regularity described by a parameter k and scalar field mass respectively, with other parameters taking specific values.

3.1.1 Introduction

Our current best understanding on gravitational interaction is described by general relativity (GR). The recent observation of gravitational waves [1, 53, 54] and black hole shadows[2, 55] provide even more evidences on this fascinating theory. However, GR also faces several challenges, such as, the incompatibility between GR and quantum theory [56], the singularities [3, 4], the late time acceleration of the universe and so on [57, 58, 59]. Among these, the singularities in classical GR are most severe. Because it is widely belief that singularities do not exist in nature, rather they reveal the limitations of GR. Therefore, the idea of regular black holes may provide a solution or a trial to the singularity problem. The regular black holes are the solutions that have horizons and are nonsingular at the origin, and their curvature invariant are regular everywhere[60, 61, 62, 63, 64]. A novel spherical symmetric regular black hole proposed in [10, 11, 12] and reformulated in [13] is a very promising solution to the singularity problem. Later it has also been generalized to the rotating axisymmetric scenario[14, 15, 16]. The exponential convergence factor is used in these regular black holes, which is also used in formulation of the quantum gravity[65].

Scalar field play a crucial role in fundamental physics as well as astrophysics, like the inflation field [66, 67, 68] and also in the dark energy models[69]. Dark matter could also be a kind of scalar field, especially, the ultralight scalar field dark matter could have some advantages over the standard Lambda cold dark matter model[70]. When the Compton wavelength of the scalar field particles are comparable to the characteristic size of the black hole horizon, they can efficiently extract rotational energy from rotating black holes through superradiance instabilities and form macroscopic quasinormal condensates[71, 72]. This provide a unique way and natural laboratory to detect the ultralight scalar field particles through black hole observations, for example, they will leave imprints on the gravitational waves[73, 24]. Because of this and its importance in black hole physics, superradiance has recently attracted plenty of attention from the science community, and physicists have performed investigation in many different aspects and scenarios[74, 75, 76, 77, 78, 79, 80, 81, 82, 83, 84, 85, 86, 87, 88, 89, 90]. It is also worthwhile to mention that there are alternative mechanisms for energy extraction from a rotating black hole, such as Penrose process[91, 92], the Blandford-Znajek process[93], magnetic reconnection process[25, 94, 95] and so on, which may also produce (charged) scalar field particles.

Thus, to study the superradiance and quasinormal of scalar field around rotating regular black holes will provide us with information that could compare with the near future gravitational waves observations. Usually, the scalar filed will be taken as a test field or perturbation filed such that it will not shift the black hole background spacetime. There are some related works on this topic but with different focus or regular spacetime[96, 97, 98]. In this work, we will study the superradiance instabilities and quasinormal modes of scalar field around the newly proposed rotating regular black hole[14, 15, 16]. We will demonstrate how the regular parameter affects the superradiance and quasinormal modes.

The structure of this section is as follows: In subsection.3.1.2, we will introduce the rotating regular black hole spacetime. In subsection.3.1.3, we will solve the massive Klein-Gordon equation in this spacetime, and obtained the radial and angular

equations. Then, in subsection.3.1.4, we will analysis the superradiance instabilities and compute the amplification factor. Then, in subsection.3.1.5, we will compute the quasinormal modes by continued fraction method, we also demonstrate how the quasinormal modes will change as a function of black hole spin, regular parameter and scalar field mass, respectively. In subsection.3.1.6, we will make a conclusion and discussion.

3.1.2 Rotating regular black hole

The metric of nonsingular rotating black hole mentioned in the introduction could be written in the Boyer–Lindquist coordinates as [14, 15, 16],

$$\begin{aligned} \mathrm{d}s^2 = &-\left(1-\frac{2Mr\mathrm{e}^{-k/r}}{\Sigma}\right)\mathrm{d}t^2+\frac{\Sigma}{\Delta}\mathrm{d}r^2+\Sigma\mathrm{d}\theta^2 \\ &-\frac{4aMr\mathrm{e}^{-k/r}}{\Sigma}\sin^2\theta\mathrm{d}t\ \mathrm{d}\phi \\ &+\left[r^2+a^2+\frac{2Mra^2\mathrm{e}^{-k/r}}{\Sigma}\sin^2\theta\right]\sin^2\theta\mathrm{d}\phi^2 \end{aligned} \tag{3.1}$$

with $\Sigma = r^2 + a^2\cos^2\theta, \Delta = r^2 + a^2 - 2Mre^{-k/r}$. and M, a, and k are three parameters, which were assumed to be positive. The Kerr metric could be reduced when set $k/r = 0$.

To show the regularity of this metric, it is convenient to study the spacetime invariant, for example, the Kretschmann invariant $\mathrm{K} = R_{abcd}R^{abcd}$ (R_{abcd} is the Riemann tensor).

$$K = \frac{4M^2\mathrm{e}^{\frac{-2k}{r}}}{r^6\Sigma^6}\left(\Sigma^4k^4 - 8r^3\Sigma^3k^3 + Ak^2 + Bk + C\right) \tag{3.2}$$

where A, B, and C are functions of r and θ, given by

$$\begin{aligned} A &= -24r^4\Sigma\left(-r^4 + a^4\cos^4\theta\right) \\ B &= -24r^5\left(r^6 + a^6\cos^6\theta - 5r^2a^2\cos^2\theta\Sigma\right) \\ C &= 12r^6\left(r^6 - a^6\cos^6\theta\right) \\ &\quad -180r^8a^2\cos^2\theta\left(r^2 - a^2\cos^2\theta\right) \end{aligned} \tag{3.3}$$

For $M \neq 0$, they are regular everywhere.

The solutions of equation

$$\Delta = r^2 + a^2 - 2Mre^{-k/r} = 0 \tag{3.4}$$

will give us the event horizons. The numerical results of horizon structure with different parameters were discussed in [11]. However, there are no analytical solutions.

Despite this, we can use approximation method to solve (3.4) analytically as long as $k/M \ll 1$, and it also satisfies the condition for (3.4) to have two distinct real solutions (see [11]), i.e, less than the critical value k_c^{EH} which decreases with the increase in a, for $a = 0.9M$, $k_c^{EH} \approx 0.1M$, for $a = 0.95M$, $k_c^{EH} \approx 0.05M$. In the Kerr limit, $\Delta_{kerr} = r^2 + a^2 - 2Mr = (r - r_+)(r - r_-)$, where r_+ and r_- are called event and inner horizon of Kerr black hole respectively. They can be seen as the

zeroth order (with respect to k/r) solution to equation (3.4). Because the equation (3.4) can be written as

$$r^2 + a^2 - 2Mr = 2Mr(e^{-k/r} - 1) \tag{3.5}$$

where the right-hand side is much smaller than the left-hand side if $k/r \ll 1$, so the right-hand side is the small perturbation. Therefore, if we brought the zeroth order solutions $r_\pm$ into the right-hand side of (3.5), we will get high order approximation solutions, there are

$$\begin{aligned} \Delta_{kerr} - 2Mr_+(e^{-k/r_+} - 1) &= (r - r_+^I)(r - \tilde{r}_-) \\ \Delta_{kerr} - 2Mr_-(e^{-k/r_-} - 1) &= (r - \tilde{r}_+)(r - r_-^I) \end{aligned} \tag{3.6}$$

where r_+^I and r_-^I could be seen as the first order approximate solutions to (3.4), i.e,

$$\Delta \approx (r - r_+^I)(r - r_-^I) \tag{3.7}$$

where $\tilde{r}_+$ and $\tilde{r}_-$ are the two extra roots because we are solving two quadratic equations, and they are numerically less accurate compared to r_+^I and r_-^I. The explicit forms for r_+^I and r_-^I are given by

$$r_+^I = M + \sqrt{M^2 - a^2 + 2Mr_+(e^{-k/r_+} - 1)} \tag{3.8}$$

$$r_-^I = M - \sqrt{M^2 - a^2 + 2Mr_-(e^{-k/r_-} - 1)} \tag{3.9}$$

For better accuracy, we can carry r_+^I and r_-^I back to the right-hand side of (3.5) and repeat the process above to get more accurate second order solutions of (3.4).

$$r_+^{II} = M + \sqrt{M^2 - a^2 + 2Mr_+^I(e^{-k/r_+^I} - 1)} \tag{3.10}$$

$$r_-^{II} = M - \sqrt{M^2 - a^2 + 2Mr_-^I(e^{-k/r_-^I} - 1)} \tag{3.11}$$

even third order solutions

$$r_+^{III} = M + \sqrt{M^2 - a^2 + 2Mr_+^{II}(e^{-k/r_+^{II}} - 1)} \tag{3.12}$$

$$r_-^{III} = M - \sqrt{M^2 - a^2 + 2Mr_-^{II}(e^{-k/r_-^{II}} - 1)} \tag{3.13}$$

they could be seen as the event horizon and inner horizon of metric (3.1). One could repeat the approximation steps to get more higher order solutions, but third order r_+^{III} and r_-^{III} are sufficient in this work, see Appendix.7.1. Here after we will define $\hat{r}_+ \equiv r_+^{III}$ and $\hat{r}_- \equiv r_-^{III}$ for simplicity.

3.1.3 Decoupled master equations for massive scalar field

The dynamics of a massive scalar field Φ in the spacetime (3.1) is governed by the Klein-Gordon equation

$$\left(\nabla^a \nabla_a - \mu^2\right) \Phi = (\sqrt{-g})^{-1} \partial_\mu \left(\sqrt{-g} g^{\mu\nu} \partial_\nu \Phi\right) - \mu^2 \Phi = 0 \tag{3.14}$$

where $g = det(g_{\mu\nu})$ and μ is the mass of the scalar field. We can rewrite it more explicitly in the Boyer–Lindquist coordinates as

$$\begin{aligned}&\left(\frac{\left(r^2+a^2\right)^2}{\Delta}-a^2\sin^2\theta\right)\partial_t\partial_t\Phi+\frac{4Mare^{-k/r}}{\Delta}\partial_t\partial_\phi\Phi\\&+\left(\frac{a^2}{\Delta}-\frac{1}{\sin^2\theta}\right)\partial_\phi\partial_\phi\Phi-\partial_r\left(\Delta\partial_r\Phi\right)\\&-\frac{1}{\sin\theta}\partial_\theta\left(\sin\theta\partial_\theta\Phi\right)+\mu^2\Sigma\Phi=0\end{aligned}\tag{3.15}$$

For the axisymmetric and asymptotically flat black-hole spacetime, the test Klein-Gordon allows for the separation of variables[99]. Since the spacetime symmetry and asymptotic behavior of Kerr black hole also apply to rotating regular black hole (3.1) as well[11], so we can decompose the field with the ansatz

$$\Phi\left(x^\mu\right)=e^{-i\omega t}e^{im\phi}S_{lm}(\theta)R_{lm}(r)\tag{3.16}$$

where ω is the frequency and it is permitted to be complex. The sign of $Im(\omega)$ determines whether the solution is decaying ($Im(\omega)<0$) or growing ($Im(\omega)>0$) in time. Carrying (3.16) to equation (3.15), this leads to two ordinary differential equations, also called the Teukolsky equations [100]. For the radial part,

$$\begin{aligned}\frac{d}{dr}\left(\Delta\frac{dR_{lm}}{dr}\right)+\Bigg(&\frac{\omega^2\left(r^2+a^2\right)^2-4Mam\omega re^{-k/r}+m^2a^2}{\Delta}\\&-\left(\omega^2a^2+\mu^2r^2+\Lambda_{lm}\right)\Bigg)R_{lm}(r)=0\end{aligned}\tag{3.17}$$

where Λ_{lm} is the separation constant, they are the eigenvalues with respect to the following angular part equation,

$$\frac{1}{\sin\theta}\frac{d}{d\theta}\left(\sin\theta\frac{dS_{lm}}{d\theta}\right)+\left(a^2\left(\omega^2-\mu^2\right)\cos^2\theta-\frac{m^2}{\sin^2\theta}+\Lambda_{lm}\right)S_{lm}(\theta)=0\tag{3.18}$$

The angular solutions $S_{lm}(\theta)$ are spheroidal harmonics $S_{lm}=S_l^m(\cos\theta;c)$. In the nonrotating limit, the spheroidal harmonics reduce to spherical harmonics Y_{lm} and $\Lambda_{lm}\approx l(l+1)$.

We define $u(r)\equiv\sqrt{r^2+a^2}R_{lm}(r)$ and switch to the tortoise coordinate via $dr_*=\frac{r^2+a^2}{\Delta}dr$, after some algebra, the radial function (3.17) takes the following Schrodinger-like form

$$\frac{d^2u\left(r_*\right)}{dr_*^2}+\mathcal{V}(r)u\left(r*\right)=0\tag{3.19}$$

with the effective potential $\mathcal{V}(r)$ given by

$$\begin{aligned}\mathcal{V}(r)=&\left(\omega-\frac{am}{a^2+r^2}\right)^2-\frac{\Delta}{(a^2+r^2)^2}\left(a^2\omega^2+\mu^2r^2+\Lambda_{lm}-2am\omega\right)\\&-\frac{r^2\Delta^2}{(a^2+r^2)^4}-\frac{\Delta+2r^2-2Me^{-k/r}(k+r)}{(a^2+r^2)^2}+\frac{4r^2\Delta}{(a^2+r^2)^3}\end{aligned}\tag{3.20}$$

the first line comes from the potential of equation (3.17) divided by $(r^2+a^2)^2$. The second line represents the effect of introducing the tortoise coordinate dr_*.

3.1.4 Superradiance instability

The incident scalar waves could be amplified when scattered off of a rotating or charged black hole, within certain parameter space of the black hole. This is the so-called Superradiance.

superradiance modes

In this section, we will study the conditions for the happening of superradiance. Now we consider the following asymptotic behavior of the solutions or boundary conditions of equation (3.19),

$$\begin{aligned} u_h(r_*) &= \mathcal{A}_{\mathcal{T}} \exp\left(-ik_h r_*\right), r_* \longrightarrow -\infty (r \to \hat{r}_+) \\ u_\infty(r_*) &= \mathcal{A}_{\mathcal{I}} \exp\left(-ik_\infty r_*\right) + \mathcal{A}_{\mathcal{R}} \exp\left(ik_\infty r_*\right), r_* \longrightarrow \infty (r \to \infty) \end{aligned} \tag{3.21}$$

where $k_h = \sqrt{\mathcal{V}\left(r \to \hat{r}_+\right)} = \omega - m\Omega_h$, $k_\infty = \sqrt{\mathcal{V}(r \to \infty)} = \sqrt{\omega^2 - \mu^2}$. These boundary conditions describe an incoming wave from spatial infinity with an amplitude of $\mathcal{A}_{\mathcal{I}}$, which scatters off the event horizon and produces reflected and transferred waves with amplitudes of $\mathcal{A}_{\mathcal{R}}$ and $\mathcal{A}_{\mathcal{T}}$, respectively.

Now, by equating the Wronskian quantity

$$W = \left(u \frac{du^*}{dr_*} - u^* \frac{du}{dr_*}\right)$$

for regions near the event horizon with its counterparts at infinity, we can get

$$\left|\mathcal{A}_{\mathcal{I}}\right|^2 - \left|\mathcal{A}_{\mathcal{R}}\right|^2 = \frac{\omega - m\Omega_h}{\sqrt{\omega^2 - \mu^2}} \left|\mathcal{A}_{\mathcal{T}}\right|^2 \tag{3.22}$$

where $\Omega_h = a/(\hat{r}_+^2 + a^2)$, According to the above equation, for superradiance to occur, the amplitude of the reflected waves must be greater than the amplitude of the incident waves, and the following frequency criteria must be met

$$\mu < \omega < m\Omega_h \tag{3.23}$$

The frequency or modes satisfying above condition is called superradiance modes.

amplification factor

The degree of amplification caused by the superradiance is described by the amplification factor, it can be computed via

$$Z_{lm} = \frac{\left|\mathcal{A}_{\mathcal{R}}\right|^2}{\left|\mathcal{A}_{\mathcal{I}}\right|^2} - 1 \tag{3.24}$$

Since the Kerr spacetime's symmetry and asymptotic behavior also applies to rotating regular black hole (3.1) as well, the derivation of this section is essentially similar to that of Kerr [71], with the exception that r_+ is replaced by $\hat{r}_+$. However, the geometry of near-horizon region is altered as a result of this difference, which also results in a different amplification factor. Just to be self-content, we will briefly review the calculation steps of amplification factor Z_{lm}.

We assume that the Compton wavelength of scalar field particle is significantly greater than the black hole gravitational size or $\mu M \ll 1$, we also consider the low-frequency regime $\omega M \ll 1$ which also implies $a\omega \ll 1$, these conditions allow us to use the matching-asymptotic techniques [101, 102] as follow.

We divide the space into two overlapping regions, i.e, the near-region $\omega(r-r_+) \ll 1$, and the far-region $r - r_+ \gg M$. We will solve the radial equation (3.17) at these two regions and then match them in their overlapping region, this will give us the analytical solutions to the amplitudes, so that we can compute the amplification factor.

The radial equation (3.17) can be written as

$$x^2(1+x)^2\frac{d^2R_{lm}}{dx^2} + x(x+1)(2x+1)\frac{dR_{lm}}{dx} + (\beta^2x^4 - (\omega^2a^2 + \Lambda_{lm})x(x+1) - \mu^2((\hat{r}_+ - \hat{r}_-)x + \hat{r}_+)^2x(x+1) + Q^2)R_{lm} = 0 \tag{3.25}$$

where we defined new variables

$$x = \frac{r - \hat{r}_+}{\hat{r}_+ - \hat{r}_-} \tag{3.26}$$

$$\beta = \omega(\hat{r}_+ - \hat{r}_-) \tag{3.27}$$

$$Q = \frac{\hat{r}_+^2 + a^2}{\hat{r}_+ - \hat{r}_-}(m\Omega_h - \omega) \tag{3.28}$$

In the near region, we have $kx \ll 1$ and $\mu^2((\hat{r}_+ - \hat{r}_-)x + \hat{r}_+)^2 \approx \mu^2\hat{r}_+^2$, such that equation (3.25) is then approximately take forms as

$$x^2(x+1)^2\frac{d^2R_{lm}}{dx^2} + x(x+1)(2x+1)\frac{dR_{lm}}{dx} + \left(Q^2 - l(l+1)x(x+1)\right)R_{lm} = 0 \tag{3.29}$$

the general solution satisfying the boundary condition (3.21) to the above equation is given by the hypergeometric functions

$$R_{lm} = A_1(\frac{x+1}{x})^{iQ}F(-l, l+1, 1-2iQ, -x) \tag{3.30}$$

the large x behavior of above solution is

$$R_{lm} \sim A_1x^l\frac{\Gamma(1-2iQ)\Gamma(2l+1)}{\Gamma(1+l-2iQ)\Gamma(l+1)} + A_1x^{-l-1}\frac{\Gamma(1-2iQ)\Gamma(-2l-1)}{\Gamma(-l)\Gamma(-l-2iQ)} \tag{3.31}$$

In the far region, equivalently $x \to \infty$, equation (3.25) approximately give us

$$\frac{d^2R_{lm}}{dx^2} + \frac{2}{x}\frac{dR_{lm}}{dx} + \left(\xi^2 - \frac{l(l+1)}{x^2}\right)R_{lm} = 0 \tag{3.32}$$

where $\xi = (\hat{r}_+ - \hat{r}_-)\sqrt{\omega^2 - \mu^2}$. The solution of this equation can be written in terms of the confluent hypergeometric function

$$R_{lm} = \exp(-i\xi x)C_1x^lU(l+1, 2l+2, 2i\xi x) + \exp(-i\xi x)C_2x^{-l-1}U(-l, -2l, 2i\xi x) \tag{3.33}$$

Expanding it for small $kx \ll 1$, we obtain

$$R_{lm} \sim C_1 x^l + C_2 x^{-l-1} \tag{3.34}$$

Now, matching (3.31) and (3.34), we can get

$$C_1 = A_1 \frac{\Gamma(1-2iQ)\Gamma(2l+1)}{\Gamma(l+1)\Gamma(l+1-2iQ)}$$
$$C_2 = A_1 \frac{\Gamma(1-2iQ)\Gamma(-1-2l)}{\Gamma(-l-2iQ)\Gamma(-l)}$$

When $r \to \infty$, from (3.21), we can know the solution of (3.17) takes form as

$$R_{lm} \sim \frac{u_\infty(r_*)}{r} \sim \mathcal{A}_\mathcal{I} \frac{\exp(-ik_\infty r_*)}{r} + \mathcal{A}_\mathcal{R} \frac{\exp(ik_\infty r_*)}{r} \tag{3.35}$$

Expanding (3.33) at infinity and matching to (3.35), we obtain the analytical expression for $\mathcal{A}_\mathcal{I}$ and $\mathcal{A}_\mathcal{R}$

$$\mathcal{A}_\mathcal{I} = C_1 \frac{(-2i)^{-l-1}\xi^{-l}\Gamma(2l+2)}{k_\infty \Gamma(l+1)} + C_2 \frac{(-2i)^l \xi^{l+1}\Gamma(-2l)}{k_\infty \Gamma(-l)}, \tag{3.36}$$

$$\mathcal{A}_\mathcal{R} = C_1 \frac{(2i)^{-l-1}\xi^{-l}\Gamma(2l+2)}{k_\infty \Gamma(l+1)} + C_2 \frac{(2i)^l \xi^{l+1}\Gamma(-2l)}{k_\infty \Gamma(-l)}. \tag{3.37}$$

After some algebra, we finally find the amplification factor (3.24) takes the explicit form as

$$Z_{lm} = 4Q\xi^{2l+1} \frac{(l!)^4}{((2l)!)^2((2l+1)!!)^2} \times \prod_{n=1}^{l} \left(1 + \frac{4Q^2}{n^2}\right) \tag{3.38}$$

The formulas above are valid for any spin $a \leq M$ provided $\mu M < \omega M \ll 1$. In Fig.3.1, we plot Z_{11} for different values of regular parameter k and black hole spin, by setting $\mu M = 0.1$. We can clearly see that the amplification starts when $\omega M > \mu M$, and dies out when it is close to the threshold frequencies $m\Omega_h$. The amplification increases along with the black hole spin, and the parameter k/M only affects the amplification when the frequencies close to the threshold $m\Omega_h$, and bigger k/M will cause a bigger threshold frequency.

3.1.5 Quasinormal modes

Quasinormal modes are solutions of the wave equation (3.19), satisfying the following boundary conditions,

$$u_h(r_*) = \exp(-ik_h r_*), \quad r_* \longrightarrow -\infty (r \to \hat{r}_+)$$
$$u_\infty(r_*) = \exp(ik_\infty r_*), \quad r_* \longrightarrow \infty (r \to \infty) \tag{3.39}$$

which means there are only ingoing waves at the event horizon, while pure outgoing wave at spatial infinity. This condition leads to a discrete eigenvalue of frequencies. Quasinormal modes were referred to as the "fingerprints" of black holes. Because they are determined by the parameters of black holes, like mass and spin etc.

There are many methods to compute the quasinormal modes, see the reviews[103, 104, 105]. In this section, we will use the popular continued fraction method to compute the quasinormal modes, and this method has been used in many outstanding works even recently[106, 107, 108].

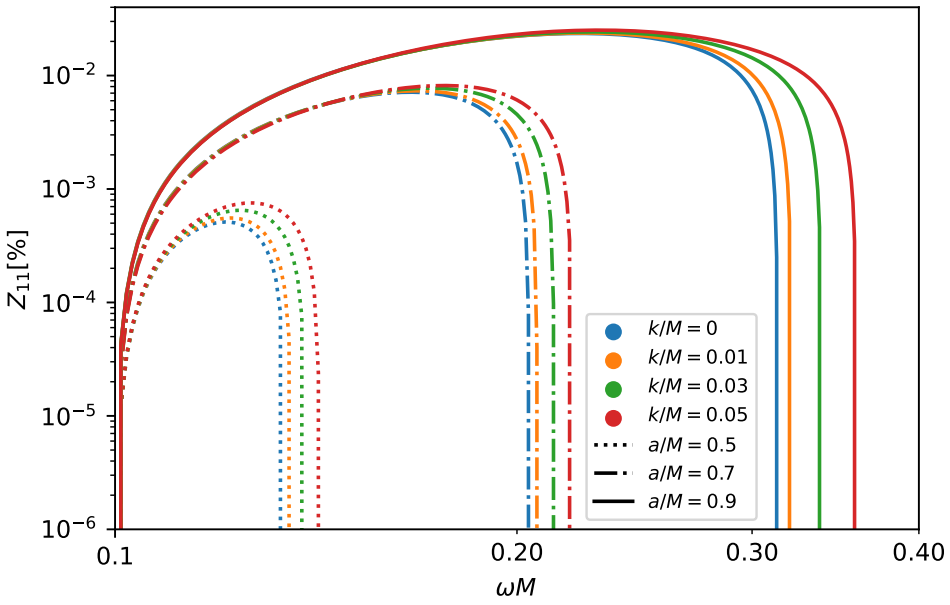

Figure 3.1: The amplification factor Z_{11} for $l = m = 1$, $\mu M = 0.1$, with three black hole spin $a = 0.5M$, $a = 0.7M$ and $a = 0.9M$, and different regular parameter values $k = 0.01M$, $k = 0.03M$, $k = 0.05M$, with the Kerr case ($k = 0$) as reference.

continued fraction method

According to the boundary conditions (3.39), we can obtain a series solution to the radial equation (3.17), by setting $R_{lm}(r)$ as

$$R_{\ell m}(r) = (r - \hat{r}_+)^{-i\sigma_+} (r - \hat{r}_-)^{i\sigma_-} y(r - \hat{r}_-) \tag{3.40}$$

where $-i\sigma_+$ and $i\sigma_-$ are the indices of $R_{\ell m}(r)$ at singular points $r = \hat{r}_+$ and $r = \hat{r}_-$, they are given by

$$\sigma_+ = \frac{\omega \hat{r}_+ - am}{b} \tag{3.41}$$

$$\sigma_- = \frac{\omega \hat{r}_- - am}{b} \tag{3.42}$$

where $b = \hat{r}_+ - \hat{r}_-$. For simplicity, we first define $x = r - \hat{r}_-$, now we have $\Delta = x(x - b)$. Next, we rewrite (3.40) and (3.17) in terms of x, and also substitute the series solution (3.40) into (3.17). Then we calculate the first term (derivatives) of (3.17). When the above operations were done, we collect all the terms with the same order of $y(x)$, $\frac{dy}{dx}$, $\frac{d^2y}{dx^2}$ respectively. At the end, we can get the second order differential equation for $y(x)$,

$$x\,(x-b)\,\frac{d^2y}{dx^2} + (B_1 + B_2 x)\,\frac{dy}{dx} + \Big((\omega^2 - \mu^2)x\,(x-b) - 2\eta\sqrt{\omega^2 - \mu^2}\,(x-b) + B_3\Big)\,y = 0 \tag{3.43}$$

where B_1, B_2, B_3, and η are given by

$$\begin{aligned} B_1 &= (-1-2i\sigma_-)b \\ B_2 &= 2(i\sigma_- - i\sigma_+ + 1) \\ B_3 &= 2\omega^2\hat{r}_+^2 + \omega^2(\hat{r}_+ + \hat{r}_-)^2 + a^2\omega^2 - \Lambda_{lm} - \mu^2\hat{r}_+^2 \\ &\quad + i(\sigma_- - \sigma_+) - (\sigma_- - \sigma_+)^2 \\ \eta &= -(\omega^2 - \mu^2/2)(\hat{r}_+ + \hat{r}_-)/\sqrt{\omega^2 - \mu^2} \end{aligned}$$

The function $y(x)$ can be expanded further in a power series

$$y(x) = e^{ik_\infty x} x^{-(1/2)B_2 - i\eta} \sum_{n=0}^{\infty} d_n \left(\frac{x-b}{x}\right)^n \tag{3.44}$$

By substituting the above series solution $y(x)$ to $R_{\ell m}(r)$, and then to the radial equation (3.17). We can obtain the coefficients d_n which satisfies a three term recurrence relation as follow

$$\alpha_0 d_1 + \beta_0 d_0 = 0 \tag{3.45}$$

$$\alpha_n d_{n+1} + \beta_n d_n + \gamma_n d_{n-1} = 0, \quad n = 1, 2, 3, \ldots\ldots \tag{3.46}$$

where the coefficients are

$$\begin{aligned} \alpha_n &= n^2 + (c_0+1)\, n + c_0 \\ \beta_n &= -2n^2 + (c_1+2)\, n + c_3 \\ \gamma_n &= n^2 + (c_2-3)\, n + c_4 - c_2 + 2 \end{aligned} \tag{3.47}$$

and the intermediate constant c_n are defined as

$$\begin{aligned} c_0 &= B_2 + B_1/b \\ c_1 &= -2\,(c_0 + 1 + i\,(\eta - k_\infty b)) \\ c_2 &= c_0 + 2(1 + i\eta) \\ c_3 &= -c_4 - \tfrac{1}{2}B_2\left(\tfrac{1}{2}B_2 - 1\right) + \eta(i-\eta) + ik_\infty b c_0 + B_3 \\ c_4 &= \left(\tfrac{1}{2}B_2 + i\eta\right)\left(\tfrac{1}{2}B_2 + i\eta + 1 + B_1/b\right) \end{aligned} \tag{3.48}$$

If the series in (3.40) and (3.44) converges and the $r = \infty$ boundary condition (3.39) is satisfied, for a given a, M, k, μ and Λ_{lm}, the frequency ω must be a root of the continued fraction equation

$$0 = \beta_0 - \frac{\alpha_0\gamma_1}{\beta_1 -}\frac{\alpha_1\gamma_2}{\beta_2 -}\frac{\alpha_2\gamma_3}{\beta_3 -}\ldots \tag{3.49}$$

or any of its inversions. (3.49) is obtained by combining equation (3.45) and (3.46). The roots of (3.49) will give us the so-called quasinormal modes.

numerical results

For simplicity and consisting with the literature, we will choose units by setting $M = 1$ in the rest of this paper. Then the radial distance r, the regular parameter k and black hole spin a are measured in unit of M, while the frequency ω and scalar field mass μ are in unit of M^{-1}.

$\mu = 0.1$	$k = 0$		k=0.001		k=0.005		k=0.01	
a	Re(ω)	-Im(ω)	Re(ω)	-Im(ω)	Re(ω)	-Im(ω)	Re(ω)	-Im(ω)
0.1	0.297602	0.094884	0.297658	0.094884	0.297921	0.094914	0.298290	0.094981
0.2	0.298164	0.094661	0.298218	0.094658	0.298452	0.094661	0.298771	0.094684
0.3	0.299116	0.094273	0.299170	0.094269	0.299397	0.094259	0.299698	0.094260
0.4	0.300478	0.093692	0.300534	0.093686	0.300762	0.093668	0.301058	0.093653
0.5	0.302285	0.092873	0.302342	0.092865	0.302574	0.092838	0.302874	0.092809
0.6	0.304579	0.091742	0.304638	0.091732	0.304878	0.091692	0.305185	0.091646
0.7	0.307413	0.090182	0.307475	0.090168	0.307725	0.090110	0.308043	0.090041
0.8	0.310836	0.087989	0.310900	0.087968	0.311160	0.087884	0.311489	0.087780
0.9	0.314815	0.084810	0.314880	0.084778	0.315143	0.084654	0.315474	0.084498

Table 3.1: Values of the quasinormal frequencies for the fundamental mode, with $l = 1$, $m = 0$, $\mu = 0.1$ for different values of k, and spin a.

Our numerical procedures operate as follow, we first calculate the angular eigenvalues Λ_{lm} using the Leaver method[109], by fixing the values for (k, l, m, a, μ). Then the continued fraction equation (3.49) depends only on the quasinormal frequency ω. For practical purposes, it is necessary to truncate the above continuing fraction to an order of n, We use a technique developed by Nollert [110] to approximate the value n. At the end, the root-finding algorithm (Built-in functions in *Wolfram Mathematica*) will be applied to find the roots of the continued fraction equation (3.49). Previous calculations of quasinormal modes in the Kerr background [111, 112] are used to validate our numerical methods. The errors of quasinormal modes caused by using the approximation (3.12) and (3.13) are less than 10^{-2}, see Appendix.7.1, they become extreme accurate when the spin grows.

In Table.3.1 and Table.3.2, we show some of the quasinormal frequencies for the fundamental mode with ($l = 1, m = 0$) and ($l = 1, m = 1$), by setting different black hole spins and regular parameter k. The scalar field mass has been set as $\mu = 0.1$. In Table.3.3, we show the dependency of quasinormal frequencies on the scalar field mass μ and regular parameter k, by setting $(l = 1, m = 1), a = 0.5$. Please note that we used minus $Im(\omega)$ to represent the imaginary part of quasinormal modes here and after in this paper. In all three tables, the $k = 0$ columns correspond to the quasinormal modes of Kerr black hole, which are in excellent six decimals agreements with the results obtained before by [111, 112].

From Table.3.1 and Table.3.2, we notice that the real part of quasinormal frequencies grow along with the black spin, while the imaginary part decrease with spin. The regular parameter k does play a role on the quasinormal frequencies. We also computed ($l = 1$, $m = 1$) quasinormal frequencies with smaller spin intervals $\Delta a = 0.02$ from $a = 0.05$ to $a = 0.91$, with regular parameter $k = 0, 0.001, 0.005, 0.01$, The results were plotted in Fig.3.2. We can see that the higher spin and bigger regular parameter k, the more deviation from Kerr black hole ($k = 0$).

To better show the dependency of quasinormal frequencies on the regular parameter k, we plot the real and imaginary part of quasinormal frequencies as a function of regular parameter k in Fig.3.3, with three different high spins ($a \geq 0.5$). We can see that regular parameter k will increase the real part of quasinormal frequencies

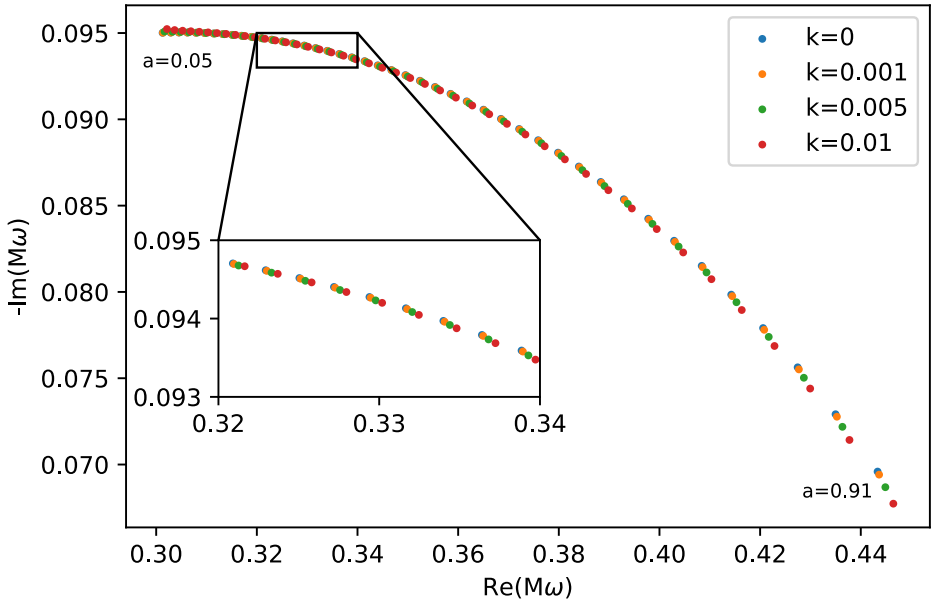

Figure 3.2: the $l = m = 1$ fundamental quasinormal frequencies as a function of black hole spin (from $a = 0.05$ to $a = 0.91$ with spin intervals $\Delta a = 0.02$), with the regular parameter $k = 0, 0.001, 0.005, 0.01$, scalar filed mass $\mu = 0.1$.

$\mu = 0.1$	$k = 0$		k=0.001		k=0.005		k=0.01	
a	Re(ω)	-Im(ω)	Re(ω)	-Im(ω)	Re(ω)	-Im(ω)	Re(ω)	-Im(ω)
0.1	0.305329	0.095029	0.305390	0.095027	0.305674	0.095054	0.30607	0.095118
0.2	0.314119	0.094920	0.314184	0.094915	0.314460	0.094908	0.314833	0.094921
0.3	0.323981	0.094569	0.324052	0.094561	0.324347	0.094536	0.324735	0.094518
0.4	0.335181	0.093883	0.335261	0.093871	0.335590	0.093828	0.336015	0.093783
0.5	0.348105	0.092714	0.348198	0.092696	0.348576	0.092630	0.349059	0.092552
0.6	0.363345	0.090805	0.363456	0.090780	0.363904	0.090678	0.364474	0.090554
0.7	0.381888	0.087678	0.382025	0.087637	0.382580	0.087474	0.383285	0.087271
0.8	0.405606	0.082262	0.405790	0.082191	0.406531	0.081904	0.407473	0.081540
0.9	0.439045	0.071342	0.439332	0.071183	0.440495	0.070533	0.441982	0.069685

Table 3.2: Values of the quasinormal frequencies for the fundamental mode, with $l = m = 1$, $\mu = 0.1$ for different values of k, and spin a.

a=0.5	$k=0$		k=0.001		k=0.005		k=0.01	
μ	Re(ω)	-Im(ω)	Re(ω)	-Im(ω)	Re(ω)	-Im(ω)	Re(ω)	-Im(ω)
0	0.344753	0.094395	0.344848	0.094375	0.345234	0.094301	0.345726	0.094214
0.1	0.348105	0.092714	0.348198	0.092696	0.348576	0.092630	0.349059	0.092552
0.2	0.358230	0.087478	0.358317	0.087466	0.358671	0.087423	0.359125	0.087375
0.3	0.375284	0.078022	0.375362	0.078020	0.375679	0.078016	0.376086	0.078016
0.4	0.399201	0.062970	0.399267	0.062982	0.399536	0.063031	0.399884	0.063099
0.5	0.429036	0.040234	0.429096	0.040270	0.429336	0.040421	0.429639	0.040617

Table 3.3: Values of the quasinormal frequencies for the fundamental mode, with $l = m = 1$, $a = 0.5$ for different values of k, and mass μ.

gently. For the imaginary part, the regular parameter k decrease imaginary part of quasinormal frequencies, even more for higher spins. These features could provide us some insights on the connection between the regularity of black hole and the stability of massive scalar field perturbation. All the imaginary part of quasinormal modes are negative (see Table.3.1, 3.2, 3.3 and Fig.3.2, 3.3), which means the black hole (3.1) is stable under massive scalar field perturbation. What is more, especially in the high spin regime, the increasing in regular parameter k will cause a smaller imaginary part of quasinormal modes compare to Kerr black hole, which corresponds to a longer damping time. The regularity of black hole seems put more 'elasticity' onto the massive scalar field perturbation such that they will live longer than the Kerr black hole scenario. On the other hand, increasing in regular parameter k will cause a bigger real part of quasinormal modes, which means it will increase the oscillation frequency of scalar field perturbation. In addition, we again see black hole spins change quasinormal frequencies significantly for both real and imaginary part.

Last but not least, we investigate the quasinormal frequencies dependency on the scalar field mass μ. From Table.3.3, we can see that, for the real part, the value increase monotonously with the scalar field mass μ. For the imaginary part, the value decrease monotonously with the scalar field mass μ. It seems that, for $\mu \leq 0.3$, the bigger regular parameter k, the bigger real part and smaller imaginary part. But for $\mu \geq 0.4$, it is not the case, where the bigger k, the bigger imaginary part. So, the scalar field mass will affect the relation between the regularity of black hole and the stability of massive scalar field perturbation. It maybe easy to understand because the different scalar field mass will significantly change the behavior of scalar field perturbation such that it will react differently to the regularity of black hole spacetime.

3.1.6 Conclusion and discussion

We have studied the massive scalar field perturbation around regular rotating black hole. We first introduced the newly proposed regular black hole spacetime metric (3.1) and some physical quantities, also we used approximation method to analytically solve the horizons. Then we separated and solved the massive Klein-Gordon equation in this spacetime and obtained the master equations(3.15), also radial part (3.17) and angular part equations (3.18). With these equations, we studied

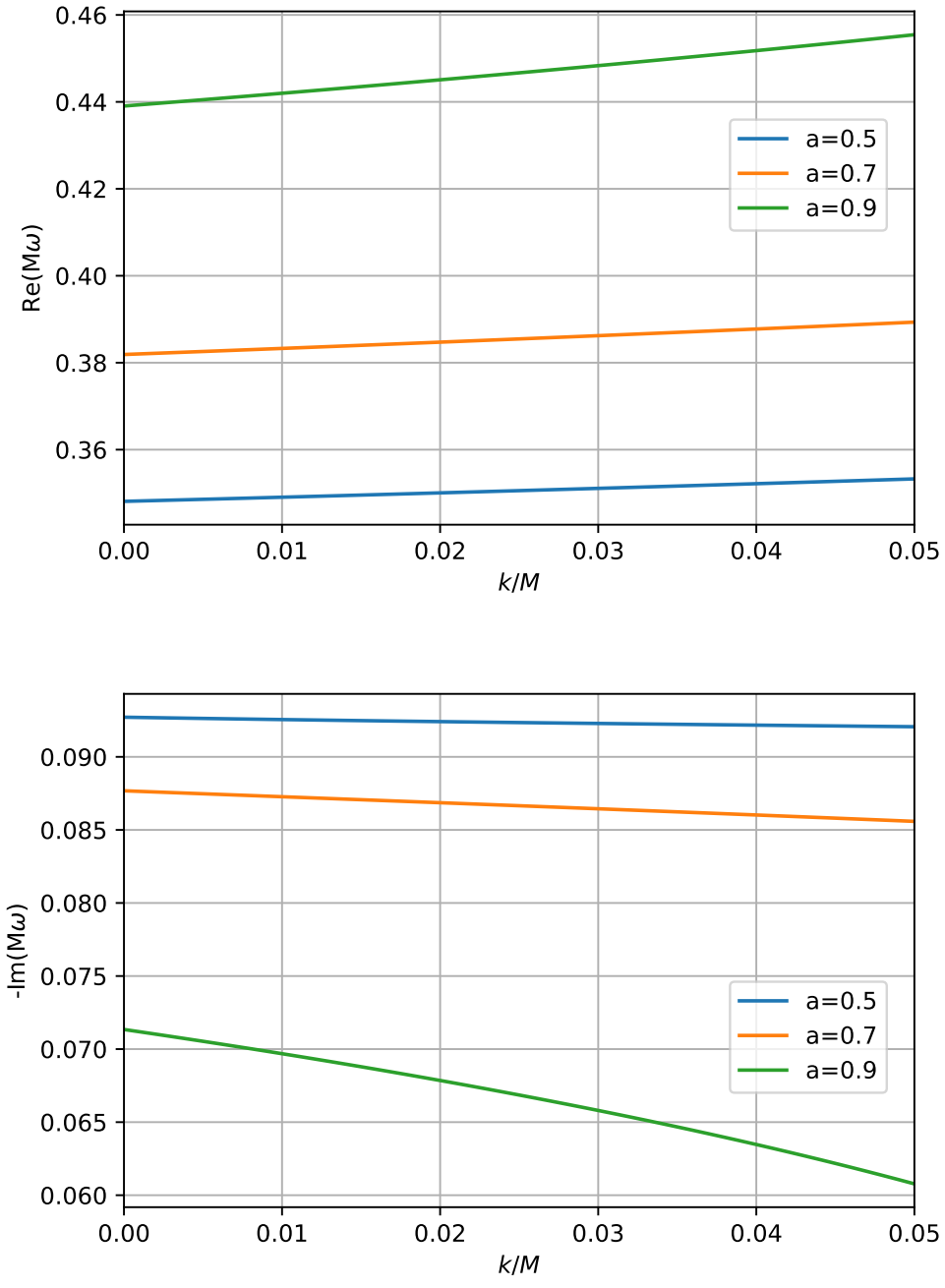

Figure 3.3: upper and lower plots are respectively the real and imaginary part of the fundamental quasinormal frequencies as a function of parameter k, by setting $l = m = 1$, $\mu = 0.1$ and three different spins $a = 0.5, 0.7, 0.9$.

the superradiance instability and quasinormal modes.

For the superradiance instability, we first discussed the conditions for the superradiance happen. The results show that the amplification happens when the frequencies are within certain parameter region (3.23). Then, we used the matching-asymptotic method to compute the amplification factor under small mass and low frequency approximations. At the end, we obtained a very net analytical expression for the amplification factor (3.38) and we plotted the $l = m = 1$ modes with several parameters.

Regarding to the quasinormal modes, we applied the continued fraction method to numerically calculated the quasinormal modes of the rotating regular black hole. We present three tables (Table.3.1, 3.2, 3.3), and the $k = 0$ columns could validate our numerical approaches. It is in excellent agreement with the previous results in the Kerr limit[111, 112]. The numerical results, in these tables also in Fig.3.3, are computed by selecting some parameters as the variables while others are settled down with certain values for the purpose of studying: (a) fundamental quasinormal modes as a function of black hole spin a; (b) fundamental quasinormal modes as a function of regular parameter k; (c) fundamental quasinormal modes as a function of scalar field mass μ.

This work is the first step to study the perturbations around the nonsingular rotating black hole (3.1). There are many researches could be conduct at the future. For example, the superradiance instability and quasinormal modes of the vector and gravitational perturbations (i.e, gravitational waves) in this spacetime. We believe it will give us more deeper understanding on black holes and gravity. We leave this research to the future.

3.2 Gravitational perturbation around rotating hairy black hole

Abstract: The No Hair theorem in classical general relativity predicts that rotating black holes are specified by the Kerr metric, which is uniquely identified by the mass and spin. However, as a pioneering study beyond general relativity, the rotating hairy black hole has been proposed, which encompasses the Kerr black hole as a special case. In these black holes, there are extra hair which could appear due to the additional surrounding sources such as dark matter or dark energy. In this work, we study the phenomenology of the rotating hairy black hole in terms of gravitational perturbations. In particular, the superradiance and the quasinormal modes. Using the matching-asymptotic method, we derive the amplification factor and the superradiance conditions. We also calculate the quasinormal modes using the continued fraction method. The results are in very good agreement with previous studies in the Kerr limit. We also show how the amplification and quasinormal modes will shift in response to variations in the hairy parameters, black hole spin, and quantum numbers.

3.2.1 Introduction

Recent observations of gravitational waves (GW) [1, 53, 54] and black hole shadows [2, 55] provide strong evidence for the existence of black holes, the intriguing objects

predicted by general relativity. It is widely believed that the physically rotating black holes in the universe are Kerr black holes described by the Kerr metric. The famous No Hair theorem [5, 6, 7, 8, 9] also states that the Kerr metric is completely determined by the mass and spin of the black hole. However, due to the additional surrounding sources like dark matter, Kerr black holes can acquire an additional global charge, called 'hair', which deviates from the Kerr metric [113]. Recently, the hairy black hole and later its rotating version were obtained using the gravitational decoupling approach (GD) [17, 18], which is specifically designed to describe deformations of known solutions of general relativity induced by additional sources[114, 115]. The rotating hairy black hole attracts amount of theoretical and observational investigations [116, 117, 118, 119, 120, 121].

To verify this proposal in GW observations, the ringdown signal from black holes will be essential. This is because the ringdown waveforms arise from the gravitational perturbation of black holes, such as the final phase of black hole merger [1, 53, 54, 122], and they are the superposition of quasinormal modes which are directly related to the No Hair theorem. The discovery and accurate identification of the quasinormal modes could be the 'smoking gun' for testing this proposal as well as general relativity [123].

On the other hand, if the wavelength of gravitational perturbations is comparable to the size of the black hole horizon, they can efficiently extract rotational energy from rotating black holes through superradiance instabilities, which also generate GW and black hole shadow signals that could be detected by observations in the future [71, 124, 125]. Because of its importance, superradiance has recently received a lot of attention from the scientific community, and physicists have explored a variety of aspects and scenarios.[74, 75, 76, 77, 78, 79, 80, 126, 127, 81, 82, 83, 84, 85, 86, 87, 88, 89, 90, 128, 129, 130].

Studying the superradiance and quasinormal of the gravitational perturbation field around rotating hairy black holes is therefore important for preparing to compare with future GW and black hole shadow observations. There is some work on this topic, but it is limited to scalar perturbations in the case of non-rotating hairy black holes [118]. In this work, we will study the superradiance and quasinormal modes of the gravitational perturbation around the rotating hairy black hole [18]. We will show how the hairy parameters and the spin of the black hole affect the superradiance and the quasinormal modes.

This section is organized as follows: In subsection.3.2.2, we will introduce the rotating hairy black hole and derive the horizons using the approximation method. In subsection.3.2.3, we obtain the master equations for the gravitational perturbation in this spacetime, and also drive the radial and angular equations respectively. Then, in subsection.3.2.4, we will calculate the superradiance amplification factor and obtain the conditions for the superradiance. We will also explore the quasinormal modes in this spacetime in subsection.3.2.5, after introducing the continued fraction method, we will present the numerical results on how the quasinormal modes will change as a function of the black hole spin, hairy parameters. In subsection.3.2.6, we will come to a conclusion and discussion.

3.2.2 Rotating hairy black hole

In [18], a rotating hairy black hole was derived using the GD approach which is precisely designed to find the deformation of the known solution of general relativity [114, 115]. In Boyer-Lindquist coordinates it is

$$\begin{aligned} ds^2 = &-\left[\frac{\Delta - a^2\sin^2\theta}{\Sigma}\right]dt^2 + \frac{\Sigma}{\Delta}dr^2 + \Sigma d\theta^2 \\ &- 2a\sin^2\theta\left[1 - \frac{\Delta - a^2\sin^2\theta}{\Sigma}\right]dtd\phi \\ &+ \sin^2\theta\left[\Sigma + a^2\sin^2\theta\left(2 - \frac{\Delta - a^2\sin^2\theta}{\Sigma}\right)\right]d\phi^2 \end{aligned} \tag{3.50}$$

with $\Delta = r^2 + a^2 - 2Mr + \alpha r^2 e^{-r/\left(M-\frac{h_0}{2}\right)}$, and $\Sigma = r^2 + a^2\cos^2\theta$. M, a denote the mass and spin of the black hole. α measures the deviation from standard Kerr black holes and is related to the primary hair h_0 via $h_0 = \alpha h$, where h_0 measures the increase of entropy caused by the hair and must satisfy the condition $h_0 \leq 2M \equiv h_K$ to ensure asymptotic flatness. The hair could originate from new fields or new gravitational sectors such as dark matter or dark energy as long as their effective energy-momentum tensor satisfies the strong energy condition outside the event horizon[18]. All these parameters were assumed to be positive. When $\alpha = 0$, this spacetime reduces to the Kerr metric, which means the absence of surrounding matter.

The solutions of the equation

$$\Delta = r^2 + a^2 - 2Mr + \alpha r^2 e^{-r/\left(M-\frac{h_0}{2}\right)} = 0 \tag{3.51}$$

will give us the horizons. One can find the numerical results of the horizon structure with different parameter values in [117]. However, the exact analytical solutions are impossible for this Δ function.

Nevertheless, we can use the approximate method to solve (3.51) analytically as long as $\alpha e^{-r/\left(M-\frac{h_0}{2}\right)} \ll 1$, which means that the new field where the hair originate from is less dense, such that the deviation from the standard Kerr black hole is small, and it will also satisfy the condition for (3.51) to have two distinct real solutions, see [117].

For the Kerr black hole, $\Delta_{kerr} = r^2 + a^2 - 2Mr = (r - r_+)(r - r_-)$, where r_+ and r_- are the so-called event and inner horizon, respectively. They can be considered as the zero-order solution (in terms of $\alpha e^{-r/\left(M-\frac{h_0}{2}\right)}$) of equation (3.51). Because Eq. (3.51) can be written as

$$r^2 + a^2 - 2Mr = -\alpha r^2 e^{-r/\left(M-\frac{h_0}{2}\right)} \tag{3.52}$$

where the right side is much smaller than the left side if $\alpha e^{-r/\left(M-\frac{h_0}{2}\right)} \ll 1$, so the right side is the small perturbation. Thus, if we bring the zero-order solutions $r_\pm$ into the right-hand side of (3.52), we obtain high-order approximate solutions, they are

$$\begin{aligned} \Delta_{kerr} + \alpha r_+^2 e^{-r_+/\left(M-\frac{h_0}{2}\right)} &= (r - r_+^I)(r - \tilde{r}_-) \\ \Delta_{kerr} + \alpha r_-^2 e^{-r_-/\left(M-\frac{h_0}{2}\right)} &= (r - \tilde{r}_+)(r - r_-^I) \end{aligned} \tag{3.53}$$

where r_+^I and r_-^I can be regarded as the first-order approximate solutions of (3.51), while $\tilde{r}_+$ and $\tilde{r}_-$ are the two additional roots, since we are solving two quadratic equations, and they are numerically less accurate compared to r_+^I and r_-^I. The explicit forms for r_+^I and r_-^I are given by

$$r_+^I = M + \sqrt{M^2 - a^2 - \alpha r_+^2 e^{-r_+/\left(M-\frac{h_0}{2}\right)}} \tag{3.54}$$

$$r_-^I = M - \sqrt{M^2 - a^2 - \alpha r_-^2 e^{-r_-/\left(M-\frac{h_0}{2}\right)}} \tag{3.55}$$

For better accuracy, we could substitute r_+^I and r_-^I back to the right hand side of (3.52) and repeat the above process to get more accurate second order solutions of (3.51),

$$r_+^{II} = M + \sqrt{M^2 - a^2 - \alpha {r_+^I}^2 e^{-r_+^I/\left(M-\frac{h_0}{2}\right)}} \tag{3.56}$$

$$r_-^{II} = M - \sqrt{M^2 - a^2 - \alpha {r_-^I}^2 e^{-r_-^I/\left(M-\frac{h_0}{2}\right)}} \tag{3.57}$$

they could be considered as the event horizon and inner horizon of metric (3.50). One could repeat the approximation steps to obtain higher order solutions, but second order r_+^{II} and r_-^{II} are sufficient in this work, see Appendix.7.2. This approximation method has been used previously to study rotating regular black holes in [131]. In the following, for simplicity, we will define $\hat{r}_+ \equiv r_+^{II}$ and $\hat{r}_- \equiv r_-^{II}$. Then the Δ function could be approximately written as

$$\Delta \approx (r - \hat{r}_+)(r - \hat{r}_-) \tag{3.58}$$

In the following sections, whenever we write Δ for metric (3.50), we refer to the above function (3.58).

3.2.3 Decoupled perturbation equations

The spacetime symmetries and the asymptotic behavior of this rotating hairy black hole (3.50) are the same to Kerr black hole[11], so we can decompose the perturbation field Φ with the ansatz

$$\Phi\left(x^\mu\right) = e^{-i\omega t} e^{im\phi} S_{slm}(\theta) R_{slm}(r) \tag{3.59}$$

where ω is the complex-valued frequency, l, m are the quantum numbers.

In a breakthrough work [100], it was shown that the linear gravitational perturbations of Kerr geometry can be described by a master equation: the Teukolsky equation. However, the Teukolsky equation does not apply to the metric (3.50) because it is not a solution of Einstein's field equation. Fortunately, using the approximation for the Δ function in subsection.3.2.2, we can see from Eq.(3.53) that it effectively corresponds to the Δ function of a Kerr-Newman black hole, with the effective charge $Q_{effect} \approx \sqrt{\alpha \hat{r}_+^2 e^{-\hat{r}_+/\left(M-\frac{h_0}{2}\right)}}$ or $\sqrt{\alpha \hat{r}_-^2 e^{-\hat{r}_-/\left(M-\frac{h_0}{2}\right)}}$ (we used the results of the second order approximation). For a Kerr-Newman black hole, it has been shown that the gravitational perturbation can be described by the Dudley-Finley equation [132], which provides a good approximation to the dynamics of the perturbation field when the electric charge $Q \leq M/2$ [133, 134]. The condition is

also satisfied in our situation, since we assume $Q_{effect} \ll M$ by the definition of the approximation method in subsection.3.2.2.

The final Δ function (3.58) we considered could be seen as a Kerr-Newman black hole with effective mass $M_{effect} = (\hat{r}_+ + \hat{r}_-)/2$ and charge $Q_{effect} = \sqrt{\hat{r}_+\hat{r}_- - a^2}$. It could be proved that $Q_{effect} \ll M_{effect}$. Therefore, we can approximately obtain a pair of differential equations from the Dudley-Finley equation [133, 134], and in fact these two equations have the same form as the Teukolsky equations, with the only difference that we replace Δ_{kerr} by Δ function (3.58) compared to the Kerr case. The radial equation has the following form

$$\Delta^{-s}\frac{d}{dr}\left(\Delta^{s+1}\frac{dR_{slm}}{dr}\right) + \left(\frac{K^2 - isK\Delta'}{\Delta} + 4is\omega r - \lambda\right)R_{slm}(r) = 0 \tag{3.60}$$

where s is the spin weight of the gravitational field, $K = (r^2 + a^2)\omega - am$ and $\lambda = \Lambda_{lm} + a^2\omega^2 - 2am\omega$, Λ_{lm} is the separation constant, they are the eigenvalues with respect to the following angular equation,

$$\begin{aligned}\frac{1}{\sin\theta}\frac{d}{d\theta}\left(\sin\theta\frac{dS_{slm}}{d\theta}\right) + \Bigg(a^2\omega^2\cos^2\theta - \frac{m^2}{\sin^2\theta} - 2sa\omega\cos\theta \\ -\frac{2sm\cos\theta}{\sin^2\theta} - s^2\cot^2\theta + s + \Lambda_{lm}\Bigg)S_{slm}(\theta) = 0\end{aligned} \tag{3.61}$$

The solutions of the angular equation are $S_{lm}(\theta)$, which are called spheroidal harmonics [136]. In the nonrotating or spherically symmetric limit case, the spheroidal harmonics reduce to the well-known spherical harmonics Y_{lm} and also $\Lambda_{lm} \approx l(l+1) - s(s+1)$.

We define $u(r) \equiv \sqrt{r^2 + a^2}R_{slm}(r)$ and switch to the tortoise coordinate via $dr_* = \frac{r^2+a^2}{\Delta}dr$, after some algebra, the radial function (3.60) takes the following Schrödinger-like form

$$\frac{d^2u\,(r_*)}{dr_*^2} + \mathcal{V}(r)u\,(r*) = 0 \tag{3.62}$$

with the effective potential $\mathcal{V}(r)$ given by

$$\begin{aligned}\mathcal{V}(r) = \left(\omega - \frac{am}{a^2 + r^2}\right)^2 - \frac{is\omega\Delta'}{a^2 + r^2} + \frac{isam\Delta'}{(a^2 + r^2)^2} \\ + \frac{\Delta}{(a^2 + r^2)^2}(4is\omega r - \lambda) - \frac{dG}{dr_*} - G^2\end{aligned} \tag{3.63}$$

where $G = r\Delta/(r^2+a^2)^2 + s\Delta'/2(r^2+a^2)$. The last two terms represent the effect of introducing the tortoise coordinate dr_*. The other terms result from the potential of Eq.(3.60) divided by $(r^2 + a^2)^2$.

3.2.4 Superradiance and amplification factor

Within a certain black hole parameter space, the incident gravitational waves can be amplified if they are scattered by a rotating black hole. In this way, the gravitational waves can efficiently extract the rotational energy of the black hole, i.e., the gravitational waves of the black hole are superradiant. We focus on the regime

in which the back-reaction of the superradiant waves on the geometry is negligible, i.e., the background spacetime metric is held fixed. This can be easily satisfied since we are working in the linear perturbation framework, and furthermore the superradiant waves are typically distributed over a very large area, which implies very low density and consequently small back-reaction effects. The work [135] which investigate the back-reaction of bosonic clouds on the Kerr geometry could be a good reference.

In this section we will examine the conditions for the occurrence of superradiance. We consider the following boundary conditions of Eq.(3.62),

$$\begin{aligned} u_h(r_*) &= \mathcal{T}_s \Delta^{-s/2} \exp\left(-ik_h r_*\right), r_* \longrightarrow -\infty (r \to \hat{r}_+) \\ u_\infty(r_*) &= \mathcal{I}_s r^s \exp\left(-i\omega r_*\right) + \mathcal{R}_s r^{-s} \exp\left(i\omega r_*\right), r_* \longrightarrow \infty (r \to \infty) \end{aligned} \tag{3.64}$$

where $k_h = \omega - m\Omega_h$, $\Omega_h = a/(\hat{r}_+^2 + a^2)$. The above boundary conditions state that there is an incoming wave from spatial infinity with amplitude $\mathcal{I}_s$ that is scattered at the event horizon such that it produces reflected waves with amplitude $\mathcal{R}_s$ and transferred waves with amplitude $\mathcal{T}_s$ respectively. The subscription s means that all amplitudes are s dependent.

To quantify how much the incident waves were amplified due to superradiance, one usually refers to the amplification factor Z_{slm}, which is given by [71, 137]

$$Z_{slm} = \left| \frac{\mathcal{R}_s \mathcal{R}_{-s}}{\mathcal{I}_s \mathcal{I}_{-s}} \right| - 1 \tag{3.65}$$

where $\mathcal{R}_{-s}$ and $\mathcal{I}_{-s}$ means the substitution of s by $-s$ in the solution of Eq.(3.62) with the asymptotic behavior of $u_\infty(r_*)$ given by

$$u_\infty(r_*) = \mathcal{I}_{-s} r^{-s} \exp\left(-i\omega r_*\right) + \mathcal{R}_{-s} r^{s} \exp\left(i\omega r_*\right), r_* \longrightarrow \infty (r \to \infty) \tag{3.66}$$

The derivation of Z_{slm} in this rotating hairy black hole (3.50) spacetime is about the same as in Kerr[71], with the difference that r_+ is replaced by $\hat{r}_+$. However, this changes the geometry of the region near the horizon, which also affects the amplification factor. Just to be self-content, we shall briefly discuss the calculation process of amplification factor Z_{slm}.

We will consider the low frequency range $\omega M \ll 1$ which also implies $a\omega \ll 1$. These approximations allow us to use the matching-asymptotic techniques [101, 102, 138] as follows.

We divide the space into two overlapping regions, which we call the near region $\omega(r - r_+) \ll 1$ and the far region $r - r_+ \gg M$. Then We can solve the radial Eq. (3.60) in these two regions and match the solutions in the overlapping region. In this way, we obtain the analytical solutions for the amplitudes, which we can use to calculate the amplification factor. The specific steps are as follows.

Let's rewrite (3.60) as

$$\begin{aligned} x^2(1+x)^2 \frac{d^2 R_{slm}}{dx^2} + x(x+1)(2x+1)\frac{dR_{slm}}{dx} \\ + (k^2x^4 + 2iskx^3 - \lambda x(x+1) - isQ(2x+1) + Q^2)R_{slm} = 0 \end{aligned} \tag{3.67}$$

where we have defined new variables

$$x = \frac{r - \hat{r}_+}{\hat{r}_+ - \hat{r}_-} \tag{3.68}$$

$$k = \omega(\hat{r}_+ - \hat{r}_-) \tag{3.69}$$

$$Q = \frac{\hat{r}_+^2 + a^2}{\hat{r}_+ - \hat{r}_-}(m\Omega_h - \omega) \tag{3.70}$$

In the near region, the quantity $kx \ll 1$, so Eq.(3.67) could be approximately written as

$$x^2(x+1)^2\frac{d^2R_{slm}}{dx^2} + x(x+1)(2x+1)\frac{dR_{slm}}{dx} + \left(Q^2 - isQ(2x+1) - l(l+1)x(x+1)\right)R_{slm} = 0 \tag{3.71}$$

the general solutions to the above equation as well as satisfying the boundary conditions (3.64) are given by the hypergeometric functions

$$R_{slm} = A_1(\frac{x+1}{x})^{-s+iQ}F(\xi, \beta, \gamma, -x) \tag{3.72}$$

where

$$\gamma = 1 - s - 2iQ \tag{3.73}$$

$$\beta = l - s + 1 \tag{3.74}$$

$$\xi = -l - s \tag{3.75}$$

the large x behavior of above solution is

$$R_{slm} \sim A_1 x^{l-s}\frac{\Gamma(\gamma)\Gamma(\beta-\xi)}{\Gamma(\gamma-\xi)\Gamma(\beta)} + A_1 x^{-l-1-s}\frac{\Gamma(\gamma)\Gamma(\xi-\beta)}{\Gamma(\xi)\Gamma(\gamma-\beta)} \tag{3.76}$$

In the far region, equivalently $x \to \infty$, Eq.(3.67) approximately give us

$$\frac{d^2R_{slm}}{dx^2} + \frac{2}{x}\frac{dR_{slm}}{dx} + \left(k^2 + \frac{2isk}{x} - \frac{l(l+1)}{x^2}\right)R_{slm} = 0 \tag{3.77}$$

The solution of this equation can be written in terms of the confluent hypergeometric function

$$R_{slm} = \exp(-ikx)C_1 x^{l-s}U(l-s+1, 2l+2, 2ikx) + \exp(-ikx)C_2 x^{-l-1-s}U(-l-s, -2l, 2ikx) \tag{3.78}$$

Applying the condition $kx \ll 1$ and Expanding it with respect to kx, we obtain

$$R_{slm} \sim C_1 x^{l-s} + C_2 x^{-l-1-s} \tag{3.79}$$

Now, we can match the solutions (3.76) and (3.79), and it will give us

$$C_1 = A_1\frac{\Gamma(1-s-2iQ)\Gamma(2l+1)}{\Gamma(l+1-s)\Gamma(l+1-2iQ)}$$

$$C_2 = A_1\frac{\Gamma(1-s-2iQ)\Gamma(-1-2l)}{\Gamma(-l-2iQ)\Gamma(-l-s)}$$

From (3.64), we can know that, when $r \to \infty$, the solution of (3.60) will take form as

$$R_{slm} \sim \frac{u_\infty(r_*)}{r} \sim \mathcal{I}_s \frac{\exp(-i\omega r_*)}{r} + \mathcal{R}_s \frac{\exp(i\omega r_*)}{r^{2s+1}} \tag{3.80}$$

Expanding (3.78) at infinity and matching to (3.80), we obtain the analytical expression for $\mathcal{I}_s$ and $\mathcal{R}_s$

$$\begin{aligned}
\mathcal{I}_s &= C_1 \frac{(-2i)^{s-l-1} k^{s-l} \Gamma(2l+2)}{\omega \Gamma(l+s+1)} + C_2 \frac{(-2i)^{l+s} k^{l+1+s} \Gamma(-2l)}{\omega \Gamma(-l+s)} \\
\mathcal{R}_s &= C_1 \frac{(2i)^{-l-1-s} k^{s-l} \Gamma(2l+2)}{\omega^{2s+1} \Gamma(l+1-s)} + C_2 \frac{(2i)^{l-s} k^{l+1+s} \Gamma(-2l)}{\omega^{2s+1} \Gamma(-l-s)}.
\end{aligned} \tag{3.81}$$

After some calculations and algebra, we finally find that the amplification factor (3.65) takes the following explicit form

$$Z_{slm} = 4Qk^{2l+1} \frac{((l-s)!(l+s)!)^2}{((2l)!)^2((2l+1)!!)^2} \times \prod_{n=1}^{l} \left(1 + \frac{4Q^2}{n^2}\right) \tag{3.82}$$

The above formula is applicable to any spin $a \leq M$ as long as $\omega M \ll 1$. In Fig.3.4, Z_{-222} is shown for different values of the parameter α, h_0 and the spin of the black hole. We can clearly see that the amplification starts at $\omega M > 0$, and stops abruptly when it comes close to the threshold frequencies $m\Omega_h$. Increasing the spin of the black hole leads to an increase in the amplification, and the parameters α and h_0 only affect the amplification when the frequencies reach the threshold $m\Omega_h$. Larger α and smaller h_0 cause a larger threshold frequency.

The formula (3.82) also gives us the conditions of superradiance. If we want the amplitude of the reflected waves to be larger than that of the incident waves, i.e. $Z_{slm} > 0$ which means $Q > 0$, the following frequency criteria must be fulfilled

$$0 < \omega < m\Omega_h \tag{3.83}$$

where $0 < \omega$ is required by the boundary conditions. The modes that satisfy the above condition are also called superradiance modes.

One could also study the amplification of scalar and vector perturbation fields using the same formula (3.82) by simply substituting $s = 0$ and $s = \pm 1$. However, we will focus only on amplification of gravitational perturbations because it is more interesting and could potentially provide phenomenological intuitions for gravitational wave observations. In the next section, we will also study the quasinormal modes of gravitational perturbations, which are closely related to the ringdown signal of gravitational waves.

3.2.5 Quasinormal modes

Quasinormal modes are the solutions of the equation (3.62) satisfying the following boundary conditions,

$$\begin{aligned}
u_h(r_*) &\propto \Delta^{-s/2} \exp(-ik_h r_*), \quad r_* \longrightarrow -\infty (r \to \hat{r}_+) \\
u_\infty(r_*) &\propto r^{-s} \exp(i\omega r_*), \quad r_* \longrightarrow \infty (r \to \infty)
\end{aligned} \tag{3.84}$$

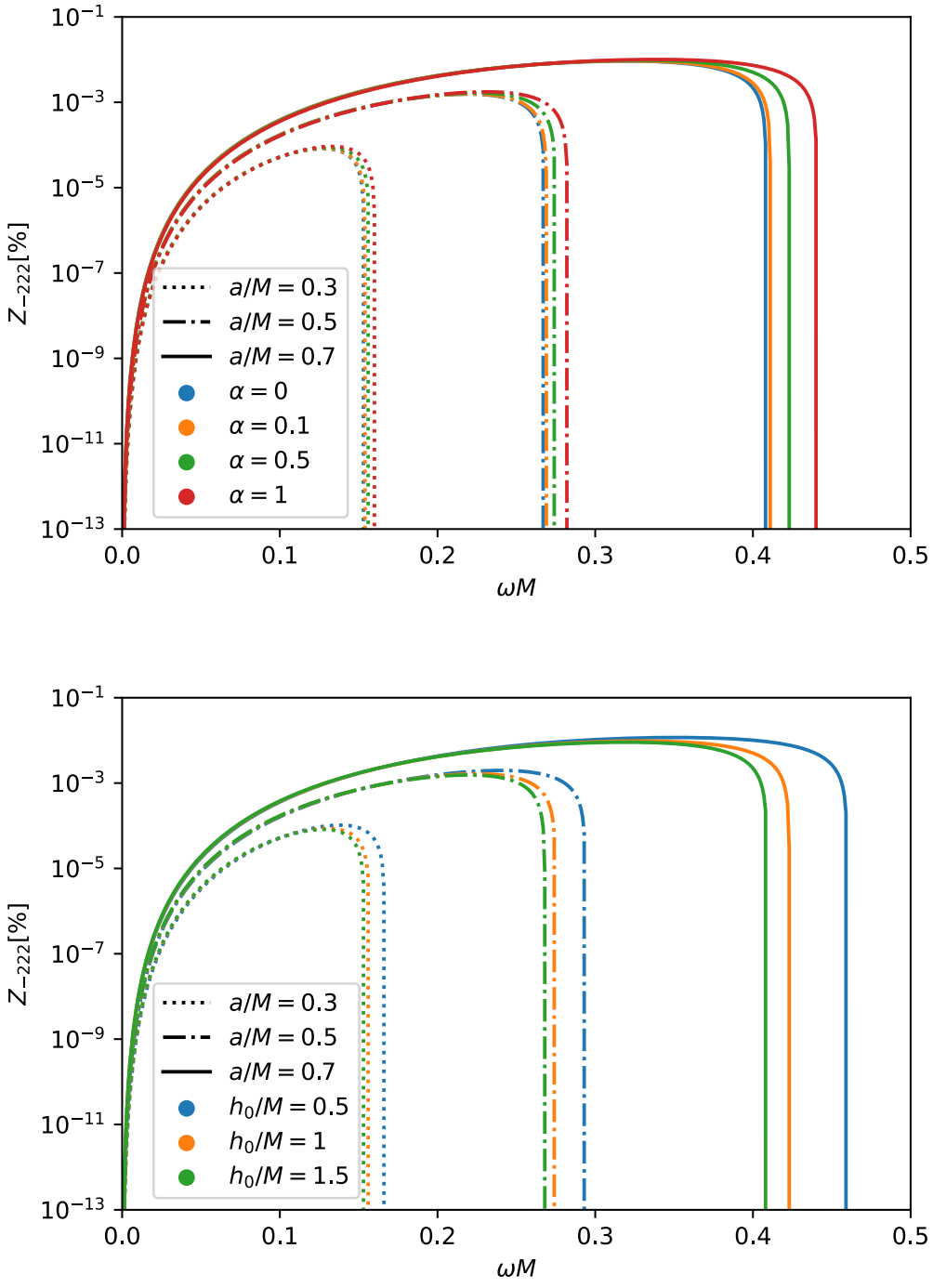

Figure 3.4: The amplification factor Z_{-222} for $s = -2, l = m = 2$, with three black hole spin $a = 0.3M$, $a = 0.5M$ and $a = 0.7M$. The upper plot aims to show the effects of α to the amplification by setting $h_0 = M$ with $\alpha \neq 0$ (please note that $\alpha = 0$ also means $h_0 = 0$). The lower plot is to show the effects of h_0 to the amplification by setting $\alpha = 0.5$.

These boundary conditions mean that there are only incoming waves at the event horizon, while there are pure outgoing waves at spatial infinity. These conditions lead to discrete eigenvalue frequencies. Quasinormal modes are also called "fingerprints" of black holes. This is because they are completely determined by the hair parameters of the black hole, such as mass and spin.

There are a number of different approaches to calculating quasinormal modes, see reviews in [103, 104, 105]. In this work we will use the popular continued fraction method, which has been used in many outstanding papers, including recent ones[106, 107, 108, 131].

continued fraction method

According to the boundary conditions (3.84) and the poles of the radial Eq. (3.60) we can formulate a series solution for $R_{slm}(r)$ as

$$R_{slm}(r) = (r-\hat{r}_+)^{-i\sigma_+}(r-\hat{r}_-)^{i\sigma_-}\, y(r-\hat{r}_-) \tag{3.85}$$

where $-i\sigma_+$ and $i\sigma_-$ are the indices of $R_{slm}(r)$ corresponding to the singular points $r=\hat{r}_+$ and $r=\hat{r}_-$ respectively, they have the form

$$-i\sigma_+ = -s - i\frac{\omega\hat{r}_+ - am}{b} \tag{3.86}$$

$$i\sigma_- = -s + i\frac{\omega\hat{r}_+ - am}{b} \tag{3.87}$$

where $b=\hat{r}_+-\hat{r}_-$. For simplicity, we define $x=r-\hat{r}_-$ and thus $\Delta = x(x-b)$. Then we can rewrite (3.85) and (3.60) into the expression of x and substitute the series solution (3.85) into (3.60). Next, we compute the derivatives in (3.60). Combining the terms based on $y(x)$, $\frac{dy}{dx}$, and $\frac{d^2y}{dx^2}$, respectively, we obtain the equation for $y(x)$,

$$x\,(x-b)\,\frac{d^2y}{dx^2} + (B_1 + B_2 x)\,\frac{dy}{dx} + \left(\omega^2 x\,(x-b) - 2\eta\omega\,(x-b) + B_3\right) y = 0 \tag{3.88}$$

where B_1, B_2, B_3 and η are given by

$$\begin{aligned}
B_1 &= (-s-1-2i\sigma_-)b \\
B_2 &= 2(i\sigma_- - i\sigma_+ + s + 1) \\
B_3 &= 2\omega^2\hat{r}_+^2 + \omega^2(\hat{r}_+ + \hat{r}_-)^2 + a^2\omega^2 - \Lambda_{lm} \\
&\quad + i(2s+1)(\sigma_- - \sigma_+) - (\sigma_- - \sigma_+)^2 - is\omega(b + 2 - 4\hat{r}_+) \\
\eta &= -\omega(\hat{r}_+ + \hat{r}_-) - is
\end{aligned}$$

The function $y(x)$ can be extended to a power series in the following form

$$y(x) = e^{i\omega x}x^{-(1/2)B_2 - i\eta}\sum_{n=0}^{\infty} d_n \left(\frac{x-b}{x}\right)^n \tag{3.89}$$

Substituting this new power series solution of $y(x)$ into Eq.(3.88). We obtain the coefficients d_n satisfying a three term recurrence relation as follows

$$\alpha_0 d_1 + \beta_0 d_0 = 0 \tag{3.90}$$

$$\alpha_n d_{n+1} + \beta_n d_n + \gamma_n d_{n-1} = 0, \quad n = 1, 2, 3, \ldots\ldots \tag{3.91}$$

where the coefficients are

$$\begin{aligned}\alpha_n &= n^2 + (c_0+1)\,n + c_0 \\ \beta_n &= -2n^2 + (c_1+2)\,n + c_3 \\ \gamma_n &= n^2 + (c_2-3)\,n + c_4 - c_2 + 2\end{aligned} \tag{3.92}$$

and the intermediate constant c_n are defined as

$$\begin{aligned}c_0 &= B_2 + B_1/b \\ c_1 &= -2\,(c_0 + 1 + i\,(\eta - \omega b)) \\ c_2 &= c_0 + 2(1+i\eta) \\ c_3 &= -c_4 - \tfrac{1}{2}B_2\left(\tfrac{1}{2}B_2 - 1\right) + \eta(i-\eta) + i\omega b c_0 + B_3 \\ c_4 &= \left(\tfrac{1}{2}B_2 + i\eta\right)\left(\tfrac{1}{2}B_2 + i\eta + 1 + B_1/b\right)\end{aligned} \tag{3.93}$$

By combining Eq.(3.90) and (3.91), we can get

$$0 = \beta_0 - \frac{\alpha_0\gamma_1}{\beta_1 -}\frac{\alpha_1\gamma_2}{\beta_2 -}\frac{\alpha_2\gamma_3}{\beta_3 -}\ldots \tag{3.94}$$

If the power series (3.85) and (3.89) converge and satisfy the boundary condition $r = \infty$ (3.84), then for a given a, M, α, h_0, and Λ_{lm} the frequency ω must be a root of the continued fraction Eq.(3.94) or any of its inversions. The solutions of Eq.(3.94) give us the quasinormal modes.

numerical results

For simplicity and in agreement with the literature, we set $M = 1$ as the unit in the rest of this paper. Then the radial distance r, the hair parameter h_0 and the spin of the black hole a are measured in the unit M, while the frequency ω is given in the unit M^{-1}.

Our numerical procedures are as follows: first, we compute the angular eigenvalues using the Leaver method[109], by fixing the values for (α, h_0, l, m, a). Then the continued fraction Eq.(3.94) is only a function of the quasinormal modes ω. It is more convenient and necessary to truncate the continuing fraction to a certain order N, so we use the technique developed by Nollert [110] to fix the value of N. Finally, the root-finding algorithm (built-in functions in *Wolfram Mathematica*) is used to find the roots of Eq. (3.94). Previous calculations of quasinormal modes in the Kerr background and also the scalar field perturbation scenario [139, 111, 112] are used to validate and verify our numerical methods. The errors of the quasinormal modes caused by using the approximation (3.56) and (3.57) are smaller than 10^{-2}, see Appendix.7.2, they become extremely accurate in the slow rotation region.

In Table.3.4 we show some of the quasinormal modes for the fundamental mode ($s = -2, l = m = 2$) with different black hole spins a, parameter α by setting $h_0 = 1$. The columns with $\alpha = 0$ correspond to the quasinormal modes of the Kerr black hole, which are in excellent six decimals agreements with the results previously obtained by [139]. In Table.3.5 we show some of the ($s = -2, l = m = 2$) quasinormal frequencies for the fundamental mode with different black hole spins and parameter h_0 by setting $\alpha = 0.5$. In Table.3.6 we show few overtones of ($s = -2, l = m = 2$) quasinormal frequencies with different black hole spins a, by setting $h_0 = 1$ and $\alpha = 0.5$.

$h_0 = 1$	$\alpha = 0$, Kerr		α=0.1		α=0.5		α=1	
a	Re(ω)	-Im(ω)	Re(ω)	-Im(ω)	Re(ω)	-Im(ω)	Re(ω)	-Im(ω)
0.1	0.387018	0.088706	0.387514	0.089016	0.389570	0.090307	0.392310	0.092044
0.2	0.402145	0.088311	0.402704	0.088634	0.405023	0.089980	0.408122	0.091795
0.3	0.419527	0.087729	0.420173	0.088067	0.422858	0.089476	0.426465	0.091385
0.4	0.439842	0.086882	0.440609	0.087229	0.443813	0.088683	0.448146	0.090663
0.5	0.464123	0.085639	0.465067	0.085980	0.469026	0.087410	0.474434	0.089363
0.6	0.494045	0.083765	0.495261	0.084067	0.500398	0.085320	0.507520	0.087007
0.7	0.532600	0.080793	0.534283	0.080988	0.541479	0.081742	0.551710	0.082628
0.8	0.586017	0.075630	0.588656	0.075563	0.600233	0.075057	0.617659	0.073752
0.9	0.671614	0.064869	0.677072	0.064026	0.703157	0.059362	0.753330	0.048227

Table 3.4: Values of the quasinormal modes for the fundamental mode, with $s = -2$, $l = m = 2$, $h_0 = 1$ with different values of α and spin a. $\alpha = 0$ corresponds to Kerr black hole

$\alpha = 0.5$	$h_0 = 0.5$		h_0=1		h_0=1.5		h_0=1.99	
a	Re(ω)	-Im(ω)	Re(ω)	-Im(ω)	Re(ω)	-Im(ω)	Re(ω)	-Im(ω)
0.1	0.397183	0.095178	0.389570	0.090307	0.387063	0.088734	0.387017	0.088706
0.2	0.413525	0.095024	0.405023	0.089980	0.402195	0.088333	0.402145	0.088311
0.3	0.432555	0.094764	0.422858	0.089476	0.419576	0.087720	0.419527	0.087729
0.4	0.455153	0.094289	0.443813	0.088683	0.439877	0.086787	0.439842	0.086882
0.5	0.482712	0.093406	0.469026	0.087410	0.464125	0.085370	0.464123	0.085639
0.6	0.517632	0.091731	0.500398	0.085320	0.493995	0.083205	0.494045	0.083765
0.7	0.564612	0.088411	0.541479	0.081742	0.532508	0.079807	0.532600	0.080793
0.8	0.635179	0.081067	0.600233	0.075057	0.586002	0.074068	0.586017	0.075630
0.9	0.778872	0.057647	0.703157	0.059362	0.672405	0.062476	0.671614	0.064869

Table 3.5: Values of the quasinormal modes for the fundamental mode, with $s = -2$, $l = m = 2$, $\alpha = 0.5$ with different values of h_0 and spin a.

From Table.3.4, Table.3.5, and Table.3.6, we notice that the real part of the quasinormal frequencies increases with the spin of the black hole, while the imaginary part decreases with the spin, regardless of the parameters and overtones are. This can be caused by the choice of a certain quantum number $l = m = 2$.

To better show the dependence of the quasinormal frequencies on the quantum number (l, m) and the spin of the black hole, we have also computed ($s = -2$, $l = 2, 3$, $m = -l....l$) quasinormal frequencies from $a = 0.01$ to $a = 0.91$, with parameters $\alpha = 0.5$, $h_0 = 1$, The results are shown in Fig.3.5. Please note that here and in all further figures we have used the minus $Im(\omega)$ for the imaginary part of the quasinormal modes. We see that the quantum number l causes only a general shift of the quasinormal modes. However, non-negative m causes the real part of the quasinormal modes to increase with spin (larger m, larger ratio of increase), while negative m causes the opposite. For the imaginary part, all decrease with spin.

Next, we want to investigate how the hairy parameters α and h_0 affect the relation between the quasinormal modes and the spin of the black hole. Therefore,

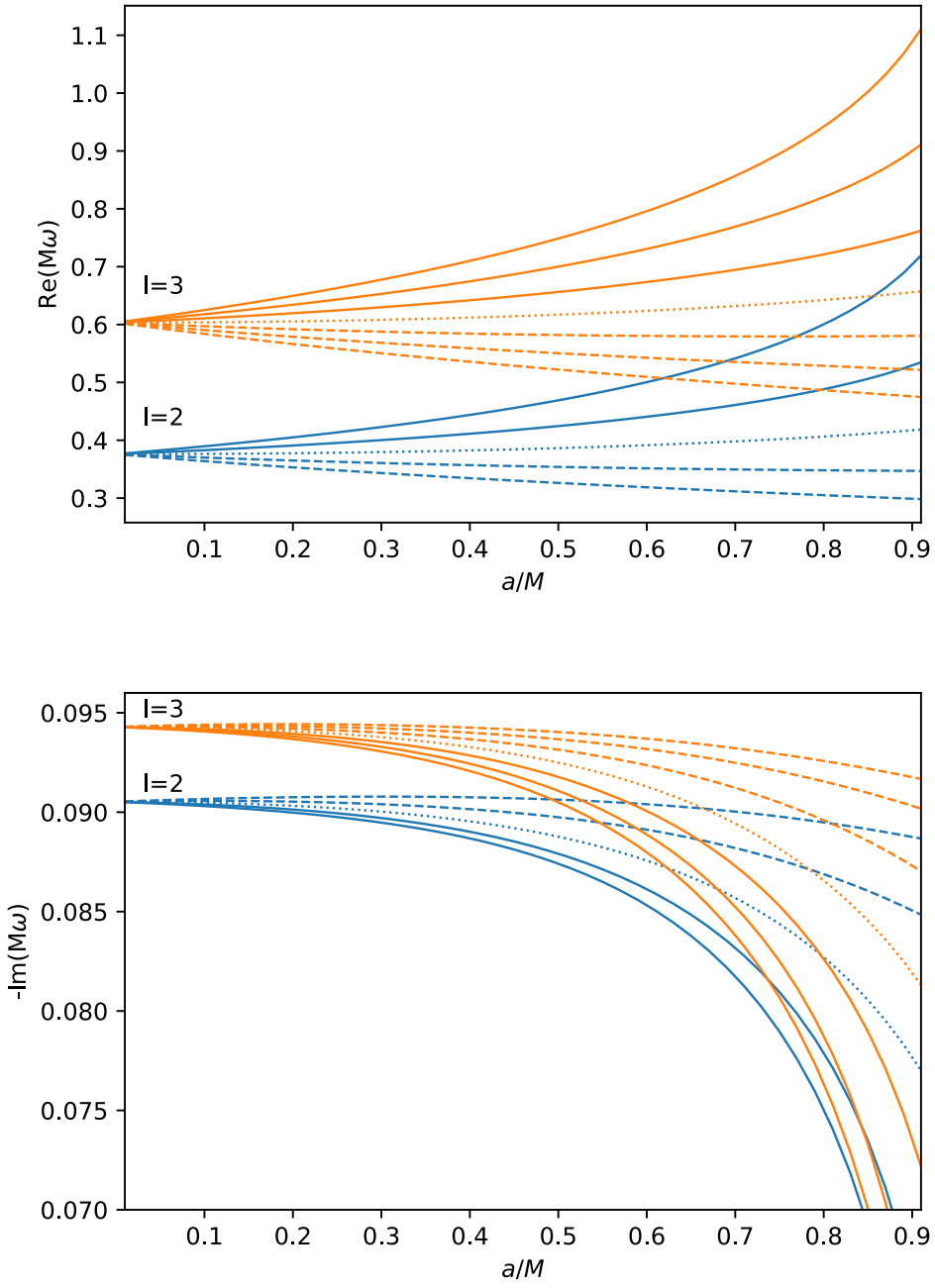

Figure 3.5: The $s = -2$ fundamental quasinormal modes with l =2, 3, $\alpha = 0.5$, $h_0 = 1$ and different values of m. The upper panel is the real part. From top to bottom, solid lines correspond to $m = l, ..., 1$, dotted line $m = 0$, and dashed lines correspond to $m = -1, ..., -l$. The low panel is the minus imaginary part, From top to bottom, solid lines correspond to $m = 1, ..., l$, dotted line $m = 0$, and dashed lines correspond to $m = -l, ..., -1$.

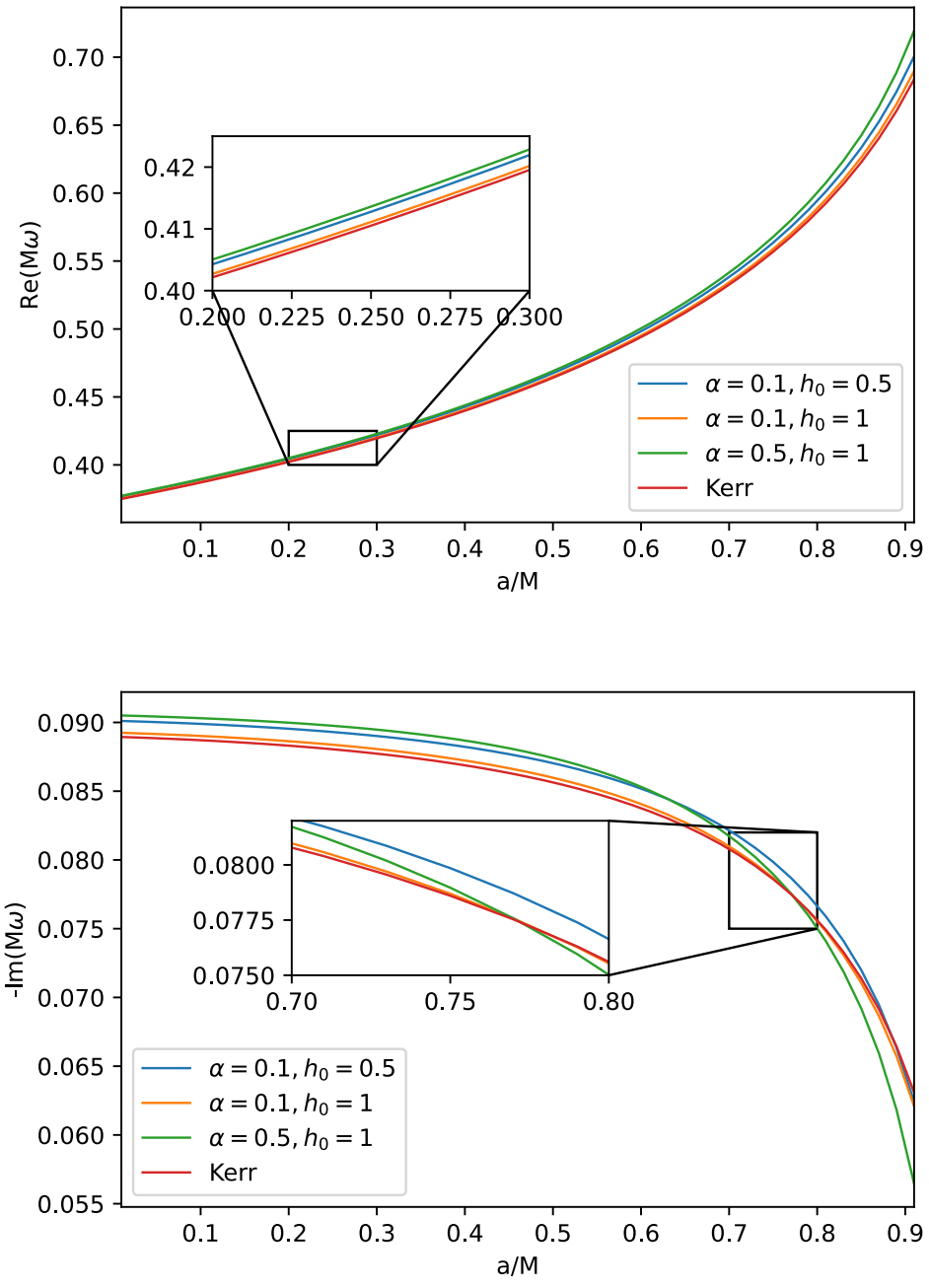

Figure 3.6: The $s = -2$ fundamental quasinormal modes with $l = m = 2$ as a function of spin a, with different combinations of α, h_0. The upper panel is the real part while the low panel is the minus imaginary part

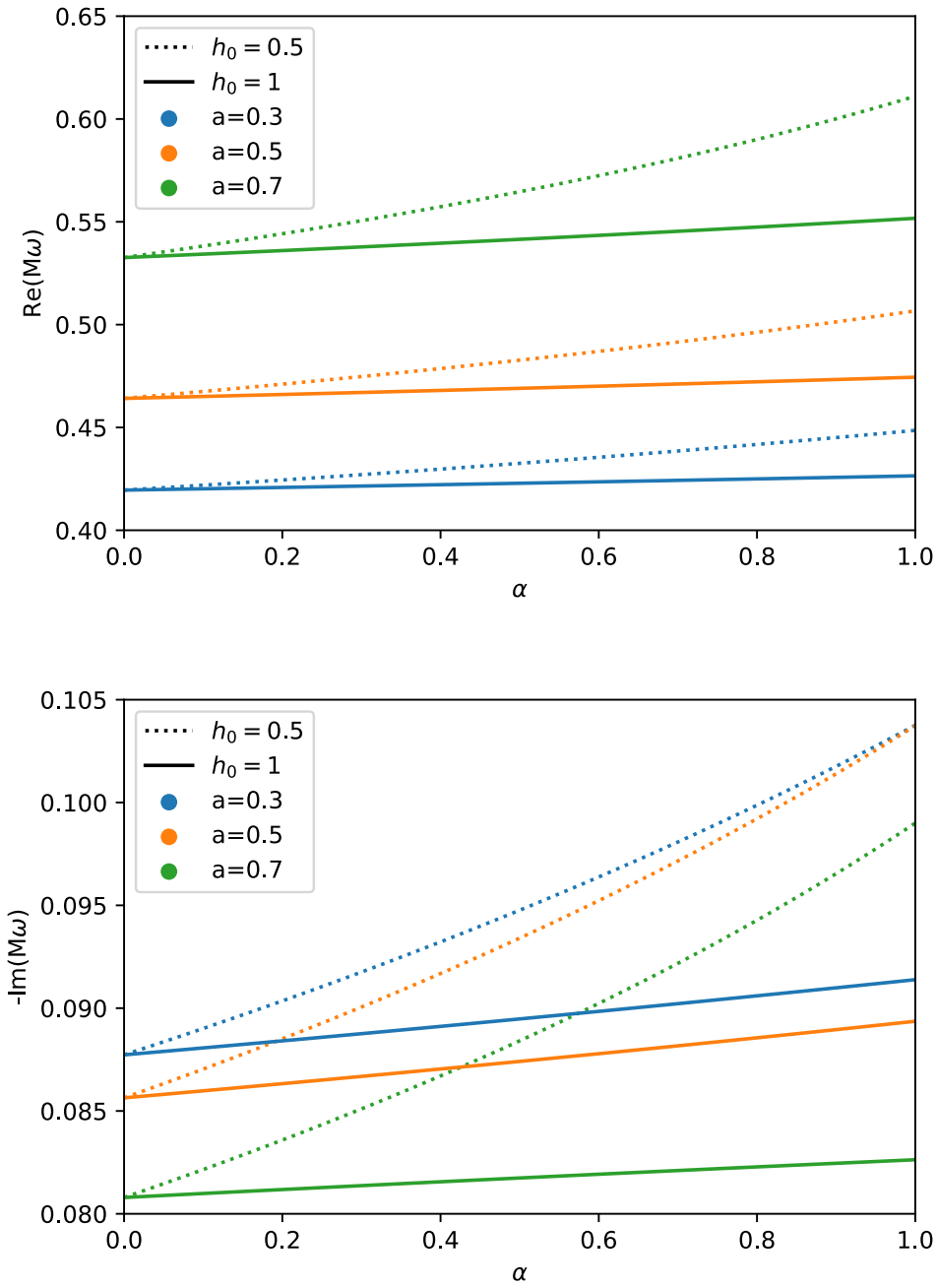

Figure 3.7: The real and imaginary part of $s = -2, l = m = 2$ fundamental quasinormal modes as a function of parameter $\alpha \in [0, 1]$, with different spin a and h_0 (please note when $a \leq 0.7$, the errors are also below 10^{-2} even with $\alpha = 1, h_0 = 0.5$, see Fig.7.2)

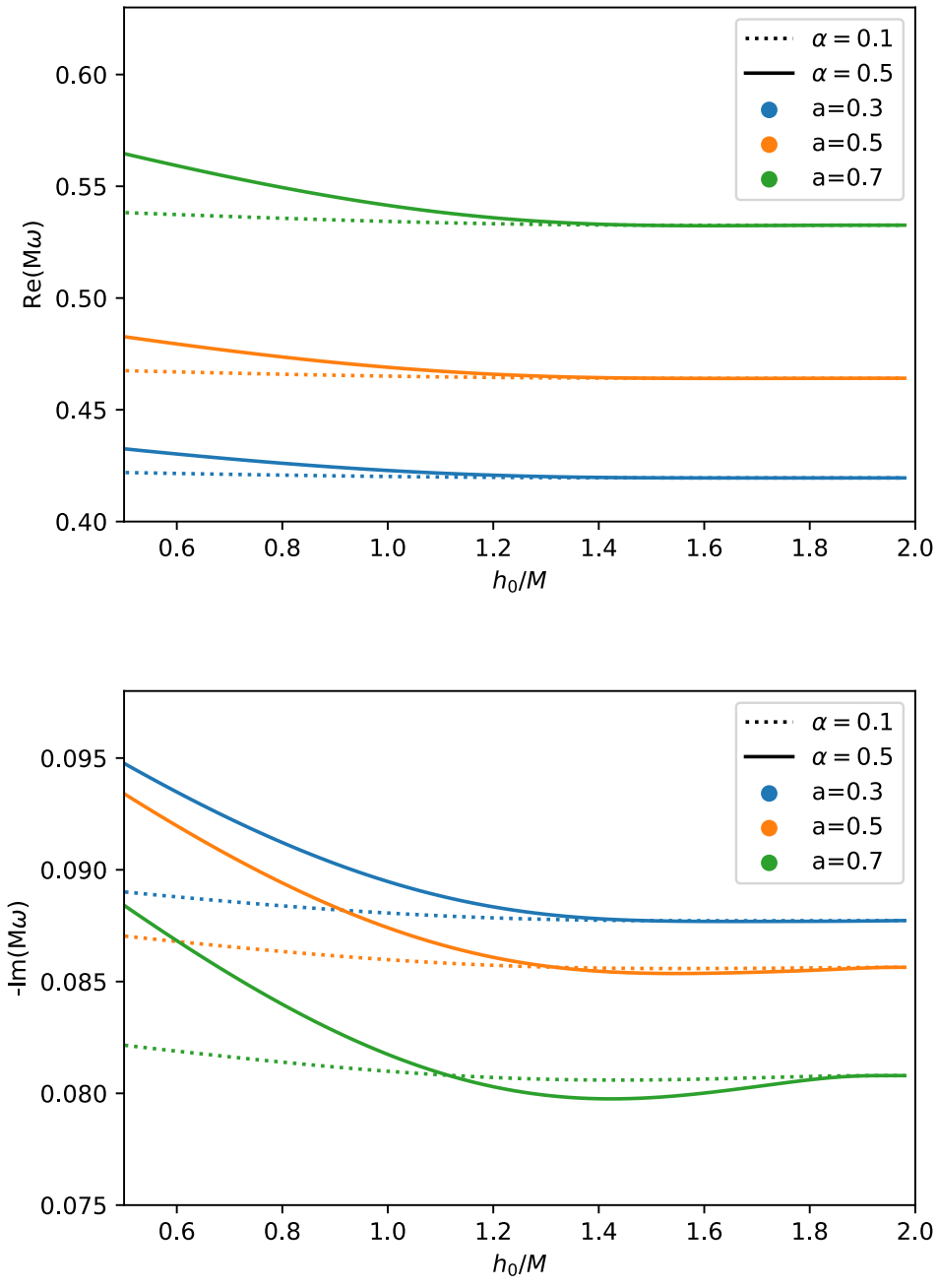

Figure 3.8: The $s = -2$ fundamental quasinormal modes with $l = m = 2$ as a function of parameter $h_0 \in [0.5, 2]$, with different spin a and α. The upper panel is the real part while the low panel is the minus imaginary part.

α=0.5, $h_0=1$	$n=0$ (α=0)		n=0		n=1		n=2	
a	Re(ω)	-Im(ω)	Re(ω)	-Im(ω)	Re(ω)	-Im(ω)	Re(ω)	-Im(ω)
0.1	0.387018	0.088706	0.389570	0.090307	0.363668	0.275243	0.319704	0.477473
0.2	0.402145	0.088311	0.405023	0.089980	0.381088	0.273410	0.340243	0.471936
0.3	0.419527	0.087729	0.422858	0.089476	0.400989	0.270985	0.363435	0.465366
0.4	0.439842	0.086882	0.443813	0.088683	0.424145	0.267668	0.390088	0.457279
0.5	0.464123	0.085639	0.469026	0.087410	0.451751	0.262947	0.421462	0.446879
0.6	0.494045	0.083765	0.500398	0.085320	0.485800	0.255900	0.459693	0.432749
0.7	0.532600	0.080793	0.541479	0.081742	0.530002	0.244640	0.508836	0.411948
0.8	0.586017	0.075630	0.600233	0.075057	0.592584	0.224438	0.577928	0.376740
0.9	0.671614	0.064869	0.703157	0.059362	0.700220	0.177572	0.694559	0.296919

Table 3.6: Values of the quasinormal modes for the fundamental mode $n = 0$ and few overtones n =1, 2, with $s = -2$, $l = m = 2$, $\alpha = 0.5$, $h_0 = 1$ for different values of spin a. The $n = 0$ (α=0) column correspond to the Kerr black hole case. As one expect, the higher overtone, the smaller real part and bigger imaginary part of quasinormal modes.

in Fig.3.6 we plot the real and imaginary parts of the quasinormal frequencies as a function of the black hole spin, with different combinations of the parameters α and h_0. We can see that α and h_0 do not affect the overall tendency between quasinormal modes and the spin of the black hole, but slightly change the slopes. In particular, for the imaginary part, there are crossings between different combinations of the α and h_0 parameters in the high spin regime.

To see it more clearly, we examine respectively how α and h_0 will affect the quasinormal frequencies. We have plotted the ($s = -2$, $l = m = 2$) fundamental quasinormal modes as a function of the parameter α in Fig.3.7 and h_0 in Fig.3.8, by fixing three spin and the other one parameter. We find that both the real and imaginary parts of the quasinormal modes increase monotonically with α. However, the reverse is true for h_0: the larger h_0 becomes, the smaller the quasinormal modes become, and they almost become a constant when they reach the limit $h_0 = h_K$. Nevertheless, we can see from both Fig.3.7 and Fig.3.8 that the larger the spin, the larger the real part of the quasinormal modes and the smaller the imaginary part.

3.2.6 Conclusion and discussion

In this work, we study the phenomenology of gravitational perturbation around rotating hairy black holes. We first introduced the hairy black hole (3.50) and also used an approximation method to obtain the horizons analytically. Then we derived the master equations of the gravitational perturbation field including a radial part (3.60) and an angular part (3.61). Based on these equations, we studied the superradiance instability and quasinormal modes of the rotating hairy black holes.

For superradiance, we derived the conditions for superradiance to occur. The results show that amplification occurs when certain frequency criteria are met (3.83). Then, we calculated the amplification factor with low frequency approximations by using the matching-asymptotic technique. In the end, we obtained the formula to

calculate amplification factor (3.82) and plotted the $s = -2, l = m = 2$ modes with different parameters.

As for the quasinormal modes, we have calculated the quasinormal modes of the rotating hairy black hole numerically using the continued fraction method. We first present three tables (Table.3.4, 3.5, 3.6), and the columns $\alpha = 0$ in Table.3.4 and Table.3.6 could validate our numerical approaches. They agree very well with the previous results in the Kerr limit [139]. Then we demonstrated and drew several figures to show how the quasinormal modes change with the variation of different parameters: (a) fundamental quasinormal modes as a function of quantum number (l, m); (b) fundamental quasinormal modes as a function of black hole spin a; (c) fundamental quasinormal modes as a function of hairy parameters α, h_0; By fixing the other parameters respectively.

The results of both superradiance instability and quasinormal modes show that the rotating hairy black hole is different from a Kerr black hole. Although the discrepancies are small, one might still expect that this should have some consequences for observations such as GW, in particular the discovery and accurate identification of the ringdown signal could provide the 'smoking gun' for testing this rotating hairy black hole. We will continue these studies in the future.

Chapter 4

Energy extraction from alternative black holes via magnetic reconnection mechanism

This chapter is based on the following two first-author papers:

- **Energy extraction from rotating regular black hole via Comisso-Asenjo mechanism**
  Authors: **Zhen Li**, Xiao-Kan Guo and Faqiang Yuan
  Published in Phys.Rev.D, 108, 044067 (2023). arxiv: 2304.08831.
  Author contributions:
  Zhen Li proposed the idea and carried out all the figure plotting, code and draft writing, as well as the manuscript revision. Zhen Li also did the majority of the calculations. Xiao-Kan Guo and Faqiang Yuan calculated the light ring data in the parameter space figure. Xiao-Kan Guo and Faqiang Yuan also provided comprehensive feedback throughout the writing process and proofread the manuscript.

- **Energy extraction via Comisso-Asenjo mechanism from rotating hairy black hole**
  Authors: **Zhen Li**, Faqiang Yuan
  Published in Phys.Rev.D 108, 024039 (2023). arxiv: 2304.12553.
  Author contributions:
  Zhen Li proposed the idea and carried out all the figure plotting, code and draft writing, as well as the manuscript revision. Zhen Li also did the majority of the calculations. Faqiang Yuan calculated the light ring data in the parameter space figure. Faqiang Yuan also provided comprehensive feedback throughout the writing process and proofread the manuscript.

4.1 Energy extraction from rotating regular black hole

Abstract: Recently, it has been demonstrated by Comisso and Asenjo that magnetic reconnection processes in the ergosphere of a Kerr black hole can provide us with a promising mechanism for extracting the rotational energy from it. In this

paper, we study the energy extraction from the the newly proposed rotating regular black holes via this Comisso-Asenjo mechanism. This novel rotating regular black hole has an exponential convergence factor $e^{-k/r}$ on the mass term characterized by the regular parameter k in the exponent. We explore the effects of this regular parameter on the magnetic reconnection as well as other critical parameters determining the Comisso-Asenjo process. The parameter spaces allowing energy extraction to occur are investigated. The power, efficiency and the power ratio to the Blandford-Znajek mechanism are studied. The results show that the regularity of the rotating black hole has significant effects on the energy extraction via the Comisso-Asenjo mechanism.

4.1.1 Introduction

General relativity is the theory that best captures our present understandings of gravitational interaction. Gravitational waves [1, 53, 54] and black hole images [2, 55] have recently been observed, adding to the compelling evidences for general relativity. However, general relativity also encounters a number of difficulties and issues, of which the singularity problem in classical general relativity [3, 140] is the most severe one. It is generally accepted that singularities do not exist in nature and instead show the limits of general relativity. The regular black holes, which are solutions with horizons but are nonsingular in the sense that curvature invariants are finite everywhere, can offer an alternative solution for the singularity problem. In addition to the typical regular black hole solutions such as the Bardeen and Hayward regular black holes [60, 62, 141], many new regular black holes are derived and studied recently (cf. the review [142]). To construct such regular black hole solutions, one could modify the shape function in the black hole metric in such a way that the the curvature invariants are finite. A highly efficient way of obtaining regular solution is to multiply the mass function by an exponential factor $e^{-k/r}$, and many new regular black hole metrics have been generated by this approach [143, 10, 11, 144, 145, 146, 14, 13, 15, 16]. In particular, the regular rotating black hole obtained this way [14, 15, 16], which are different from those obtained by the Newman-Janis algorithm [147], have attracted lots of attention, but the phenomenological studies of such black holes are still very lacking. There are a few works exploring this aspect, mainly focusing on the black hole image and quasinormal mode effects [148, 149, 150, 152, 151], and therefore other astrophysical tests of regular rotating black holes are desirable.

A rapidly rotating black hole will produce an anti-parallel magnetic field configuration in the equatorial plane [153, 154]. Both numerical simulations [155, 156, 157, 158] and black hole image [2, 55] support that the main condition for this configuration is realistic. Comisso and Asenjo have shown in their remarkable paper [25] that this peculiar magnetic field configuration could lead to a fast magnetic reconnection process inside the ergosphere when the aspect ratio of the current sheet exceeds critical value [159, 160, 161], which can convert an amount of magnetic energy into plasma particle energy so that the plasma can escape from the reconnection layer. We will denote this new mechanism as the Comisso-Asenjo mechanism in order to distinguish with previous attempts in magnetic reconnection [162]. Comisso-Asenjo mechanism offers us a brand new way to extract energy from the rotating black holes. It has also been shown in many numerical simula-

tions that there is always a dominant point at which the reconnection process occurs [155, 157, 158]. In this Comisso-Asenjo magnetic reconnection process, one part of the plasma or flux is accelerated and another part is decelerated in the opposite direction. If the decelerated part has a negative energy and the accelerated part has an energy greater than its rest mass and thermal energy at infinity, the energy is extracted from the rotating black hole by magnetic reconnection [25]. The frame dragging effect of a rapidly rotating black hole causes this process to occur over and over again. In comparison with other energy extraction mechanisms, such as the Penrose process [163, 164] and the Blandford-Znajek mechanism [165], such a mechanism could be dominant in extracting the rotational energy of black holes.

The energy extraction via Comisso-Asenjo mechanism was first studied in the Kerr black hole [25] and recently extended to many other rotating black holes [166, 167, 168, 169, 170]. All the results show that the effects on the reconnection process of non-Kerr black holes are significantly different from the Kerr case. In this work, we aim to investigate the energy extraction from the rotating regular black hole via Comisso-Asenjo mechanism in the ergosphere. Because this process could potentially produce more high-energy astrophysical phenomena, it allows us to test the rotating regular black hole hypothesis across a wider observational range.

This section is organized as follows: We introduce the rotating regular black hole spacetime in subsection.4.1.2. Then in subsection.4.1.3, we will present the formulations of Comisso-Asenjo mechanism, especially the equations of plasma energy-at-infinity density per enthalpy and the conditions for energy extraction from a regular rotating black hole to occur. Next, based on the formulas in the last section, in subsection.4.1.4, we will explore the parameter spaces allowing energy extraction from the rotating regular black hole via Comisso-Asenjo mechanism. In subsection.4.1.5, we study the power and efficiency of this mechanism with different parameter combinations. We also compare the power ratio between the Comisso-Asenjo mechanism and the Blandford-Znajek mechanism in this section. In subsection.4.1.6, we will make a conclusion.

4.1.2 Rotating regular black hole

The metric of rotating regular black hole that we will discuss can be written in the Boyer-Lindquist coordinates as [15, 16],

$$ds^2 = g_{tt}dt^2 + g_{rr}dr^2 + g_{\theta\theta}d\theta^2 + g_{\phi\phi}d\phi^2 + 2g_{t\phi}dtd\phi \tag{4.1}$$

where the metric components are given by

$$\begin{aligned} g_{tt} &= -\left(1 - \frac{2Mre^{-k/r}}{\Sigma}\right) \qquad g_{t\phi} = -\frac{2aMre^{-k/r}}{\Sigma}\sin^2\theta \\ g_{rr} &= \frac{\Sigma}{\Delta} \qquad\qquad\qquad\qquad g_{\theta\theta} = \Sigma \\ g_{\phi\phi} &= \left(r^2 + a^2 + \frac{2Mra^2e^{-k/r}}{\Sigma}\sin^2\theta\right)\sin^2\theta \end{aligned} \tag{4.2}$$

with $\Sigma = r^2 + a^2\cos^2\theta$ and $\Delta = r^2 + a^2 - 2Mre^{-k/r}$. The mass, specific angular momentum, and regular parameters, M, a, and k, are assumed to be positive.

The Kerr metric could be retained when we set $k/r = 0$. Here and after, we use geometrized units with $G = c = 1$.

The solutions of equation

$$\Delta = r^2 + a^2 - 2Mre^{-k/r} = 0 \tag{4.3}$$

give the horizons. However, there are no analytical solutions. The numerical results of horizon structure as well as the ergosphere with different parameters were discussed in [14]. We will restrict our discussion on the value of regular parameter k such that (4.3) has two distinct real solutions (outer/event horizon and inner horizon), i.e, k should be less than the critical value k_c^{EH} which decreases as a increases.

Although the metric (4.1) mainly modifies the Kerr spacetime inside the event horizon, they also affect the spacetime outside the event horizon. One of the main purposes of this paper is to examine how the exponential convergence factor, represented by regular parameter k, affect the magnetic reconnection process in the ergosphere.

4.1.3 Energy extraction via Comisso-Asenjo mechanism

In this section, we present the Comisso-Asenjo formulas [25] of calculating the energy at infinity associated with accelerated/decelerated plasma in the spacetime (4.1). It is more convenient to evaluate the plasma energy density in the "zero-angular-momentum-observer" (ZAMO) frame [171]. The metric (4.1) in ZAMO frame takes the form of a Minkowski metric

$$ds^2 = -d\hat{t}^2 + \sum_{i=1}^{3} \left(d\hat{x}^i\right)^2 = \eta_{\mu\nu} d\hat{x}^\mu d\hat{x}^\nu \tag{4.4}$$

where

$$d\hat{t} = \alpha dt, \quad d\hat{x}^i = \sqrt{g_{ii}} dx^i - \alpha\beta^i dt \tag{4.5}$$

with

$$\alpha = \left(-g_{tt} + \frac{g_{\phi t}^2}{g_{\phi\phi}}\right)^{1/2}, \quad \beta^\phi = \frac{\sqrt{g_{\phi\phi}}\omega^\phi}{\alpha}. \tag{4.6}$$

We define $\omega^\phi = -g_{\phi t}/g_{\phi\phi}$ as the angular velocity of the frame dragging due to the rotating regular spacetime.

For a contra-variant vector a^μ in the Boyer-Lindquist coordinates, when transformed into the ZAMO frame, which we denote by $\hat{a}^\mu$, the following relation is obtained:

$$\hat{a}^0 = \alpha a^0, \quad \hat{a}^i = h_i a^i - \alpha\beta^i a^0 \tag{4.7}$$

and we also have the covariant vector $\hat{a}_\mu$ transformation relations

$$\hat{a}_0 = \frac{1}{\alpha} a_0 + \sum_i \frac{\beta^i}{h_i} a_i, \quad \hat{a}_i = \frac{1}{h_i} a_i. \tag{4.8}$$

The one-fluid approximation energy-momentum tensor of this system, in Boyer-Lindquist coordinates, takes form of

$$T^{\mu\nu} = pg^{\mu\nu} + wU^\mu U^\nu + F^\mu{}_\delta F^{\nu\delta} - \frac{1}{4} g^{\mu\nu} F^{\rho\delta} F_{\rho\delta} \tag{4.9}$$

where p, w, U^μ, and $F_{\mu\nu}$ are, respectively, the proper plasma pressure, enthalpy density, four-velocity, and electromagnetic field tensor. With this energy-momentum tensor, we can get the "energy-at-infinity" density $e^\infty = -\alpha g_{\mu 0} T^{\mu 0} = e^\infty_{hyd} + e^\infty_{em}$ [162], where e^∞_{hyd} and e^∞_{em} are, respectively, the hydrodynamic energy-at-infinity density and the electromagnetic energy-at-infinity density, and they are given by

$$\begin{aligned} e^\infty_{hyd} &= \alpha(w\hat{\gamma}^2 - p) + \alpha\beta^\phi w\hat{\gamma}^2\hat{v}^\phi \\ e^\infty_{em} &= \frac{\alpha}{2}(\hat{B}^2 + \hat{E}^2) + (\hat{\mathbf{B}} \times \hat{\mathbf{E}})_\phi \end{aligned} \tag{4.10}$$

where $\hat{\gamma} = \hat{U}^0 = 1/\sqrt{1 - \sum_{i=1}^3 (d\hat{v}^i)^2}$, $\hat{B}^i = \epsilon^{ijk}\hat{F}_{jk}/2$, $\hat{E}^i = \hat{F}_{i0}$ are the Lorentz factor, the components of magnetic and electric fields respectively. Here, v^ϕ denotes the azimuthal component of the plasma outflow velocity in the ZAMO frame [172]. The hat above these quantities means that we evaluate the quantity in the ZAMO frame.

Just as Comisso and Asenjo [25], we also assume that a considerable portion of the magnetic energy is converted into kinetic energy of plasma during the Comisso-Asenjo magnetic reconnection process, one can ignore the contribution of e^∞_{em} in the total energy, which leads to $e^\infty \approx e^\infty_{hyd}$. In addition, considering the plasma element is incompressible and adiabatic, we have [162]

$$e^\infty = \alpha\left(w(\hat{\gamma} + \beta^\phi\hat{\gamma}\hat{v}^\phi) + \frac{p}{\hat{\gamma}}\right). \tag{4.11}$$

One should note that the incompressible and adiabatic assumptions are consistent with each other. According to the incompressible approximation (see [162]), plasma fluid is made up of tiny, spatially separated elements with a constant volume. Similar to a soft ball, the element has a thin, light, closed, adiabatic skin and its volume is also constant. Here, we made the assumption that plasma gas pressure has no effect on the plasma and only has an inertia effect on the plasma dynamics. Due to the assumption that the plasma gas inside the ball is incompressible and adiabatic, the temperature in the ball is also expected to be constant.

We would like to introduce the local rest frame in order to investigate the localized magnetic reconnection process, $\bar{x}^\mu = (\bar{x}^0, \bar{x}^1, \bar{x}^2, \bar{x}^3)$, in which the directions of $\bar{x}^1$ and $\bar{x}^3$ are, respectively, parallel to the radial direction $\bar{x}^1 = r$ the azimuthal direction $\bar{x}^3 = \phi$. The local rest frame of plasma rotates with Keplerian angular velocity Ω_K in the equatorial plane from the perspective of Boyer-Lindquist observer, which is given by

$$\Omega_K = \frac{d\phi}{dt} = \frac{-g_{t\phi,r} + \sqrt{g^2_{t\phi,r} - g_{tt,r}g_{\phi\phi,r}}}{g_{\phi\phi,r}}. \tag{4.12}$$

Based on the transformation relation of vectors between Boyer-Lindquist and ZAMO coordinates, we can also obtain the above Keplerian angular velocity observed in the ZAMO frame, which is given by

$$\hat{v}^K = \frac{\Omega_K\sqrt{g_{\phi\phi}}}{\alpha} - \beta^\phi. \tag{4.13}$$

If we denote the outflow velocity observed in the local rest frame as v_{out}, then the outflow velocity observed in the ZAMO frame is

$$\hat{v}_{\pm}^{\phi} = \frac{\hat{v}^{K} \pm v_{out} cos(\xi)}{1 \pm \hat{v}_{K} v_{out} cos(\xi)} \tag{4.14}$$

where $\pm$ represent the outflow velocity with corotating (+) and counterrotating (-) direction relative to the rotation of the black hole. They also correspond to the accelerated part and decelerated part of the plasma, respectively. In (4.14), $\xi = arctan(\bar{v}^1/\bar{v}^3)$ is the plasma orientation angle, $\bar{v}^1$ and $\bar{v}^3$ are the radial and azimuthal components of plasma velocities in the local rest frame.

With the above equations (4.11) and (4.14), we can get the energy-at-infinity density of the reconnection outflows as

$$\begin{aligned} e_{\pm}^{\infty} =& \alpha\hat{\gamma}_{K} \left(\left(1 + \hat{v}_{K}\beta^{\phi}\right) \gamma_{out} w \pm \cos(\xi) \left(\hat{v}_{K} + \beta^{\phi}\right) \gamma_{out} v_{out} w \right. \\ & \left. - \frac{p}{\left(1 \pm \cos(\xi)\hat{v}_{K} v_{out}\right) \gamma_{out} \hat{\gamma}_{K}^{2}} \right) \end{aligned} \tag{4.15}$$

where $\gamma_{out} = 1/\sqrt{1 - v_{out}^2}$ and $\hat{\gamma}_{K} = 1/\sqrt{1 - \hat{v}_{K}^2}$. From [25], Comisso and Asenjo have derived that v_{out} is related to the properties of plasma magnetization and it could be expressed as

$$v_{out} = \sqrt{\frac{\sigma_0}{\sigma_0 + 1}} \tag{4.16}$$

where $\sigma_0 = B_0^2/w_0$ is the plasma magnetization upstream of the reconnection layer, B_0 is the asymptotic macroscale magnetic field and w_0 is the enthalpy density of the plasma. Then, the plasma energy-at-infinity density per enthalpy $\epsilon_{\pm}^{\infty} = e_{\pm}^{\infty}/w$ becomes [25]

$$\begin{aligned} \epsilon_{\pm}^{\infty} = \alpha\hat{\gamma}_{K} [& \left(1 + \beta^{\phi}\hat{v}_{K}\right) \left(1 + \sigma_0\right)^{1/2} \pm \cos(\xi) \left(\beta^{\phi} + \hat{v}_{K}\right) \sigma_0^{1/2} \\ & - \frac{1}{4} \frac{\left(1 + \sigma_0\right)^{1/2} \mp \cos(\xi)\hat{v}_{K}\sigma_0^{1/2}}{\hat{\gamma}_{K}^{2} \left(1 + \sigma_0 - \cos^2(\xi)\hat{v}_{K}^2\sigma_0\right)} \Bigg] \end{aligned} \tag{4.17}$$

where we have assumed that $p = w/4$. Eq.(4.17) has exactly the same form as the one in the Kerr black hole case (see [25]), and the differences are the geometry quantities that are now replaced by spacetime metric (4.1).

Just like in the Penrose process [163, 164], if the following conditions should be satisfied

$$\epsilon_{-}^{\infty} < 0, \quad \Delta\epsilon_{+}^{\infty} = \epsilon_{+}^{\infty} - \left(1 - \frac{\Gamma}{4(\Gamma - 1)}\right) > 0 \tag{4.18}$$

for a relativistic hot plasma, i.e. $\Gamma = 4/3$, then we have $\Delta\epsilon_{+}^{\infty} = \epsilon_{+}^{\infty}$. Consequently, black hole energy can only be extracted if the decelerated part of plasma in a magnetic reconnection process acquires negative energy as measurable at infinity, while the accelerated part of the plasma in the same magnetic reconnection process acquires energy at infinity larger than its rest mass and thermal energies.

4.1.4 Parameter spaces for energy extraction

The expression of energy at infinity Eq.(4.17) depends on several critical parameters: the black hole mass M, the black hole spin a, the dominant reconnection radial location r (so-called X point [155, 157, 158, 25]), the plasma magnetization σ_0, the orientation angle ξ and the regular parameter k. For simplicity, we will choose units by setting $M = 1$ in the rest of this paper, then a, r, and k are measurable in the unit of M, while σ_0 and ξ are dimensionless parameters.

Now, we will show that Comisso-Asenjo mechanism is a viable mechanism to extract energy from regular rotating black holes in a significant range of parameter spaces. In order to compare with the literature, the structure of figures in this section are in reference to the Comisso and Asenjo original paper [25].

First, let us consider how the orientation angle ξ and plasma magnetization σ_0 affect the energy-at-infinity per enthalpy ϵ_+^∞ and ϵ_-^∞. For this purpose, taking $r = 1.5$, $a = 0.89$ and $k = 0.1$, we plot ϵ_+^∞ and ϵ_-^∞ as a function of σ_0 with different ξ in Fig.4.1. We can see that ϵ_+^∞ increases with the plasma magnetization σ_0 while

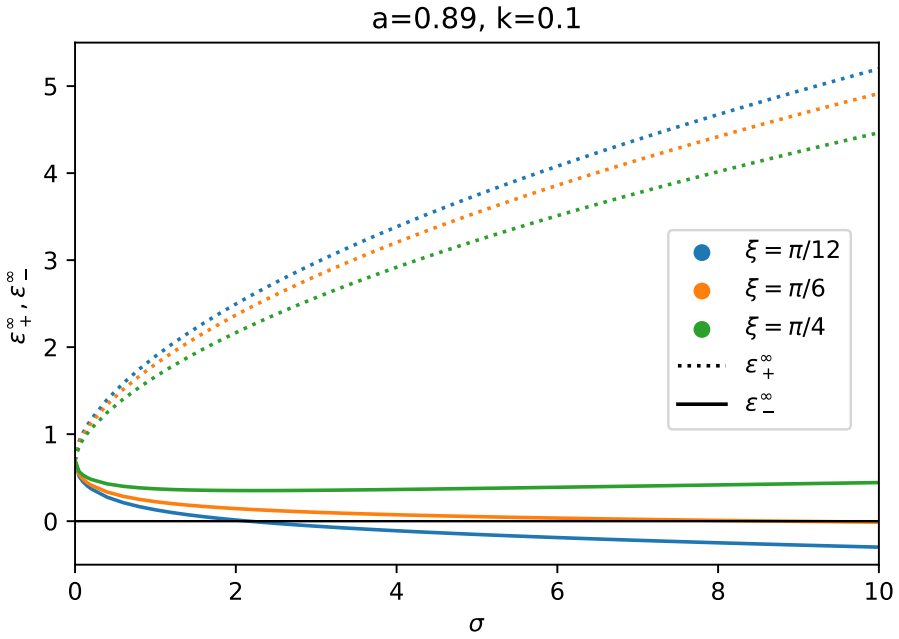

Figure 4.1: The behaviors of ϵ_+^∞ (dotted curve) and ϵ_-^∞ (solid curve) as a function of plasma magnetization $\sigma_0 \in [0, 10]$, with different orientation angle $\xi = \pi/12, \pi/6, \pi/4$. The dominant reconnection radial location is taken as $r = 1.5$, with black hole spin $a = 0.89$ and regular parameter $k = 0.1$. The black solid line is $\epsilon_+^\infty = \epsilon_-^\infty = 0$ as reference.

ϵ_-^∞ decreases with the plasma magnetization σ_0. It is easy to satisfy the condition $\Delta\epsilon_+^\infty = \epsilon_+^\infty > 0$, however, the orientation angle is essential for ϵ_-^∞ to be negative. In order to satisfy the energy extraction conditions (4.18), the orientation angle should be small enough. The restriction could be relaxed if the plasma magnetization σ_0 is large enough since it can subtract the increase of ϵ_-^∞ due to increase of orientation angle ξ.

To investigate the impact of regular parameter k on ϵ_+^∞ and ϵ_-^∞, we plot ϵ_+^∞ and ϵ_-^∞ as a function of regular parameter k in Fig.4.2 by taking $r = 1.6$, $a = 0.89$ and $\xi = \pi/12$ with different plasma magnetization σ_0. From both upper plot and lower plot, we can see that ϵ_+^∞ and ϵ_-^∞ all decrease as the regular parameter k increases. Again, $\epsilon_+^\infty > 0$ is well satisfied regardless of what the plasma magnetization σ_0 is. However, in order to extract energy from the black hole, the condition $\epsilon_-^\infty < 0$ is not so straightforward to be met. It requires that the regular parameter k should be large enough. What is more, from both plots, we can see that a large plasma magnetization σ_0 is always beneficial for extracting energy from the black hole.

Let us now examine the parameter space of the dominant reconnection radial location r and black hole spin a that permit the realization of energy extraction from black hole via magnetic reconnection. The results are shown in two-dimensional $r-a$ parameter space plots, see Fig.4.3 and Fig.4.4. In Fig.4.3, we have three plots, they correspond to different regular parameters $k = 0, 0.05, 0.1$, respectively by taking $\xi = \pi/12$. The $k = 0$ case is the Kerr black hole as reference. The critical black hole spin, under which the rotating black hole has two horizons, decreases as the regular parameter k increases. We only show the region below those critical black hole spin. As the regular parameter k increase, the radii of the outer event horizon and outer ergosphere decrease while that of the light ring increases. The allowed region for $\epsilon_+^\infty > 0$ (gray area) is widening in the r dimension while shrinking in the a dimension. The regions where $\epsilon_-^\infty < 0$ have a great dependency on the plasma magnetization σ_0; the larger σ_0, the larger the region with $\epsilon_-^\infty < 0$. The increase in the regular parameter k will make smaller the black hole spin a available for $\epsilon_-^\infty < 0$. Regarding Fig.4.4, we aim to exam the effects of orientation angle ξ on the $r - a$ parameter space by taking $\sigma_0 = 100$, $k = 0.1$. We can see that the smaller orientation angle ξ, the larger region with $\epsilon_-^\infty < 0$.

4.1.5 Energy extraction power and efficiency

The power and efficiency of energy extraction via the Comisso-Asenjo mechanism are significant to the black hole evolution and its astrophysical phenomena. In this section, we will investigate the energy extraction power and efficiency of the rotating regular black hole (4.1). In [25], Comisso and Asenjo have proposed that these two quantities essentially depend on how quick the plasma with negative energy-at-infinity density are absorbed by the black hole per unit time. The power can be well estimated by [25]

$$P_{etr} = -\epsilon_-^\infty w_0 A_{in} U_{in} \tag{4.19}$$

where the reconnection inflow four-velocity $U_{in} = \mathcal{O}(10^{-1})$ and $\mathcal{O}(10^{-2})$, respectively, refer to the collisionless [173, 174, 175] and collisional regimes [176, 177]. A_{in} is the cross-sectional area of the inflowing plasma, which can be estimated as $A_{in} \sim r_E^2 - r_{ph}^2$ for rapid rotating regular black holes, with r_E and r_{ph} are the outer ergosphere and light ring of the rotating regular black hole respectively.

We will investigate the power mainly in the collisionless regime, which is consist with [25], and it also allows for a higher energy extraction rate than the collisional regime.

In Fig.4.5, we demonstrate the ratio P_{etr}/w_0 as a function of the dominant reconnection radial location r for a rapidly spinning black hole (4.1) in the collisionless

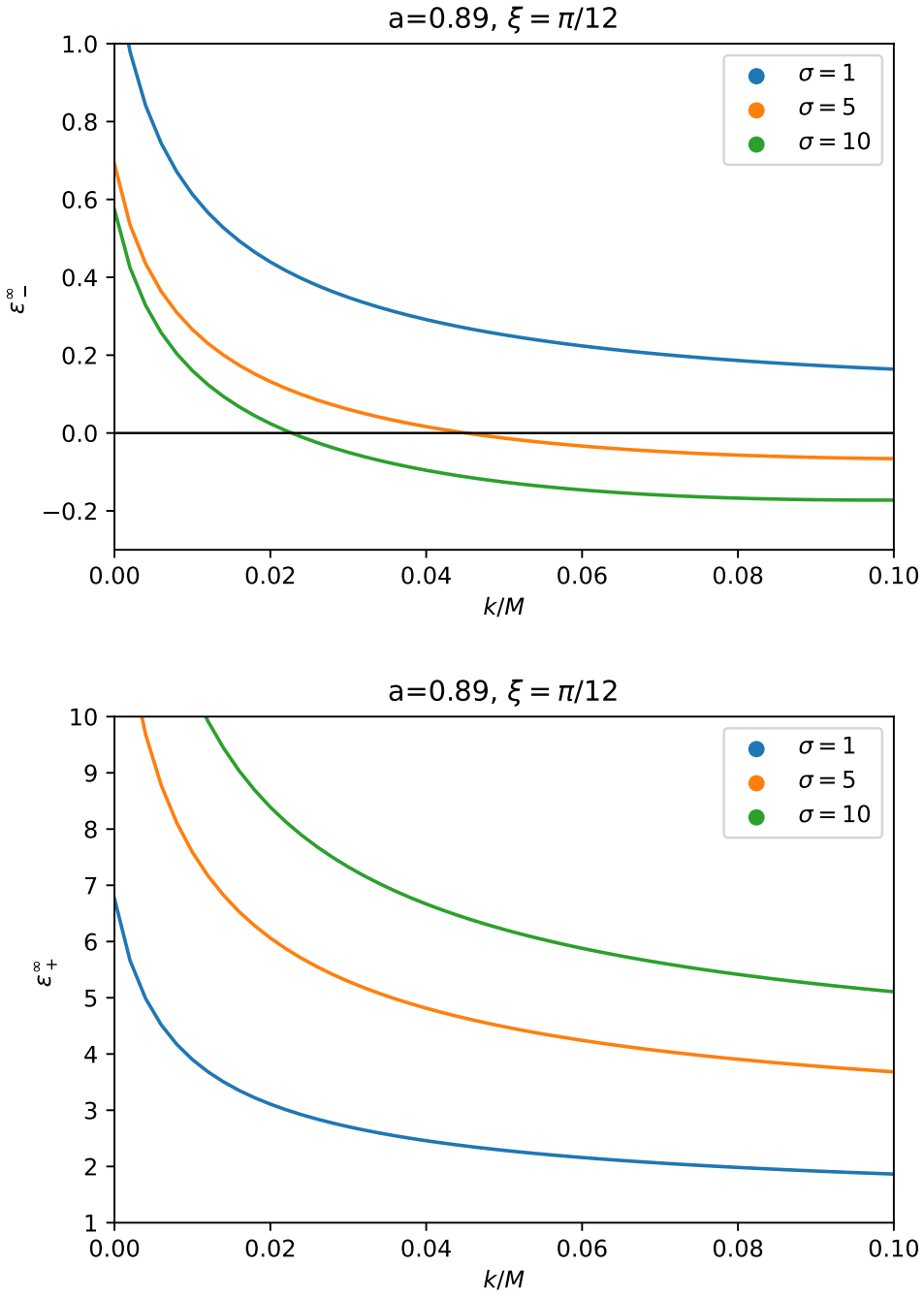

Figure 4.2: The behaviors of ϵ^{∞}_{-} (upper plot) and ϵ^{∞}_{+} (lower plot) as a function of the regular parameter $k \in [0, 0.1]$, with different plasma magnetization $\sigma_0 = 1, 5, 10$. The dominant reconnection radial location is taken as $r = 1.6$, with black hole spin $a = 0.89$ and orientation angle $\xi = \pi/12$. The black solid line in the upper plot is $\epsilon^{\infty}_{-} = 0$ as reference.

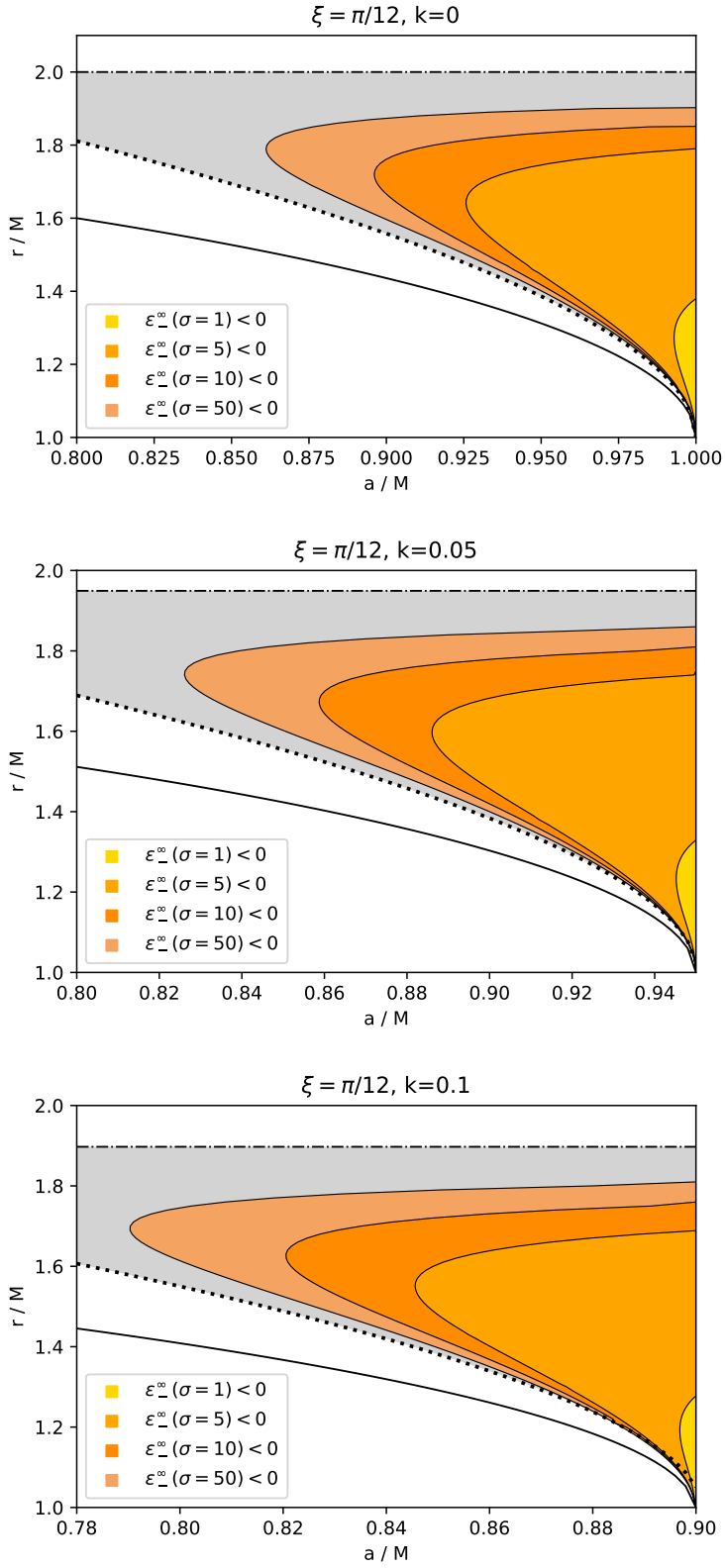

Figure 4.3: The parameter space $(r-a)$ with $\xi = \pi/12$ and three different regular parameters $k = 0$ (upper plot), 0.05(middle plot), and 0.1(lower plot). The colored regions are $\epsilon^{\infty}_{-} < 0$ with $\sigma_0 = 1, 5, 10, 50$. The gray area is the region where $\epsilon^{\infty}_{+} > 0$. Black solid curves, black dotted curves, and black dot dashed curves are the radii of the outer event horizon, light ring, and outer ergosphere respectively.

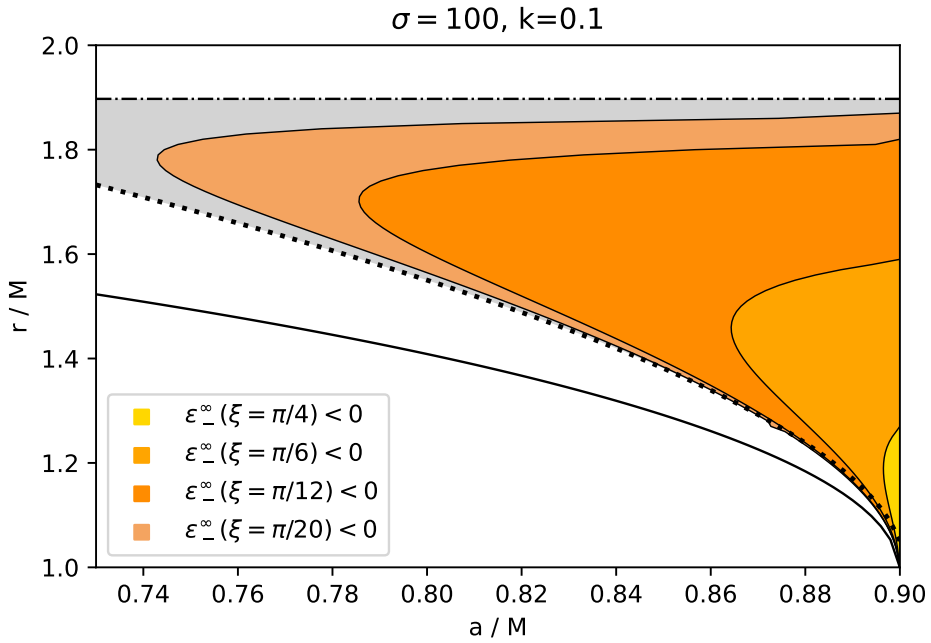

Figure 4.4: The parameter space $(r - a)$ with $\sigma_0 = 100$, $k = 0.1$ and different orientation angle ξ. The colored regions are $\epsilon^{\infty}_{-} < 0$ with $\xi = \pi/20, \pi/12, \pi/6, \pi/4$ respectively. The gray area is the region where $\epsilon^{\infty}_{+} > 0$. Black solid curves, black dotted curves, and black dot dashed curves are the radii of the outer event horizon, light ring, and outer ergosphere respectively.

regime $U_{in} = 0.1$, with different plasma magnetization $\sigma_0 = 10, 100, 1000, 10000$ by taking $a = 0.89$, $\xi = \pi/12$ and $k = 0.1$. As the plasma magnetization σ_0 increases, the power extracted from the black hole rises monotonically. The power peaks at those positions near the limiting circular orbit or light ring and then gradually declines.

We also show the ratio P_{etr}/w_0 as a function of the regular parameter k in Fig.4.6. with different plasma magnetization $\sigma_0 = 10, 100, 1000, 10000$ by taking $r = 1.5$, $a = 0.89$, $\xi = \pi/12$ and $U_{in} = 0.1$. The power increases monotonically for the increasing values of the regular parameter k. In addition, along with the plasma magnetization σ_0, the power rises monotonically as well.

Next, we evaluate the efficiency of energy extraction. It is convenient to define the efficiency as [25]

$$\eta = \frac{\epsilon^{\infty}_{+}}{\epsilon^{\infty}_{+} + \epsilon^{\infty}_{-}}. \tag{4.20}$$

If $\eta > 1$, then the energy will be extracted from the rotating regular black hole.

In Fig.4.7, we show the efficiency η as a function of the dominant reconnection radial location r with different black hole spin $a = 0.87, 0.88, 0.89, 0.90$, taking $\sigma = 100$, $\xi = \pi/12$, $k = 0.1$. Note that when $a = 0.90$, the black hole is an extreme one for $k = 0.10$. As reference, we also plot the efficiency for the extreme black hole. Regarding the nonextremal case, we can see from Fig.4.7 that the efficiency significantly increases with location r that is closer to the outer event horizon and decreases below unity when it is close to the ergosphere. Thus, there are peaks for

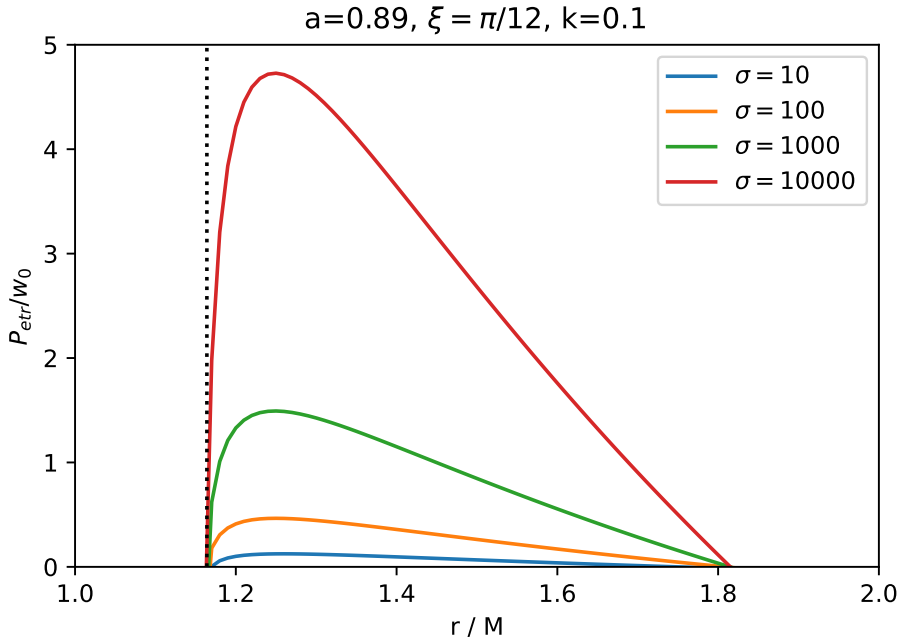

Figure 4.5: P_{etr}/w_0 as a function of the dominant reconnection radial location r with different plasma magnetization $\sigma_0 = 10, 100, 1000, 10000$, by taking $a = 0.89$, $\xi = \pi/12$, $k = 0.1$, and $U_{in} = 0.1$. The vertical dotted line indicates the limiting circular orbit, i.e., light ring r_{ph}.

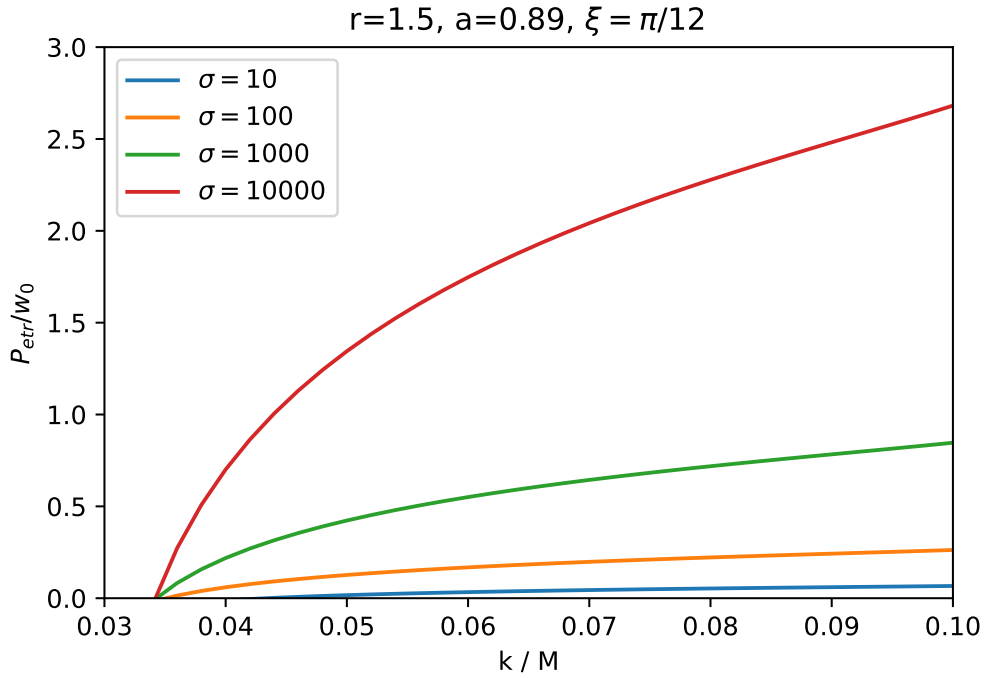

Figure 4.6: P_{etr}/w_0 as a function of the regular parameter k with different plasma magnetization $\sigma_0 = 10, 100, 1000, 10000$, by taking $r = 1.5$, $a = 0.89$, $\xi = \pi/12$ and $U_{in} = 0.1$.

efficiency and the peaks go to a large value and shift to a small location r when black hole spin a increases.

In order to study the role of the regular parameter k on the efficiency, we plot the efficiency as a function of the regular parameter k with different plasma magnetization $\sigma_0 = 10, 100, 1000, 1000$ in Fig.4.8, taking $r = 1.5$, $a = 0.89$ $\xi = \pi/12$. We can see that the efficiency grows monotonically along with the increasing of regular parameter k. The effects of plasma magnetization σ_0 on the efficiency is dropping exponentially as σ_0 grows and is almost the same for sufficiently large values.

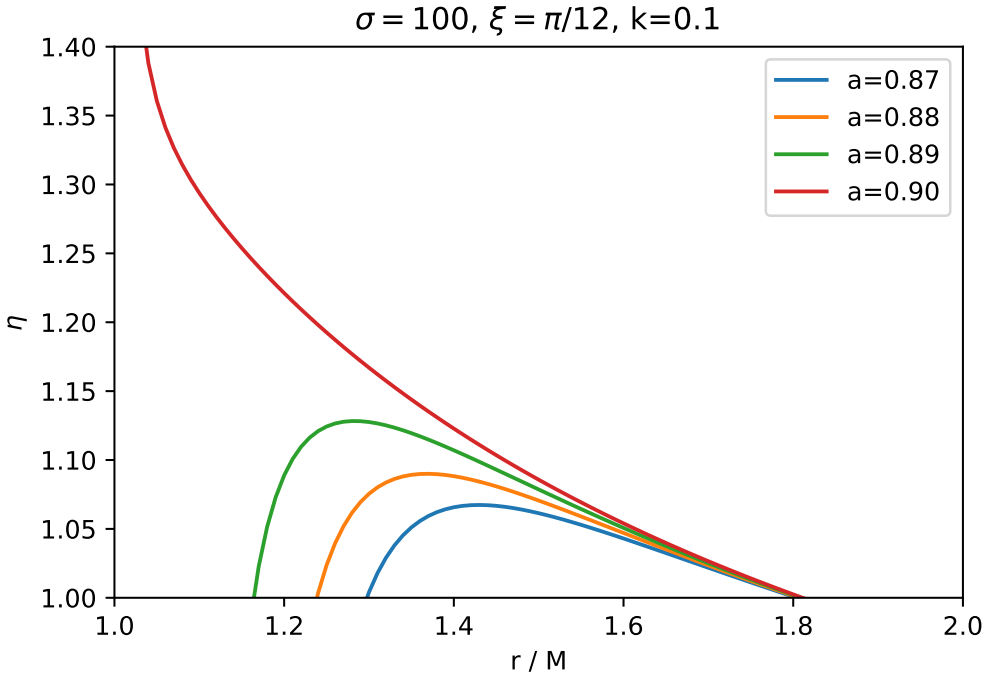

Figure 4.7: Efficiency η of the magnetic reconnection process as a function of the dominant reconnection radial location r with different black hole spin $a = 0.87, 0.88, 0.89, 0.90$, taking $\sigma = 100$, $\xi = \pi/12$, $k = 0.1$. Note that the $a = 0.90$ case is the extreme black hole for $k = 0.10$.

Last but not least, we compare the powers of the energy extractions via the Comisso-Asenjoand Blandford-Znajek mechanisms, in the latter of which the black hole rotation energy is extracted through a magnetic field that threads the event horizon. Regarding the Blandford-Znajek mechanism, in the so-called maximum efficiency conditions [178, 179, 180], the power of energy extraction is given by [165, 181, 182]

$$P_{BZ} = \frac{\kappa}{16\pi}\Phi_H^2(\Omega_H^2 + C_1\Omega_H^4 + C_2\Omega_H^6 + \mathcal{O}(\Omega_H^8)) \tag{4.21}$$

where κ is a numerical constant related to the magnetic field configuration and C_1, C_2 are numerical coefficients. The magnetic flux crossing the black hole event horizon is given by $\Phi_H = \frac{1}{2}\int_\theta\int_\phi |B_r|\sqrt{-g}d\theta d\phi = 2\pi(r_+^2 + a^2)B_0 sin(\xi)$, where r_+ is the event horizon. The angular velocity at the event horizon is $\Omega_H = 2ar_+e^{-k/r_+}/\left(r_+^2 + a^2\right)^2$. We assume that the difference in the spacetime metric will

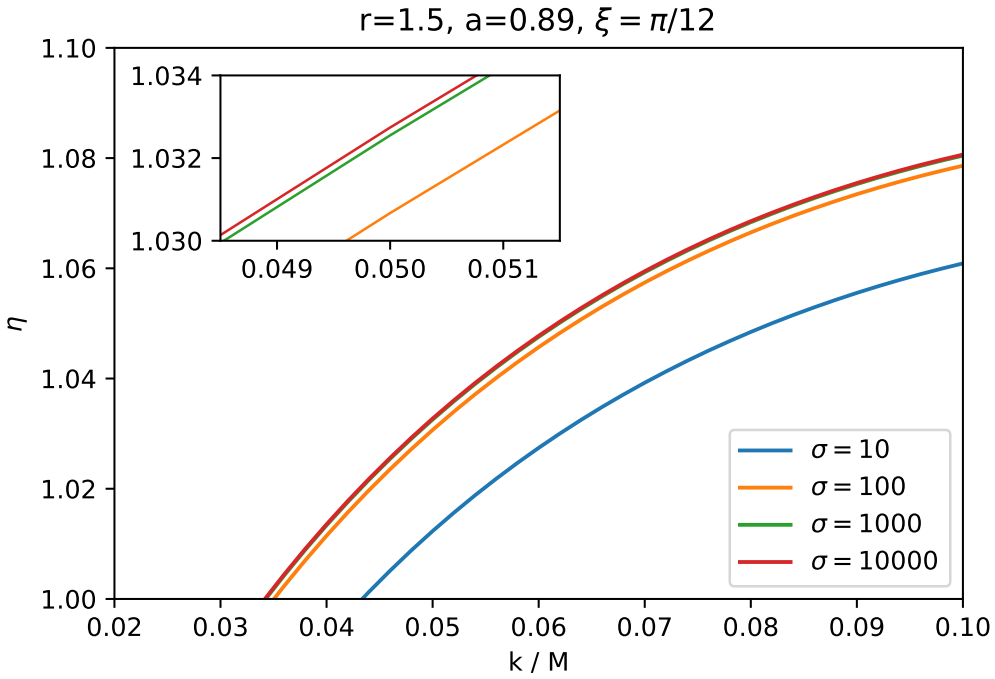

Figure 4.8: Efficiency η of the magnetic reconnection process as a function of the regular parameter k with different plasma magnetization $\sigma_0 = 10, 100, 1000, 1000$, taking $r = 1.5$, $a = 0.89$ $\xi = \pi/12$.

only affect the Blandford-Znajek process through geometry quantities, since the basic magnetic field configurations are the same to the Kerr case. Thus, we have only modified the geometry quantities in the Blandford-Znajek power of Kerr black hole and obtain Eq.(4.21). Then, the power ratio between these two mechanism is

$$\frac{P_{etr}}{P_{BZ}} \sim \frac{-4\epsilon_{-}^{\infty} A_{in} U_{in}}{\pi\kappa\sigma_0(r_{+}^2 + a^2)^2 sin^2(\xi)(\Omega_H^2 + C_1\Omega_H^4 + C_2\Omega_H^6)}. \tag{4.22}$$

By taking $\xi = \pi/12$, $\kappa = 0.05$, $C_1 = 1.38$, $C_2 = -9.2$ respectively [25], we show the power ratio in Fig.4.9 as a function the plasma magnetization σ_0 with different dominant reconnection radial location $r = 1.3, 1.5, 1.7$, the near-extreme black hole spin $a = 0.89, 0.99$ corresponding to regular parameter $k = 0.1, 0$ respectively. We can see that all the power ratios rise sharply along with the plasma magnetization that is closer to the critical value, and then after their maximum value are attained, the power ratios drop along with the plasma magnetization. The reason why the power ratios Eq.(4.22) decrease as the increase in the plasma magnetization is the different dependency on the plasma magnetization. Since when $\sigma_0 \to \infty$, we have $P_{etr} \sim \sigma_0^{1/2}$ and $P_{BZ} \sim \sigma_0$, thus $P_{etr}/P_{BZ} \sim 1/\sigma_0^{1/2}$, which decrease with the increase in plasma magnetization. On the other hand, when $\sigma_0 \sim 1$, the force-free electrodynamics approximation [165, 181, 182] of Blandford-Znajek power becomes invalid. It is necessary to examine the energy and angular momentum carried onto the rotating regular black hole by the accreting plasmas. In this scenario, the power ratios can only be seen as an effective or rough comparison. We also found that the smaller the dominant reconnection radial location r, the larger the power ratios. In

addition, the power ratio of Kerr black hole ($k = 0$) is greater than the regular black hole ($k = 0.1$), which shows that, compared with the Kerr black hole, the Comisso-Asenjo mechanism is less effective at extracting energy from a regular black hole. Nevertheless, in a very broad parameter range of the plasma magnetization σ_0, the power ratio is greater than 1, which means that the Comisso-Asenj mechanism is a very promising and an important energy extraction mechanism from rotating regular black holes.

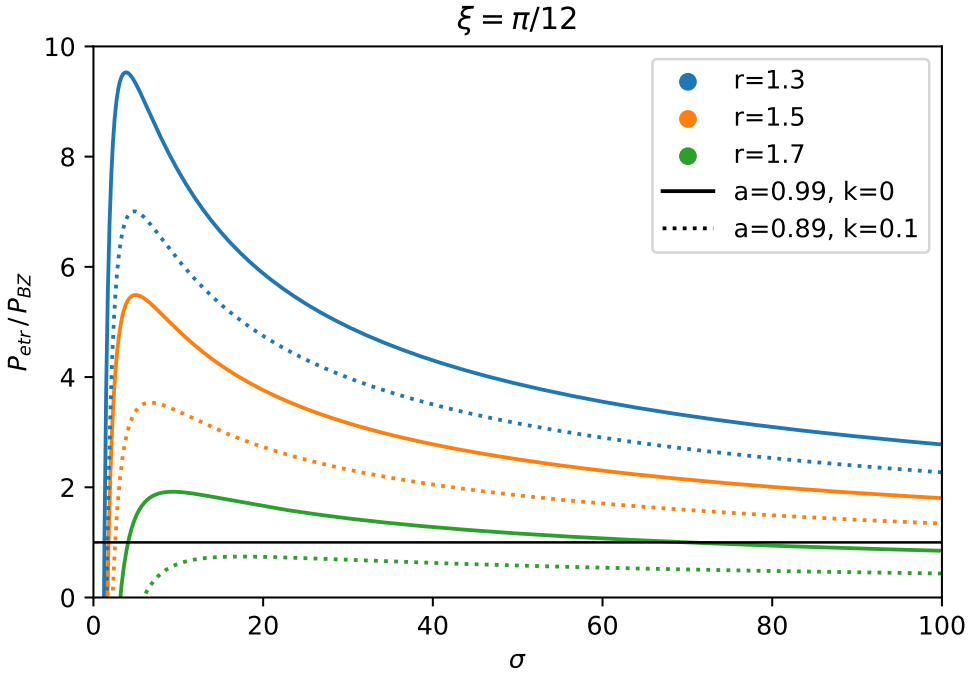

Figure 4.9: Power ratio P_{etr}/P_{BZ} as a function of the plasma magnetization σ_0 with different dominant reconnection radial location $r = 1.3, 1.5, 1.7$ and $[a = 0.89, k = 0.1]$(dotted curve), $[a = 0.99, k = 0]$ (solid curve), by taking the orientation angle $\xi = \pi/12$. The coefficients are taken as $\kappa = 0.05$, $C_1 = 1.38$, $C_2 = -9.2$ respectively. The black solid line is $P_{etr}/P_{BZ} = 1$ as reference.

4.1.6 Conclusion

Rotating regular black hole (4.1) is a very promising solution to the singularity problem in general relativity. In order to verify this proposal, the phenomenological study of this spacetime is essential. In this work, we investigated the energy extraction from a rotating regular black hole (4.1) caused by Comisso-Asenj magnetic reconnection process within the ergosphere.

With the assumption that a considerable portion of the magnetic energy is converted into kinetic energy of plasma during reconnections, we first present the Comisso-Asenjo formulas of the plasma energy at infinity (4.17) associated with the accelerated and decelerated part of the same reconnection process as well as the conditions (4.18) for extracting energy from the rotating regular black hole.

Then we specifically studied how the plasma magnetization, orientation angle and especially the regular parameter will affect the behavior of the plasma energy-at-infinity per enthalpy ϵ_+^∞ and ϵ_-^∞, by taking black hole spin and dominant reconnection radial location as certain values. It turns out that the small value of orientation angle and large values of plasma magnetization and regular parameter will be beneficial for the energy extraction via magnetic reconnection from the rotating regular black hole. What is more, in order to explore the effects of the other parameters settled down, we demonstrated the two dimensional $(r - a)$ parameter space that satisfies the conditions (4.18). We also show the effects of different regular parameter, plasma magnetization and orientation angle in the same figures such that we can fully explore the parameter spaces.

In the subsequent section, we also studied how these critical parameters will affect the power and efficiency of the energy extraction via the magnetic reconnection. The power and efficiency all grow with the increasing of regular parameter. It is interesting that the plasma magnetization almost has no effect to the efficiency when it becomes large enough.

Finally, we studied the power ratio of the energy extraction via the Comisso-Asenjo mechanism to the famous Blandford-Znajek mechanism. In a sufficient large parameter range, the energy extraction via Comisso-Asenjo process is more powerful than the Blandford-Znajek mechanism for extracting energy from the rotating regular black hole. In addition, the Kerr case ($k = 0$) is more efficient than the regular black hole case ($k = 0.1$).

4.2 Energy extraction from rotating hairy black hole

Abstract: It was demonstrated by Comisso and Asenjo that the magnetic reconnection in the ergosphere is a promising mechanism to extract energy from the rotating Kerr black hole. In this work, we investigate the role of the Comisso-Asenjo mechanism in energy extraction from the newly suggested rotating hairy black holes which have an extra hair due to the additional surrounding sources, such as dark matter or dark energy. We examine how the hairy parameters characterized the hair affect the magnetic reconnection process in addition to other important variables of the Comisso-Asenjo process, including the parameter spaces that permit energy extraction, the power, efficiency and power ratios with respect to the Blandford-Znajek mechanism.

4.2.1 Introduction

It is widely accepted that the physically rotating black holes in the Universe are described by the Kerr metric, which are characterized by two parameters, i.e., the mass and the spin. The famous No Hair theorem in classical general relativity [5, 6, 7, 8, 9] also states that the Kerr metric has no other 'hair' besides the mass and spin. However, the unknown dark matter and dark energy, which may originate from new fundamental fields, could be an additional source of the black hole such that Kerr black holes obtain a new hair and deviate from the Kerr metric [113]. Based on this novel idea, recently, the hairy black hole and later its rotating counterpart were

obtained using the gravitational decoupling approach (GD) [17, 18] which has been created expressly to describe the deformation of known solutions of general relativity brought on by additional sources [114, 115]. There are numerous theoretical and observational investigations on this (rotating) hairy black hole [116, 117, 118, 119, 120, 121, 183, 184].

A fast rotating black hole, on the other hand, will result in an antiparallel magnetic field configuration in the equatorial plane [153, 154]. Comisso and Asenjo have shown that, when the aspect ratio of the current sheet approaches a critical value [159, 160, 161], this distinctive magnetic field configuration could result in a quick magnetic reconnection process inside the ergosphere, which is capable of converting a large amount of magnetic energy into the kinematic energy of the plasma particles which escape from the black hole to infinity [25]. In order to distinguish this new mechanism from the earlier attempt [162] at magnetic reconnection, we will refer to it as the Comisso-Asenjo mechanism. Numerous numerical simulations have also demonstrated that the Comisso-Asenjo reconnection process always occurs at a dominant point [155, 157, 158]. This process keeps repeating due to the frame-dragging effect of the rotating black hole. Such a mechanism might be more effective than others for extracting the rotational energy from black holes, such as the Penrose process [163, 164] and the Blandford-Znajek mechanism [165]. The Kerr black hole was the first black hole to be studied with energy extraction via the Comisso-Asenjo mechanism [25] and most lately applied to the other rotating black holes [166, 167, 168, 169, 170, 185].

In this work, we look into the role of the Comisso-Asenjo mechanism in the energy extraction from the rotating hairy black hole. Since this process may result in more high energy astrophysical phenomena, therefore, this work may provide us phenomenological insights on testing the rotating hairy black hole as well as the No Hair theorem over a larger spectrum of future observations.

The structure of this section is as follows: The rotating hairy black hole spacetime is presented in subsection.4.2.2. Then in subsection.4.2.3, the Comisso-Asenjo mechanism formulas will be discussed, along with the equations for plasma energy at infinity density per enthalpy and the conditions for energy extraction. Next in subsection.4.2.4, use the Comisso-Asenjo mechanism formulas in the previous section, we will look into the magnetic reconnection parameter spaces for energy extraction. In subsection.4.2.5, we examine the power and efficiency of the Comisso-Asenjo mechanism using a variety of parameter combinations. In this section, we also examine the power ratios of the Comisso-Asenjo mechanism comparing to the Blandford-Znajek mechanism. At last, we will make a conclusion in subsection.4.2.6.

4.2.2 Rotating hairy black hole

The GD method, which is specifically created to find deformation of the known solution of GR [114, 115], was used to derive a rotating hairy black hole in [18]. Its line element square can be read as follows in the Boyer-Lindquist coordinates:

$$ds^2 = g_{tt}dt^2 + g_{rr}dr^2 + g_{\theta\theta}d\theta^2 + g_{\phi\phi}d\phi^2 + 2g_{t\phi}dtd\phi \tag{4.23}$$

where the metrics are provided by

$$\begin{aligned} g_{tt} &= -\left[\frac{\Delta - a^2\sin^2\theta}{\Sigma}\right] & g_{rr} &= \frac{\Sigma}{\Delta} \\ g_{t\phi} &= -a\sin^2\theta\left[1 - \frac{\Delta - a^2\sin^2\theta}{\Sigma}\right] & g_{\theta\theta} &= \Sigma \\ g_{\phi\phi} &= \sin^2\theta\left[\Sigma + a^2\sin^2\theta\left(2 - \frac{\Delta - a^2\sin^2\theta}{\Sigma}\right)\right] \end{aligned} \tag{4.24}$$

with $\Delta = r^2 + a^2 - 2Mr + \lambda r^2 e^{-r/\left(M-\frac{h_0}{2}\right)}$, and $\Sigma = r^2 + a^2\cos^2\theta$. M, a denote the black hole mass and spin. The primary hair h_0 measures the rise in entropy generated by the hair and must meet the requirement $h_0 \leq 2M \equiv h_K$ in order to achieve asymptotic flatness. λ measures deviation from the standard Kerr black holes and is related to h_0 via the equation $h_0 = \lambda h$. The Kerr metric, which denotes the absence of surrounding matter, is what this spacetime reduces to when $\lambda = 0$.

We will get horizons from the equation below

$$\Delta = r^2 + a^2 - 2Mr + \lambda r^2 e^{-r/\left(M-\frac{h_0}{2}\right)} = 0 \tag{4.25}$$

Analytical solutions, however, do not exist. In [117], it was discussed how different hairy parameters affected the numerical results of the horizon structure and the ergosphere. We will restrict our discussion on the regime of hairy parameters such that (4.25) has two distinct real solutions (see[117]).

4.2.3 Energy extraction via the Comisso-Asenjo mechanism

One part of the plasma accelerates during the Comisso-Asenjo magnetic reconnection process while the opposing direction part decelerates. If the accelerated half has an energy larger than its rest mass and thermal energy at infinity and the decelerated part has a negative energy, then the energy is extracted from the rotating black hole by the Comisso-Asenjo mechanism [25]. The formula of the Comisso-Asenjo mechanism was already presented in subsubsection.4.1.3. To discuss this mechanism in the rotating hairy black hole scenario, we just need to replace the metric components in subsubsection.4.1.3 with the quantities specified in (4.23). So, we will go directly to the results in the next section.

4.2.4 Parameter spaces for energy extraction

The plasma energy at infinity density (4.17) depends on several critical parameters: the black hole mass M, the black hole spin a, the dominant reconnection radial location r, the plasma magnetization σ_0, the orientation angle ξ, and the hairy parameters λ and h_0. For simplicity, we will choose units by setting $M = 1$ in the rest of this paper, then a, r and h_0 are measured in the unit of M. λ, σ_0 and ξ are dimensionless parameters.

We will now demonstrate that, in a sizable range of parameter spaces, the Comisso-Asenjo mechanism is a viable process to extract energy from hairy rotating black holes. In order to examine the effects of both hairy parameters λ and h_0

on the magnetic reconnection and simplify our discussion, we choose four different combinations of hairy parameter in the following analysis, which take two typical values for each hairy parameter in its dominate range and permute them. As a result, we will use the following combinations: $(\lambda = 0.5, h_0 = 0.5)$, $(\lambda = 0.5, h_0 = 1.5)$, $(\lambda = 1, h_0 = 1.5)$ and $(\lambda = 1, h_0 = 0.5)$.

We first show the behavior of ϵ_+^∞ and ϵ_-^∞ as a function of plasma magnetization σ_0 in Fig.4.10, taking $r = 1.5$ and $\xi = \pi/12$ with four different combinations of hairy parameter and its corresponding maximal black hole spin for which it has two horizons. We can see that ϵ_+^∞ increases along with σ_0 while the ϵ_-^∞ decreases. In the entire range, $\epsilon_+^\infty > 0$ and $\epsilon_-^\infty < 0$ when $\sigma_0 \gtrsim 2$ for all the combinations of hairy parameter, which implies that meeting the conditions (4.18) is easy and it is very effective to extract energy from the hairy black hole via magnetic reconnection in the sufficient parameter range. Although the differences of ϵ_+^∞ and ϵ_-^∞ between different combinations of hairy parameter are small, there are still notable information: the bigger the maximal black hole spin which the hairy parameter combination corresponds to, the larger ϵ_+^∞ and smaller ϵ_-^∞, almost the same when their maximal black hole spin are equal. That is to say that extract energy via the magnetic reconnection process has a positive correlation with the black hole spin. It may be easy to understand this since the higher black hole spin means more rotational energy. In addition, we also find that the difference of ϵ_+^∞ and ϵ_-^∞ between different λ almost disappear when $h_0 = 1.5$, while the differences become notable when $h_0 = 0.5$. We can conclude that in order to let the effect of the hairy parameter λ be significant, h_0 should be sufficiently small.

To better understand how the black hole spin affects the energy extraction via magnetic reconnection, we plot the two dimensional $(r - a)$ parameter space in Fig.4.11 and Fig.4.12. For the four subplots of Fig.4.11, they correspond to four combinations of hairy parameter. The maximal black hole spin, under which the rotating hairy black hole has two horizons, is different. We found that the smaller black hole spin requires a relatively large radial location r such that the energy extraction via the magnetic reconnection mechanism works. As we discussed before, here the parameter spaces for $(\lambda = 0.5, h_0 = 1.5)$ and $(\lambda = 1, h_0 = 1.5)$ are almost the same, this prove again that the effects of λ depend on how small the value of h_0 is. When $h_0 = 0.5$, λ indeed causes a difference in the parameter space as well as the radii of the outer event horizon, light ring and outer ergosphere. In Fig.4.12, we aim to examine the effects of orientation angle ξ on the $(r - a)$ parameter space by taking $\sigma_0 = 100$, $\lambda = 0.5$, and $h_0 = 1.5$. We can see that the smaller orientation angle ξ, the larger the region allowing to extract energy from the rotating hairy black hole via magnetic reconnection mechanism.

4.2.5 Energy extraction power and efficiency

Black hole evolution and its associated astrophysical phenomenon depend significantly on the power and efficiency of energy extraction via the Comisso-Asenjo mechanism. We will examine the energy extraction power and efficiency form the rotating hairy black hole. Comisso and Asenjo have proposed that [25] these two quantities mostly depend on the rate at which plasma with negative energy-at-infinity density is absorbed. We denote the power as P_{etr} and it can be well esti-

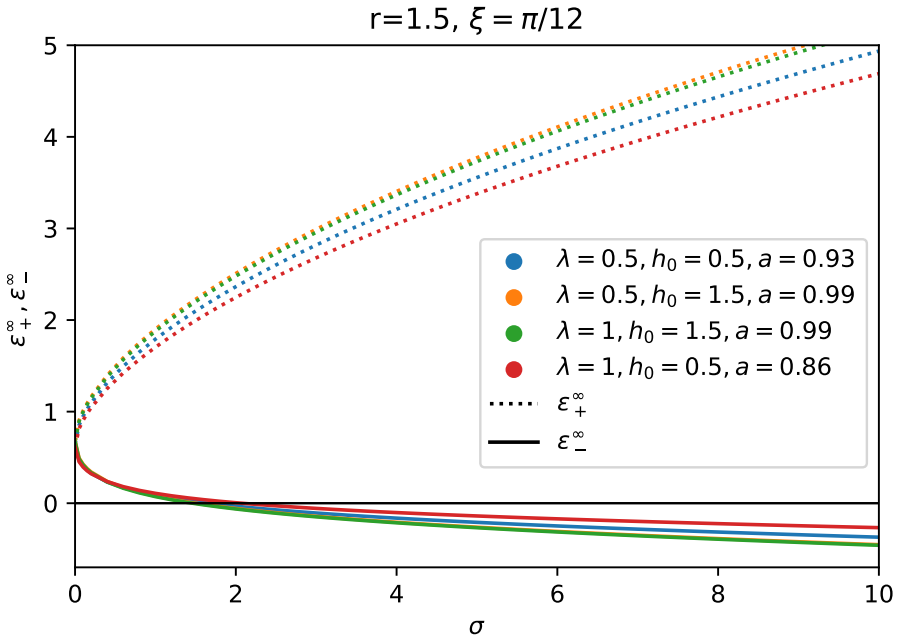

Figure 4.10: The behaviors of ϵ_+^∞ (dotted curve) and ϵ_-^∞ (solid curve) as a function of plasma magnetization $\sigma_0 \in [0, 10]$ with four different combinations of hairy parameter and black hole spin. The dominant reconnection radial location is taken as $r = 1.5$, with orientation angle $\xi = \pi/12$. The black solid line is $\epsilon_+^\infty = \epsilon_-^\infty = 0$ as reference

mated by [25]

$$P_{etr} = -\epsilon_-^\infty w_0 A_{in} U_{in} \tag{4.26}$$

where $U_{in} = \mathcal{O}(10^{-1})$ and $\mathcal{O}(10^{-2})$ respectively refer to the collisionless and collisional regimes. A_{in} is the cross-sectional area of the inflowing plasma, which can be estimated as $A_{in} \sim r_E^2 - r_{ph}^2$ for rapid rotating black holes, and r_E, r_{ph} are the outer ergosphere and light ring of the black hole, respectively.

We will investigate the power mainly in the collisionless regime which allows for a higher energy extraction rate than the collisional regime.

We first plot the ratio P_{etr}/w_0 as a function of the dominant reconnection radial location r in Fig.4.13, with different plasma magnetization $\sigma_0 = 10, 100, 1000, 10000$, by taking $a = 0.99$, $\xi = \pi/12$, $\lambda = 0.5$, $h_0 = 1.5$ and $U_{in} = 0.1$. The power extracted from the black hole rises monotonically as plasma magnetization rises. The power steadily declines after reaching a maximum at those locations close to the outermost circular orbit or light ring.

In order to examine the effects of the hairy parameters λ and h_0, we plot the ratio P_{etr}/w_0 as a function of the dominant reconnection radial location r in Fig.4.14, but with different combinations of hairy parameter, taking $\sigma = 100, \xi = \pi/12$ and $U_{in} = 0.1$. The results show that they all rise sharply when the location is closer to their light ring and then decline along with the increases in radial location r. The higher the peaks, the faster the decline. The critical locations r where $P_{etr}/w_0 = 0$ and the peaks where P_{etr}/w_0 reach the maximum also shift with the hairy parameters. The bigger the value of λ, the smaller critical locations and the

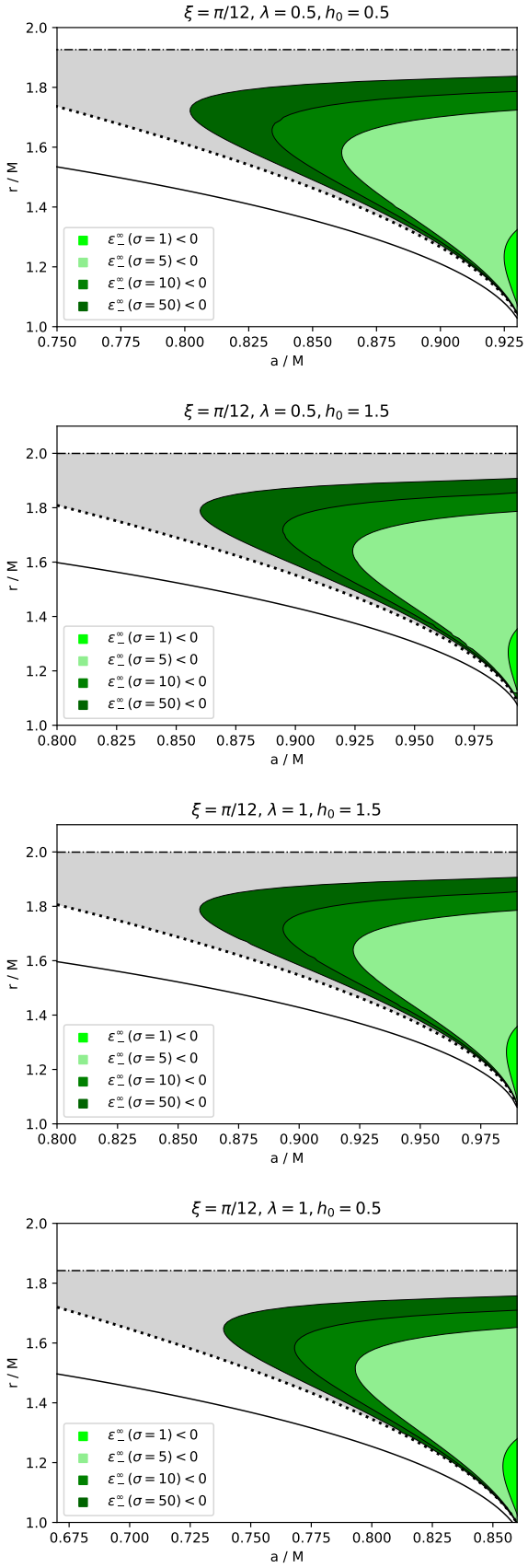

Figure 4.11: The parameter space $(r - a)$ with $\xi = \pi/12$ and four different different combinations of hairy parameter. The colored regions are $\epsilon^{\infty}_{-} < 0$ with $\sigma_0 = 1, 5, 10, 50$. The gray area is the region where $\epsilon^{\infty}_{+} > 0$. Black solid curves, black dotted curves, and black dot dashed curves are the radii of the outer event horizon, light ring, and outer ergosphere respectively.

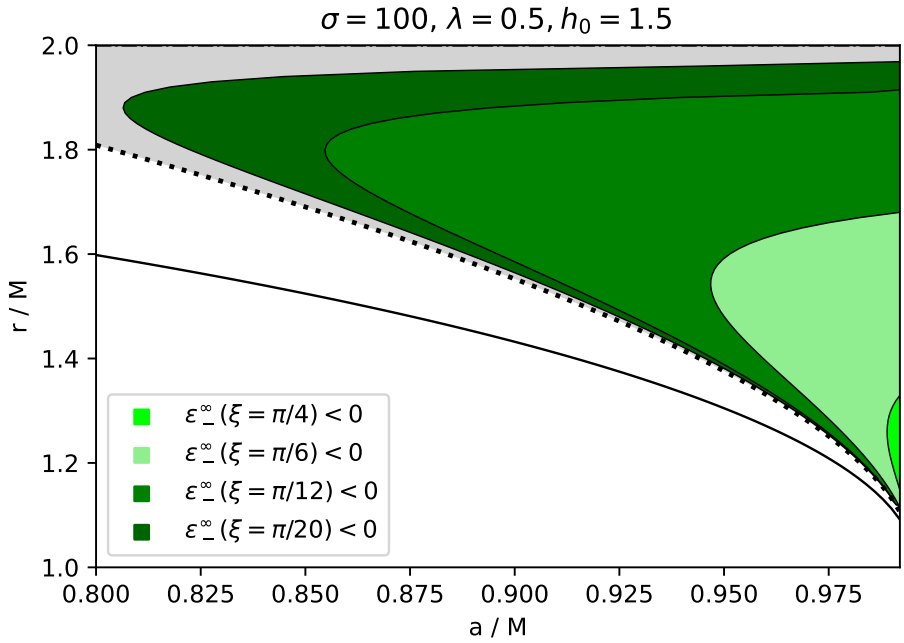

Figure 4.12: The parameter space $(r - a)$ with $\sigma_0 = 100$, $\lambda = 0.5$, $h_0 = 1.5$ and different orientation angle ξ. The colored regions are $\epsilon^{\infty}_{-} < 0$ with $\xi = \pi/20, \pi/12, \pi/6, \pi/4$ respectively. The gray area is the region where $\epsilon^{\infty}_{+} > 0$. Black solid curves, black dotted curves, and black dot dashed curves are the radii of the outer event horizon, light ring, and outer ergosphere respectively.

higher peaks when h_0 keep unchanged. The bigger the value of h_0, the bigger critical locations and the lower peaks when λ keep unchanged.

Next, we assess the efficiency. It is practical to define the efficiency as [25]

$$\eta = \frac{\epsilon^{\infty}_{+}}{\epsilon^{\infty}_{+} + \epsilon^{\infty}_{-}} \tag{4.27}$$

if $\eta > 1$, then the energy will be extracted from the rotating hairy black hole.

We plot the efficiency η as a function of the dominant reconnection radial location r in Fig.4.15 with different black hole spin $a = 0.90, 0.95, 0.98, 0.99, 1$, taking $\sigma = 100, \xi = \pi/12, \lambda = 0.5, h_0 = 1.5$. Note that the $a = 1$ case is the over-extreme black hole. With regard to the non-extreme situation, Fig.4.15 shows that the efficiency sharply increases with location r that is closer to the light ring and gradually declines after the peaks. As the black hole spin increases, the peaks shift to smaller locations and grow to higher values.

In addition, we plot the efficiency η in Fig.4.16 as a function of the dominant reconnection radial location r with different combinations of hairy parameter, taking $\sigma = 100, \xi = \pi/12$. There are peaks close to their light ring as well, and then all η decrease along with the radial location r, which seems that the decline rates are the same at sufficient large location ($r \approx 1.4$) regardless the hairy parameter combinations. However, the position and value of the peaks depend on the combinations of hairy parameter.

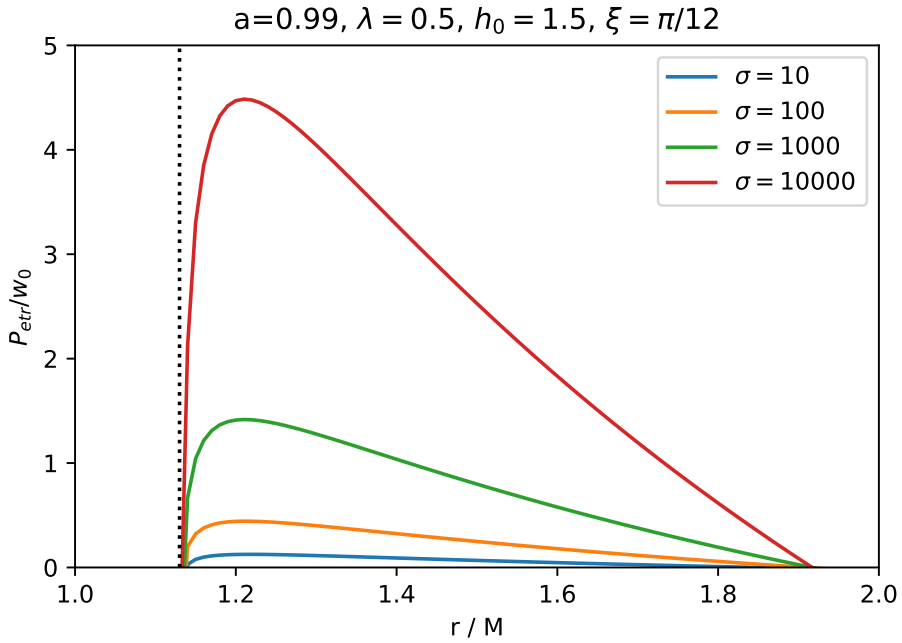

Figure 4.13: P_{etr}/w_0 as a function of the dominant reconnection radial location r with different plasma magnetization $\sigma_0 = 10, 100, 1000, 10000$, by taking $a = 0.99, \xi = \pi/12, \lambda = 0.5, h_0 = 1.5$ and $U_{in} = 0.1$. The vertical dotted line indicates the limiting circular orbit, i.e., light ring r_{ph}.

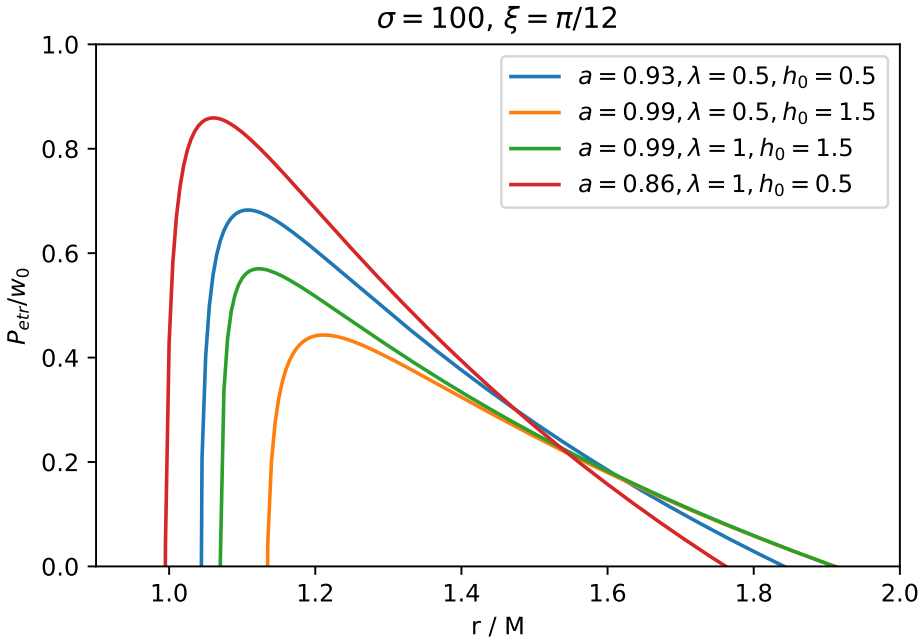

Figure 4.14: P_{etr}/w_0 as a function of the dominant reconnection radial location r with different combinations of the hairy parameter, by taking $\sigma = 100, \xi = \pi/12$ and $U_{in} = 0.1$.

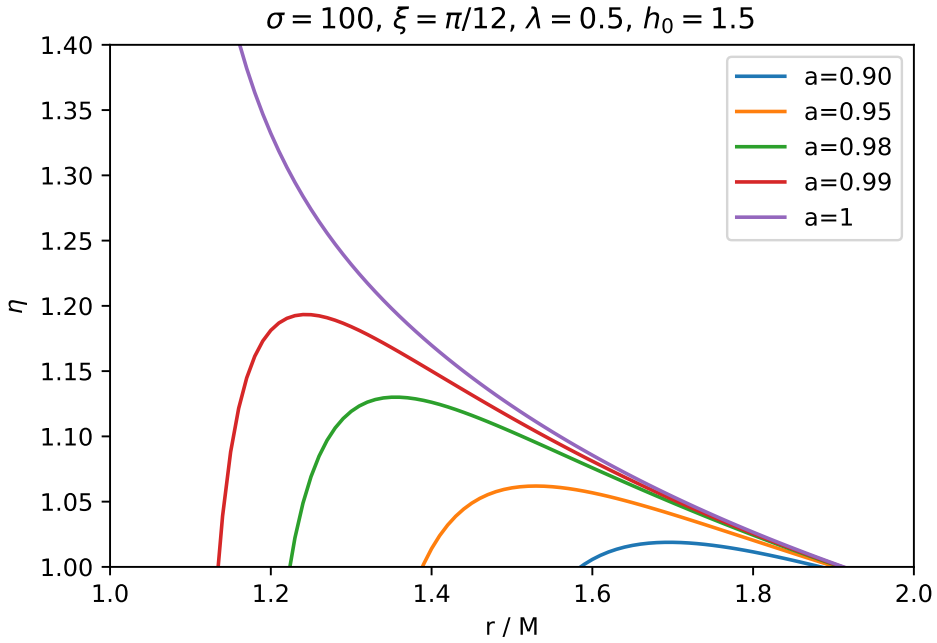

Figure 4.15: Efficiency η of the magnetic reconnection process as a function of the dominant reconnection radial location r with different black hole spin $a = 0.90, 0.95, 0.98, 0.99, 1$, taking $\sigma = 100, \xi = \pi/12, \lambda = 0.5, h_0 = 1.5$. Note that the $a = 1$ case is the extreme black hole.

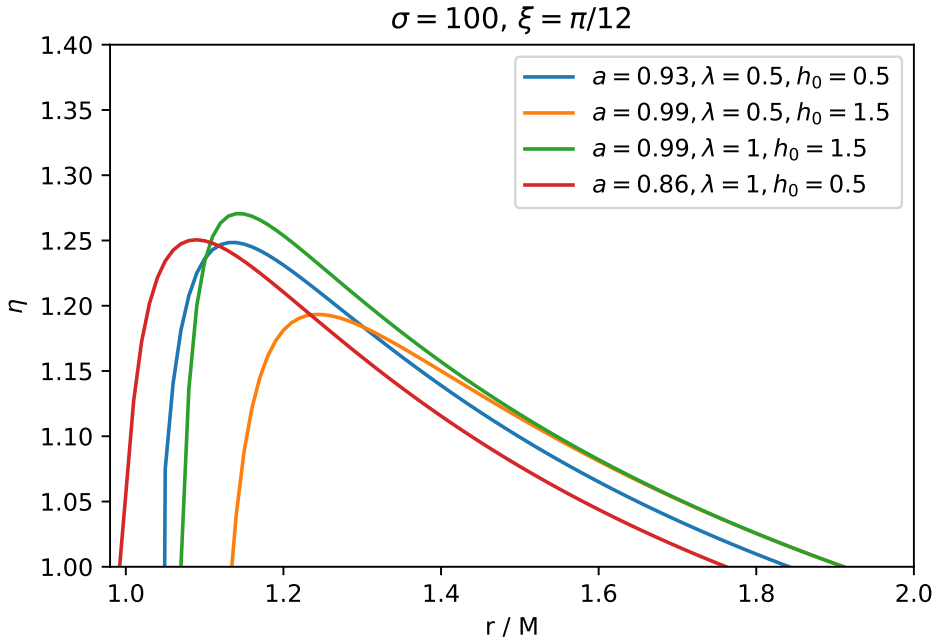

Figure 4.16: Efficiency η of the magnetic reconnection process as a function of the dominant reconnection radial location r with different combinations of hairy parameter, taking $\sigma = 100, \xi = \pi/12$.

Furthermore, we would like to make a power comparison between the energy extraction via Comisso-Asenjo mechanism and Blandford-Znajek mechanism. Regarding the Blandford-Znajek mechanism, it extracts the rotation energy of the black hole through a magnetic field that threads the event horizon. In the maximum efficiency conditions [178, 179, 180], the power of energy extraction is given by [165, 181, 182]

$$P_{BZ} = \frac{\kappa}{16\pi}\Phi_H^2(\Omega_H^2 + C_1\Omega_H^4 + C_2\Omega_H^6 + \mathcal{O}(\Omega_H^8)) \tag{4.28}$$

where κ is a numerical constant related to the magnetic field configuration. C_1 and C_2 are the numerical coefficients. The magnetic flux passing across the event horizon of the rotating hairy black hole is given by

$$\Phi_H = \frac{1}{2}\int_\theta\int_\phi |B_r|\sqrt{-g}d\theta d\phi = 2\pi(r_+^2 + a^2)B_0 sin(\xi)$$

. The angular velocity at the event horizon is

$$\Omega_H = 2ar_+(1 - \frac{1}{2}\lambda r_+ e^{-r_+/(1-h_0/2)})/\left(r_+^2 + a^2\right)^2$$

. Since the fundamental magnetic field configurations are the same as in the Kerr case, we expect that only the geometry quantities will be affected by the difference in the spacetime metric on the Blandford-Znajek mechanism. As a result, we just change the geometry quantities in the Blandford-Znajek power of Kerr black hole and obtain Eq.(4.28). Then, the power ratio between these two mechanisms is

$$\frac{P_{etr}}{P_{BZ}} \sim \frac{-4\epsilon_-^\infty A_{in}U_{in}}{\pi\kappa\sigma_0(r_+^2 + a^2)^2 sin^2(\xi)(\Omega_H^2 + C_1\Omega_H^4 + C_2\Omega_H^6)} \tag{4.29}$$

Taking the orientation angle $\xi = \pi/12$, the coefficients $\kappa = 0.05$, $C_1 = 1.38$ and $C_2 = -9.2$ [25], we show the power ratio P_{etr}/P_{BZ} as a function of the plasma magnetization σ_0 in Fig.4.17 with different dominant reconnection radial location $r = 1.3, 1.5, 1.7$. As the plasma magnetization gets closer to the critical value, we can observe that all of the power ratios rise along with it. Once their maximum values are reached, power ratios decrease along with the plasma magnetization. The distinct dependence on plasma magnetization is what causes the power ratios Eq.(4.29) to decline as plasma magnetization increases. Since we have $P_{etr}/P_{BZ} \sim 1/\sigma_0^{1/2}$ when $\sigma_0 \to \infty$, which drops as plasma magnetization increases. On the other hand, the Blandford-Znajek power has used the force-free electrodynamics approximation [165, 181, 182] which is invalid when $\sigma_0 \sim 1$. Therefore, in this instance, the power ratios can only be viewed as a rough comparison. We also notice that the smaller the location r, the faster the rising and decline of the curves. The different combinations of hairy parameter only slightly change the curves comparing to the location r. Nevertheless, the Comisso-Asenjo mechanism is a very promising and significant energy extraction mechanism from rotating hairy black holes since the power ratios are greater than 1 throughout a very wide parameter range.

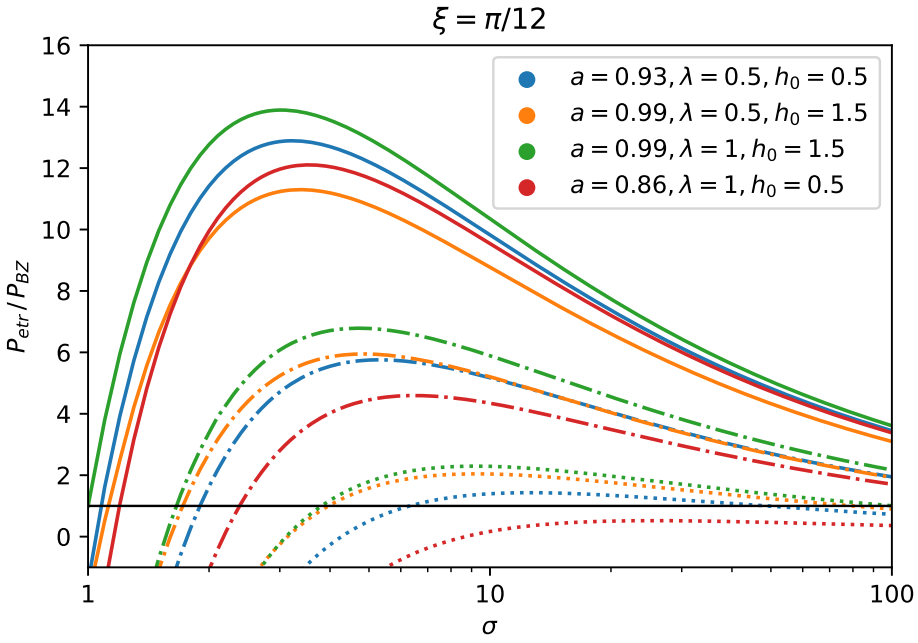

Figure 4.17: Power ratio P_{etr}/P_{BZ} as a function of the plasma magnetization σ_0 with different dominant reconnection radial location $r = 1.3$ (solid curve), 1.5 (dot-dashed curve), 1.7 (dotted curve), by taking the orientation angle $\xi = \pi/12$. The coefficients are taken as $\kappa = 0.05$, $C_1 = 1.38$, $C_2 = -9.2$ respectively. The black solid line is $P_{etr}/P_{BZ} = 1$ as reference.

4.2.6 Conclusion

The rotating hairy black hole is a very encouraging black hole solution beyond classical general relativity. The existence of new hair originated from unknown fundamental field, such as dark matter and dark energy, will break down the No Hair theorem of general relativity and lead to a new theory for gravity as well as spacetime. Therefore, the phenomenological investigation of rotating hairy black hole spacetime is crucial for testing this hypothesis and laid foundation for observations. In this paper, we studied the energy extraction from a rotating hairy black hole (4.23) via magnetic reconnection process in the ergosphere.

We started by presenting Comisso-Asenjo formulas, i.e., the plasma energy at infinity density (4.17) associated with the accelerated and decelerated parts as well as the conditions (4.18) allowing the energy extraction to occur. Then, all the following analyses are based on these.

We first emphasize our discussion on how the plasma magnetization and hairy parameter will affect the behavior of the plasma energy-at-infinity density per enthalpy ϵ_+^∞ and ϵ_-^∞, taking the orientation angle $\xi = \pi/12$ and dominant reconnection radial location $r = 1.5$. The results show that ϵ_+^∞ increases monotonically along with plasma magnetization while ϵ_-^∞ decreases with it. In addition, we found that in order to make the effects of the hairy parameter λ become significant, the other hairy parameter h_0 should be sufficiently small. The amount of energy extraction has a positive correlation with the maximal black hole spin which the hairy param-

eter combinations correspond to. Then, we studied how the black hole spin affects the energy extraction by demonstrating the two-dimensional $(r-a)$ parameter space with different combinations of hairy parameter, taking orientation angle $\xi = \pi/12$. We found that the smaller the black hole spin the relatively larger radial location r such that the energy extraction works.

We also investigated how the power and efficiency of the energy extraction through magnetic reconnection will be impacted by the hairy parameters as well as the other critical parameters. They all have peaks near their light ring and decrease with radial location after reaching the peaks. However, the location and value of the peaks depend on the combinations of hairy parameter. At the end, we compared the power ratio between the Comisso-Asenjo mechanism and the Blandford-Znajek mechanism. It turns out that the energy extraction via the Comisso-Asenjo mechanism is more effective in a sufficiently wide parameter range. Especially, the closer the radial location to the event horizon, the greater the power ratio. The effects of different combinations of hairy parameter on the power ratios are small comparing to that of the dominant reconnection radial location.

Since we have made the same assumption as in the original work of Comisso and Asenjo [25] that the plasma rotates in circular orbits, one possibility for future research is to consider more complex and realistic cases where reconnection takes place in noncircular orbits. The allowable parameter space for extracting energy from rotating hairy black holes should be expanded, since the plasma could get closer to the event horizon even if the black hole spin is not very high. Moreover, if the force-free approximation of Eq.(4.28) fails, one should also consider the energy and angular momentum carried by the accretion plasmas onto the black hole, which would be more accurate for the comparison (4.29) if $\sigma_0 \sim 1$. In addition, the Comisso-Asenjo formalism is very general and can be applied to many different spacetime. It offers us a brand new way to extract energy from rotating black holes. So one could extend the Comisso-Asenjo mechanism to other rotating black holes and even to wormholes.

Chapter 5

A phenomenological model for dark matter distribution

This chapter is based on the following first-author paper:

- **A phenomenological model for dark matter phase-space distribution**
  Authors: **Zhen Li**, Steen H. Hansen
  Published in MNRAS 529, 1877 (2024). arxiv: 2312.12304.
  Author contributions:
  Zhen Li proposed the idea and performed all the calculations, figure plotting, code and draft writing, as well as the manuscript revision. Steen H. Hansen provided comprehensive feedback throughout the writing and analysis process. Steen H. Hansen also provided the simulated velocity data and proofread the manuscript.

Abstract: Understanding the nature of dark matter is among the top priorities of modern physics. However, due to its inertness, detecting and studying it directly in terrestrial experiments is extremely challenging. Numerical N-body simulations currently represent the best approach for studying the particle properties and phase space distribution, assuming the collisionless nature of dark matter. These simulations also address the lack of a satisfactory theory for predicting the universal properties of dark matter halos, including the density profile and velocity distribution. In this work, we propose a new phenomenological model for the dark matter phase space distribution. This model aims to provide an NFW-like density profile, velocity magnitude distribution, and velocity component distributions that align closely with simulation data. Our model is relevant both for theoretical modeling of dark matter distributions, as well as for underground detector experiments that rely on the dark matter velocity distribution for experimental analysis.

5.1 Introduction

Dark matter is an invisible and mysterious substance that makes up a great portion of the universe. While its existence is solely inferred from its gravitational effects, its true nature and composition remain one of the most significant questions in modern astrophysics and particle physics. Detecting dark matter has proven to be incredibly challenging because it does not emit or interact with light. Based on these limitations, cosmological N-body simulations may, at the moment, be the only

possibly way to study dark matter structures and distributions. These simulations are performed assuming the collisionless property of dark matter, see the review of simulations [186, 187].

Across a wide range of halo mass and redshift, some universal properties appear in different dark matter simulations when the halos attain equilibrium [34, 35, 36, 37, 38, 39, 40]. The density profile of dark matter halos can always be fitted quite well by the famous double power law density profile, i.e, the Navarro-Frenk-White (NFW) model [188, 189, 190], which has logarithmic density slope -1 close to the center and -3 in the outer region. Although there are alternative models (see a brief review [191]), NFW model plays a crucial role in modern dark matter related researches. It finds applications in simulating galaxy formation [186], gravitational lensing modeling [192, 193], galaxy rotation curves [194], dark matter detection experiments [195], and so on. In addition, the velocity anisotropy has also been shown to vary as a function of radius [35, 36, 37]. Another important universal feature in simulations is the so called phase-space density ρ/σ^3, which seems to follow a power-law with respect to radius [38, 39]. These universal empirical properties unveil the intrinsic physics of collisionless N-body systems as well as properties of equilibrium dark matter structures in a cosmological setting. However, there is still no universally accepted theoretical model that predicts all of these empirical results [41, 42, 43, 44, 45, 46, 47, 48].

Another important aspect is the velocity distributions of dark matter particles. The direct detection experiments of dark matter, which aim to detect the low energy nuclear recoil from rare scattering events between target nuclei and dark matter particles, relies on the knowledge of velocity distributions near the location of solar system. Therefore, it is essential to know the velocity distributions of dark matter halos. The inverse-Eddington method is very efficient to perform this task [196], however, it is only valid under certain limiting circumstances [197]. There are also degeneracies in the velocity distributions for a given density profile when the system is not ergodic, because single variable function $\rho(r)$ is not sufficient to determine the velocity distribution which involves multiple variables. An ideal velocity distribution function should also provide the distribution of velocity components. As an example, the standard halo model (SHM) is known to not provide the right description on the velocity distributions [45, 46, 47, 48], especially the behavior of high velocity tails. Therefore, many velocity distribution models have been proposed, either from the first principle or theories [198, 199, 200, 201], guessing from the empirical fitting [202, 203, 204, 205, 206], inferring from the observational data [207, 208, 209], or parameterizing velocity distributions [210, 211, 212]. However, none of these are fully satisfactory and widely accepted. Furthermore, these velocity distribution models also have degeneracy in the velocity components since they all use the velocity magnitude rather than the velocity components as principle variables.

Instead of working on the universal properties (like density profile) and velocity distribution separately, we suggest applying an unified approach where the density profile (as well as other universal properties) and velocity distributions could be derived and are consistent with each other. One promising way is to propose a phase space distribution function from which the density profile and velocity distributions could easily be derived and thus automatically be consistent with each

other. The density could be obtained through the velocity integral of the phase space distribution function, and the velocity distribution could also be derived by fixing the radius and potential in the phase space distribution function [213].

In previous studies, one notable phase space distribution model has been proposed by assuming the separability of energy and angular momentum in the distribution function [214]. This model could successfully recover many empirical laws observed in simulations. It has three parameters for the angular momentum part (or anisotropy profile), and the energy part is obtained by inverting the density profile, which usually doesn't have analytical expressions. A six parameter analytical approximation for the energy part was given. Due to the large number of parameters (at least nine parameters) in this model, it introduces many uncertainties in predicting the properties of distribution, potentially causing overfitting to the simulation data.

More generally speaking, not restricting to a phase space distribution, it could also be some kind of formula that is related to phase space distribution. By working in energy or orbit space, the well-known DARKexp model has been developed, which is derived from the first principle of statistical mechanics for self-gravitating collisionless systems [215, 216]. DARKexp model only has one free parameter, i.e., the central potential, and could provide a good fit to the energy distributions. The corresponding phase space distribution could be obtained by dividing the DARKexp energy distribution with the density of states. However, DARKexp focuses on the isotropic scenario. Currently, there is no relevant research available for the anisotropic case, which needs further development.

There is also an action-based approach that could related to phase space distribution, which were derived using the action-angel method [217, 218, 219]. However, the reasoning employed to create the distribution function does not apply to the NFW case. Consequently, there is no action distribution function for NFW density profile, instead they proposed an empirical model for NFW [217]. In addition, the action-based models generally do not provide analytical formula for the derived quantities, making their application more challenging.

In this work, we aim to propose a new analytical and ready-to-use phase space distribution with few free parameters, which could result in a NFW-like density profile, the radial varied anisotropy as well as power law phase-space density (although certain disagreements with simulation data exist). What's more, it can also provide us with the velocity magnitude distribution as well as its components, with natural cut off at the local escape velocity. We will also compare our analytical velocity distributions with simulation data, which has radial and tangential velocity data separately allowing to break the degeneracy of the velocity magnitude distributions. Our model fit quite well to the radial velocity data and also the low velocity regime of tangential velocity data, giving consistent results on the distributions as well as the fitting parameters within an acceptable range. This provides support that our analytical model may be relevant for understanding the gravitational dynamics of cosmological dark matter structures.

This chapter is organized as follows: In section.5.2, we will present our dark matter phase space distribution function and study its predictions on the density profile, anisotropy parameter, as well as the phase space density. Additionally, we will provide the formulas for the velocity magnitude , the radial and tangential

velocity components distributions. Next, in section.5.3, we will compare our radial and tangential velocity distributions with simulation data. The velocity data were extracted from different radial bins (shell) of equilibrium dark matter halos, with both radial and tangential velocity data available in each bin. For comparison, we use data from two different simulation schemes, namely the cold collapse and explicit energy exchange. The fitting results and estimated parameters are also presented in this section. Finally, we will conclude and discuss our findings in section.5.4.

5.2 The distribution function and its properties

Based on the observations of the simulation data introduced in subsection.5.3, a reasonable distribution function should be spherically symmetric due to the simulated halos have no preferred spatial directions. Therefore, it is convenient to write out the distribution function of dark matter halos in spherical coordinates (r, θ, φ). The distribution function should also be anisotropic because the simulation data of radial and tangential velocity distributions are different. That means we need take into account the angular momentum of dark matter particles. It would be a good choice to put the angular momentum in the exponent because when we integrate the distribution function to obtain the density profile, it will result in a term of $1+r^2$ in the denominator. Then if we wish to obtain an NFW-like profile, we could just multiply it by the radial distance r. Meanwhile, we would like the distribution function to have a natural cutoff, and it could be realized by multiplying the binding energy. After considering the above conditions, our distribution function is given by

$$f(v_r, v_t, r) = f(\epsilon, L, r) \propto \frac{r_0}{r} \times \frac{\epsilon}{\lambda^2} \times \mathrm{Exp}\left(Q/\lambda^2\right) \tag{5.1}$$

where r_0 is the parameter to normalize radial distance, and λ is the parameter to normalize the binding energy ϵ and exponent Q which are given by

$$\epsilon = -\frac{v^2}{2} + \phi \tag{5.2}$$

$$v^2 = v_r^2 + v_t^2 \tag{5.3}$$

$$Q = \epsilon - L^2/4r_0^2 \tag{5.4}$$

$$L = rv_t \tag{5.5}$$

where ϕ is the positive potential, v_r and $v_t = \sqrt{v_\theta^2 + v_\varphi^2}$ are respectively the radial and tangent velocity, and L is the angular momentum of dark matter particles. One could notice that this distribution function does not satisfy the Jeans theorem since there is a factor r_0/r, which means that the full form is not only a function of the integrals of motion. This could be seen as the limitation of our model. However, this limitation does not undermine the primary objective of our work. We have proposed a phenomenological or effective model rather than presenting a comprehensive theory. Therefore, it is acceptable for breaching the Jeans theorem as long as it is consistent with the simulation data.

For simplicity, in the following discussion of this section, we will denote $a = r/r_0$ and set $\lambda = 1$. Then the potential, binding energy and Q are all in unit of λ^2, the

velocity is in unit of λ. The density of the above distribution is given by the integral with respect to velocities

$$\begin{aligned}\rho(a,\phi) &= 2\pi \int v_t f(v_r, v_t, a) dv_r dv_t \\ &= N_\rho [\frac{\sqrt{2\pi} e^{\phi} \left(a^2(2\phi-1)+4\phi-6\right) \mathrm{erf}\left(\sqrt{\phi}\right)}{a\left(a^2+2\right)^2} \\ &\quad + \frac{8\sqrt{\pi} e^{-\frac{1}{2}\left(a^2\phi\right)} \mathrm{erfi}\left(\frac{a\sqrt{\phi}}{\sqrt{2}}\right)/a}{a\left(a^2+2\right)^2} + \frac{2\sqrt{2\phi}}{a\left(a^2+2\right)}]\end{aligned} \tag{5.6}$$

where N_ρ is the normalization constant, which is usually the inverse of the halo mass, $erf(x)$ and $erfi(x)$ are called error function and imaginary error function. To obtain $\rho(a)$, we first need to know the dependence of ϕ on a, which requires solving the spherically symmetric Poisson equation,

$$\frac{d}{da}(a^2 \frac{d\phi}{da}) = -4\pi G a^2 \rho(a,\phi) \tag{5.7}$$

however, it has to be solved numerically. Starting from $a = 0$ for some chosen value of $\phi(0)$ and $\frac{d\phi}{da} = 0$, we thus can solve for $\phi(a)$. In practice, we need to apply a softening to the centre point $a = 0$ due to the divergent behavior of $1/a$ of the Poisson equation. If we assume that the central potential is nearly flat within a small radial distance, let's say $a = 0.01$. Then, we could solve the Poisson equation by choosing that the initial conditions at $a = 0.01$ is the same as the centre point. Thus, the numerical results are not sensitive to the choice of $a = 0.01$ as long as the approximation of flat central potential is valid. In the following discussions, we mainly choose to start the numerical solution from $a = 0.01$ with different initial potentials, i.e., $\phi(0.01) = 5$, 7, 10 and $\frac{d\phi}{da}|_{a=0.01} = 0$. As a comparison, we also show the numerical results of potential when we choose to start with $a = 0.001$. The gravitational constant G in the numerical solutions is set to be $4.301 \times 10^{-6} kpc M_\odot^{-1} (km/s)^2$, and the normalization factor N_ρ is set to $N_\rho = 1$.

5.2.1 potential, density, anisotropy and pseudo phase pace density

The numerical results of the potential are shown in Fig.5.1 and Fig.5.2 for given initial potentials. We can see that all the potentials with different initial conditions are quite smooth when close to the center and at a significant distance from the center, with a drastic transition between them. A larger initial potential, a greater difference between the central and distant regions, and a faster drop in the transition region. By comparing the potentials in Fig.5.1 and Fig.5.2, we can see that results are not sensitive to the initial value a in the numerical solutions. The potentials are almost the same regardless of the different initial values of a. Therefore, we could safely use one of the numerical results of potential (the case with $a = 0.01$) to continue our discussion.

With the results of potential, we can obtain the density (5.6) corresponding to the distribution function (5.1). The results are shown in Fig.5.3. For comparison,

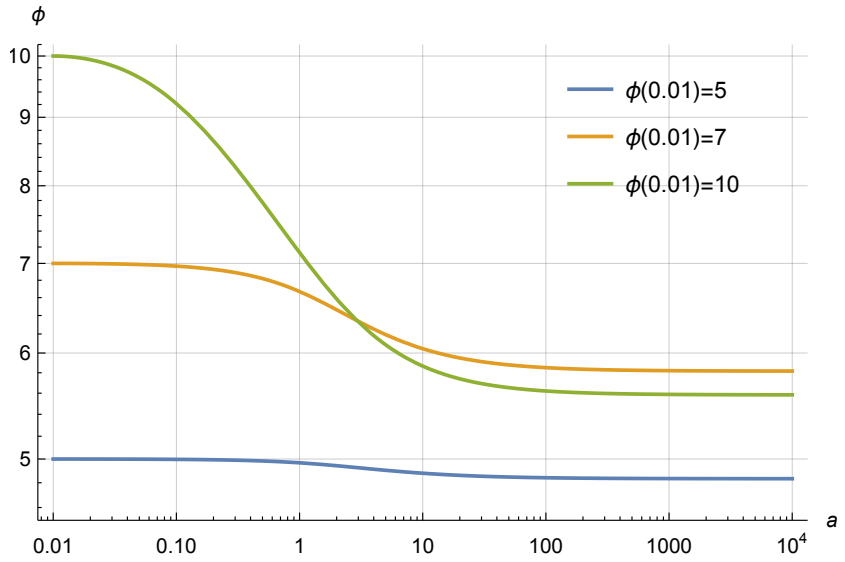

Figure 5.1: The numerical solution of the potentials as a function of radial distance a, for three different initial conditions $\phi(0.01) = 5, 7, 10$ and $\frac{d\phi}{da}|_{a=0.01} = 0$ at $a = 0.01$.

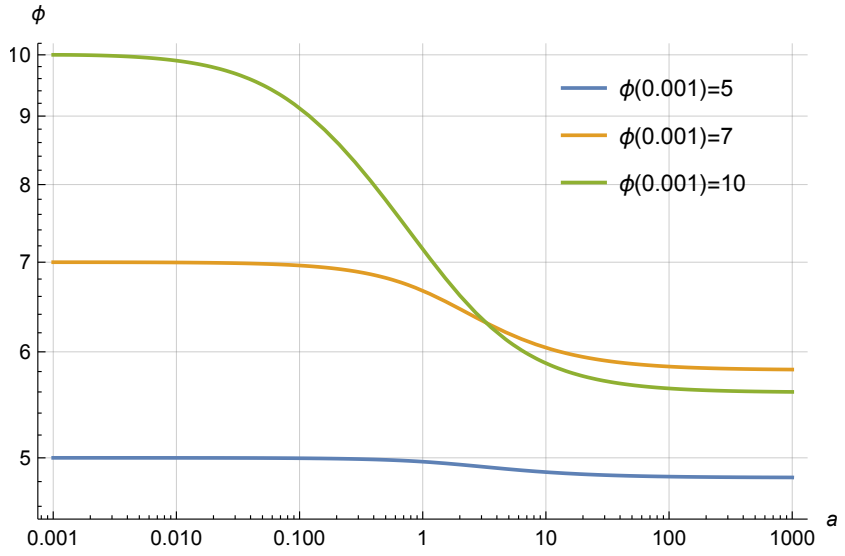

Figure 5.2: The numerical solution of the potentials as a function of radial distance a, for three different initial conditions $\phi(0.001) = 5, 7, 10$ and $\frac{d\phi}{da}|_{a=0.001} = 0$ at $a = 0.001$.

we also plot the NFW density profile

$$\rho_{NFW} \propto \frac{1}{r(r+r_s)^2} \tag{5.8}$$

by setting the characteristic radius of NFW as $r_s = \sqrt{2}r_0$. All the density profiles are normalized by demanding that they have the same total mass $M_{tot} = 1$ within their R_{200} radius where the average density within this radius are 200 times than the mean density of the universe which is set to be 5×10^{-5} for simplicity. We can see that they are very similar to the well-known NFW density profile, which has logarithmic density slope $\gamma = dlog\rho/dloga$ approximately -1 near the center and -3 in the outer region of the halo, referring to Fig.5.4 for the variation of γ with radial distances. However, there are also differences between NFW and our model, especially in the transition region where γ is from -1 to -3. Our model seems more sharper than the NFW density profile around the transition region. The initial potentials will affect the logarithmic slope near the center region. The concentrations $c \equiv R_{200}/R_{-2}$ (R_{-2} is the radius at which the logarithmic slope is -2) for the curves in Fig.5.3 with $\phi(0.01) = 5, 7, 10$ and NFW are respectively 222.7, 645.5, 14866.7 and 231.9. It is evident that larger initial potential values result in higher concentrations. To closely resemble the NFW profile, the initial potential should be sufficiently small. The smaller the initial potential, the more similar the profile to the NFW one. It is remarkable that we can obtain the NFW-like density profile from a phase space distribution function.

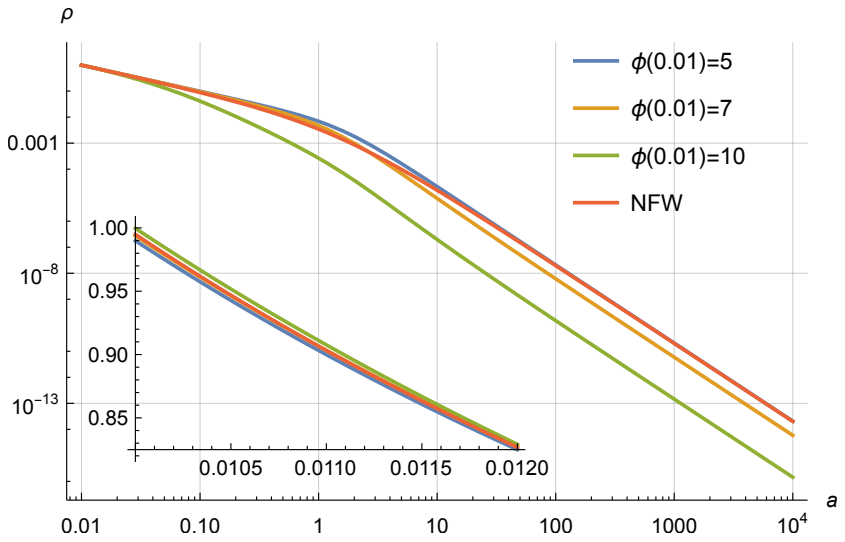

Figure 5.3: The numerical result of dark matter density as a function of radial distance a, for three different initial conditions $\phi(0.01) = 5, 7, 10$, and the NFW density profile by setting $r_s = \sqrt{2}\,r_0$. All profiles are normalized by ensuring that they share the same total mass within their R_{200} radius as $M_{tot} = 1$. The concentrations for the curves with $\phi(0.01) = 5, 7, 10$ and NFW are 222.7, 645.5, 14866.7 and 231.9 respectively.

Since our model considers the anisotropic case, it is also important to investigate

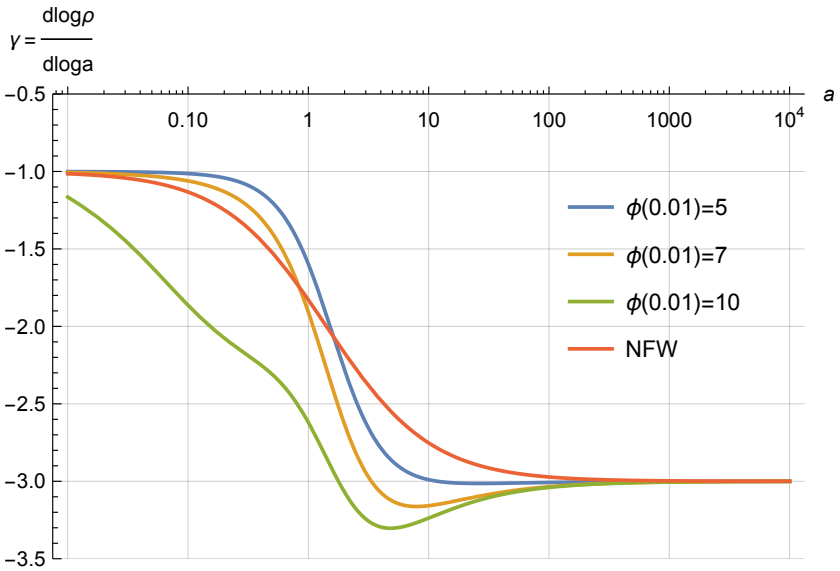

Figure 5.4: The logarithmic slope of the dark matter density γ as a function of radial distance a, with three different initial conditions $\phi(0.01) = 5$, 7, 10, and the NFW density slope by setting $r_s = \sqrt{2}\, r_0$.

the anisotropy parameter β which is defined as

$$\beta(a) \equiv 1 - \frac{\sigma_t^2}{2\sigma_r^2} \tag{5.9}$$

where σ_t and σ_r are respectively the tangential and radial velocity dispersion. They could be compute through

$$\sigma_r^2(a) = \frac{2\pi}{\rho(a)} \int v_r^2 * v_t f(v_r, v_t, a) dv_r dv_t \tag{5.10}$$

$$\sigma_t^2(a) = \frac{2\pi}{\rho(a)} \int v_t^3 f(v_r, v_t, a) dv_r dv_t \tag{5.11}$$

We show β as a function of a in Fig.5.5. Despite the different initial potentials, we observe that the values of β are nearly identical. The initial conditions do not affect the anisotropy. β starts at $\beta = 0$, i.e., $\sigma_t^2/2 = \sigma_\theta^2 = \sigma_\varphi^2 = \sigma_r^2$, indicating isotropy around the center. As the radius grows, β increase rapidly around the scale radius $a \approx \sqrt{2}$, reaching $\beta = 1$ at larger radial distances. This implies $\sigma_t^2 \ll \sigma_r^2$. This type of β behaves similarly to the commonly-used Osipkov-Merritt model [220, 221], which is expressed as

$$\beta(r) = \frac{1}{1 + r_a^2/r^2} \tag{5.12}$$

with r_a as the scale parameter in Osipkov-Merritt model. We also illustrate the behavior of $\beta(r)$ when $r_a^2 = 2\sqrt{2}\, r_0^2$ in Fig.5.5. We can see that they are almost the same to our model across a large range of radial distances. This could be attributed to the exponent of our distribution function Q which is similar to the Osipkov-Merritt model. $\beta(r)$ is only related to the scale parameter r_a and independent of the other parameters of the Osipkov-Merritt model. A similar observation holds

for our model, possibly explaining why all the $\beta(a)$ values in our model are almost identical. Eq.(5.12) could serve as an approximation for $\beta(a)$ in our model, achieved by setting $r_a^2 = 2\sqrt{2}\, r_0^2$.

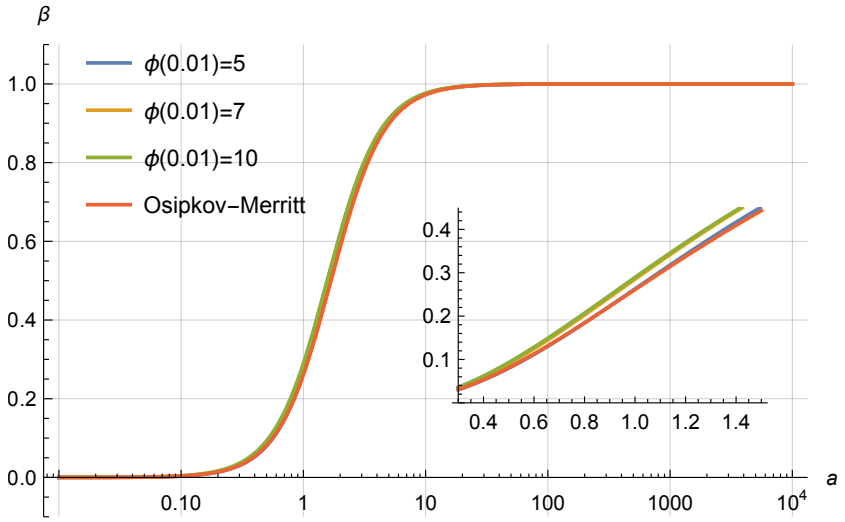

Figure 5.5: The anisotropy parameter β as a function of radial distance a, with three different initial conditions $\phi(0.01) = 5,\ 7,\ 10$, as well as the $\beta(r)$ of the Osipkov-Merritt model with $r_a^2 = 2\sqrt{2}\, r_0^2$.

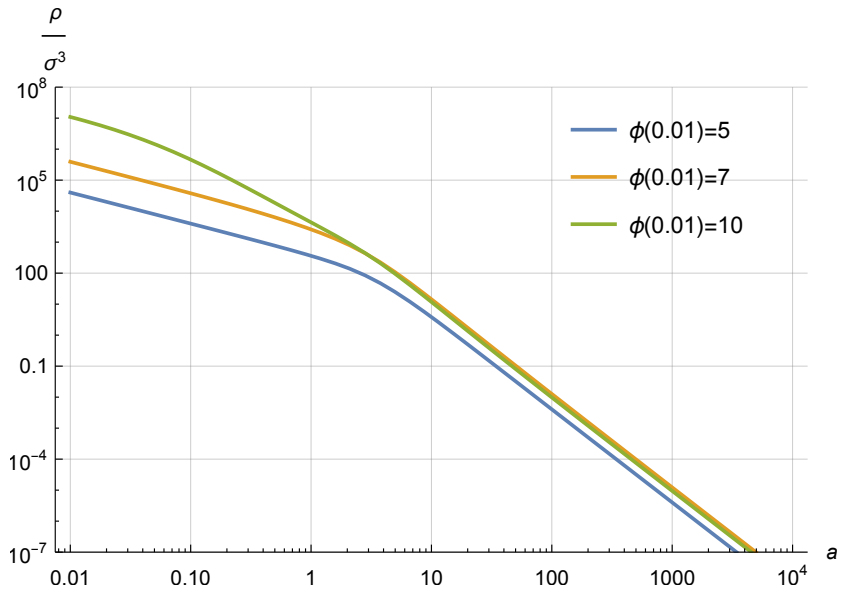

Figure 5.6: The pseudo phase space density as a function of radial distance a, with three different initial conditions $\phi(0.01) = 5,\ 7,\ 10$.

We also investigate the pseudo phase space density

$$\frac{\rho}{\sigma^3} = \frac{\rho}{(\sigma_t^2 + \sigma_r^2)^{3/2}} \tag{5.13}$$

which is another important empirical laws. In Fig.5.6, we plot the pseudo phase space density as a function of a. We can see that it has a pretty much the same

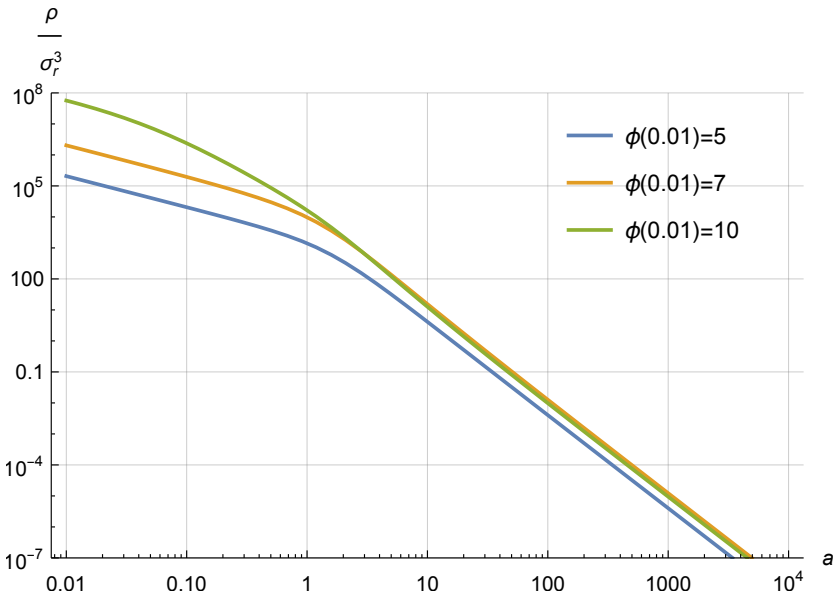

Figure 5.7: The quantity ρ/σ_r^3 as a function of radial distance a, with three different initial conditions $\phi(0.01) = 5,\ 7,\ 10$.

logarithmic density slope as the density, see Fig.5.3. It has logarithmic slope of -1 in the inner region and -3 in the outer region. These results disagree with simulation data, which show a simple logarithmic slope ≈ -1.9 across a large range of orders of magnitude in radius a [38, 39, 222, 223, 224]. Nevertheless, the different initial potentials only cause a difference in the center region and have no effect on the outer region. For comparison, we also plot the quantity ρ/σ_r^3 as a function of radius [222] in Fig.5.7. The slopes in the outer region are the same as the pseudo phase space density, while there is an overall shift to higher values in the center region. Unfortunately, these still contradict the simulation data [39, 222].

5.2.2 velocity distributions

The velocity magnitude distribution $f(v)$ could be obtained by transformation and integrating over the distribution function (5.1). We get

$$f(v) = N_v \frac{4\pi e^{\phi - \frac{v^2}{2}} \left(2\phi - v^2\right) \text{DawsonF}\left(\frac{1}{2}\sqrt{a^2 v^2}\right)}{a\sqrt{a^2 v^2}} \tag{5.14}$$

where N_v is the normalization constant, DawsonF(x) is the so-called Dawson integral. We have plotted the velocity magnitude distribution for different radii $a = 1,\ 5,\ 10$ in Fig.5.8, by choosing the initial potential $\phi(0.01) = 5$. As comparison, we also show the SHM velocity distributions which corresponds to the Maxwell-Boltzmann phase space distribution. We can see that our velocity distribution is suppressed more than the SHM model in the high velocity tails. The velocity distributions are more concentrated at lower values as the radial distance becomes larger. We also compare the velocity distribution function (5.14) with simulation data from the Aquarius Project [225, 45]. We fitted the data with our model as well as the SHM model in Fig.5.9. The velocity distribution data are taken from

many 2 kpc boxes located between 7 and 9 kpc from the center of halo Aq-A-1 in Aquarius Project. In each 2 kpc box, there are about 10^4 to 10^5 particles. In Fig.5.9, the black line is the median value of velocity distribution measured over all 2 kpc boxes, and the green band encloses 95% of the measured velocity distributions for each velocity bin, and each velocity bin has a width of 5 km/s. We can see that our model almost overlaps the SHM model, with the exception that our model exhibits a relatively larger suppression in the high velocity tails, resulting in a better fit to the simulation data.

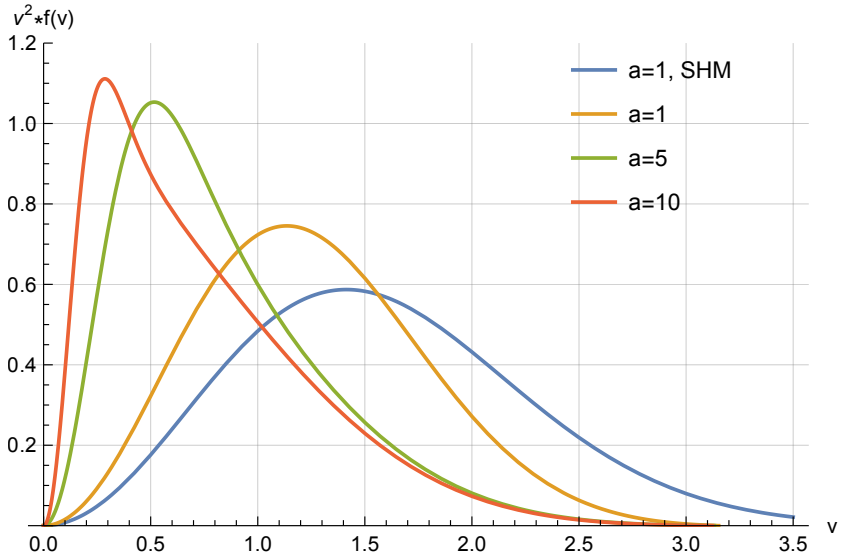

Figure 5.8: The normalized velocity magnitude distribution $v^2 f(v)$ as a function of velocity v, at three different radial locations $a = 1$, 5, 10, with initial potential $\phi(0.01) = 5$. We also show the Maxwell-Boltzmann distribution which is also known as the standard halo mode (denote as SHM) at $a = 1$, as comparison.

The above velocity magnitude has some extent degeneracy over the velocity components. Therefore, it is crucial to understand the radial and tangential velocity distributions and validate them through simulations.

By integrating over the tangent velocity component in the distribution function (5.1), this yields the radial velocity distribution. Similarly, we can integrate over the radial velocity component in the distribution (5.1) to obtain the tangential velocity distribution. They are respectively given by

$$f(v_r) = N_r[\frac{e^{-\frac{v_r^2-2\phi}{2\lambda^2}}\left(4\lambda^2\left(e^{\frac{\left(a^2+2\right)\left(v_r^2-2\phi\right)}{4\lambda^2}}-1\right)\right)}{a\left(a^2+2\right)^2} + \frac{e^{-\frac{v_r^2-2\phi}{2\lambda^2}}\left(-v_r^2\left(a^2+2\right)+2\phi\left(a^2+2\right)\right)}{a\left(a^2+2\right)^2}] \tag{5.15}$$

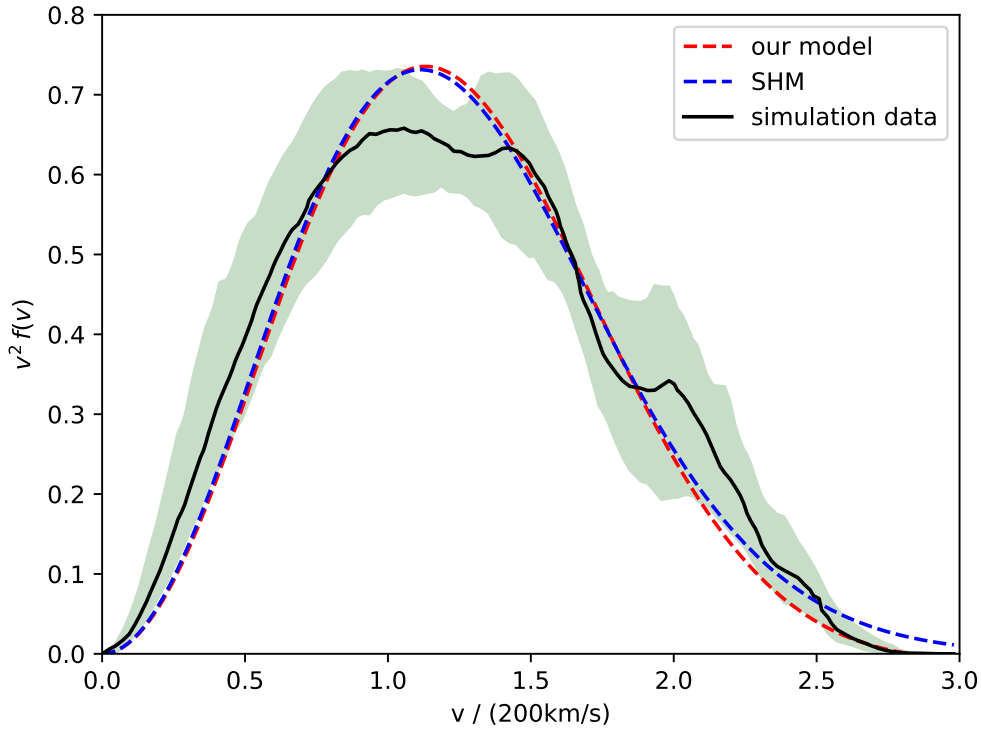

Figure 5.9: The best fit of our model(red dashed) and SHM model(blue dashed) to the velocity distribution data extracted from 2 *kpc* boxes between 7 and 9 *kpc* from the center of halo Aq-A-1 in Aquarius Project. The black line is the median value while the green band enclose 95% of the velocity distributions over all 2 *kpc* boxes.

$$f(v_t) = N_t[-\frac{e^{-\frac{\left(a^2+2\right)v_t^2}{4\lambda^2}}\left(\sqrt{2\pi}e^{\frac{\phi}{\lambda^2}}\left(\lambda^2+v_t^2-2\phi\right)\operatorname{erf}\left(\frac{\sqrt{\phi-\frac{v_t^2}{2}}}{\lambda}\right)\right)}{2a\lambda} + \frac{e^{-\frac{\left(a^2+2\right)v_t^2}{4\lambda^2}}\left(2\lambda e^{\frac{v_t^2}{2\lambda^2}}\sqrt{2\phi-v_t^2}\right)}{2a\lambda}] \tag{5.16}$$

where N_r and N_t represent the normalization constants. To fit the real simulation data in the next section, we have kept λ as a free parameter rather than $\lambda = 1$ in the above formulas of $f(v_r)$ and $f(v_t)$. It can be verified that the radial and tangential velocity distribution functions approach zero at the local escape velocity $v_r = v_t = v_{escape} = \sqrt{2\phi}$, indicating a cutoff at the local escape velocity.

5.3 Comparing velocity component distribution with simulation data

5.3.1 the simulation data

We use the velocity data extracted from the simulation in [226]. These numerical simulations were described in detail previously [199, 200]. To test our model, we compare the velocity distribution function with two different scheme of simulation performed in [226].

The first is called the cold collapse simulation. This aims to simulate the violent relaxing process that occurs in the early universe when structure collapsed. They create a main halo with a number of compact and condensed substructures. All particles started with zero velocities and evolve under gravity. Once it has attained equilibrium, we divide a halo structure into radial bins (thin spherical shell) and thus we can extract the radial and tangential velocity components of the particles from selected bins. We sample the same number of particles in three radial bins whose radial and the tangential velocity data are shown in Fig.5.10. To facilitate the readability of the bin data, some of the bin data have been shifted vertically. The three radial bins were chosen near the slope of $\gamma_0 = dlog\rho/dlogr = -1.6, -2.0, -2.4$.

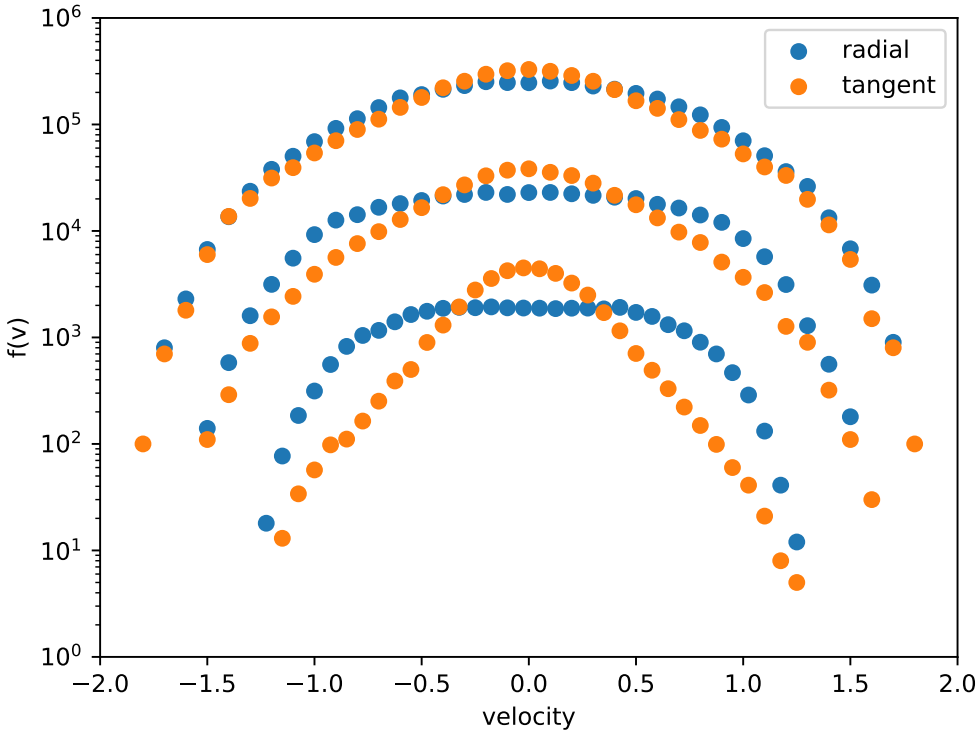

Figure 5.10: The three radial bins data for radial and tangential velocities in the cold collapse simulation. The three radial bins were chosen near the slope of $\gamma_0 = -1.6, -2.0, -2.4$ (From top to bottom), and the $\gamma_0 = -1.6, -2.0$ data were shifted vertically for easy reading. Each data point represents the number of particles within a velocity bin $\Delta v = 0.1$.

The second set of numerically simulated data is the so-called explicit energy exchange simulation. Various types of energy exchange take place between collisionless particles, particularly through violent relaxation and dynamical friction. Therefore, the numerical set-up take into account a perturbation in which the spherical symmetry is preserved, but they permit the particles to exchange energy. Each radial bin is designed to preserve energy with instantaneous energy exchange, ensuring that the perturbation itself has no impact on the density or dispersion profiles. Afterward, the system evolves with normal collisionless dynamics. Similarly, we divide the equilibrium structure into radial bins and then extract the radial and the tangential velocity data. We plot the velocity data in Fig.5.11. The three radial bins were chosen near the slope of $\gamma_0 = -1.7, -2.4 - 3.0$.

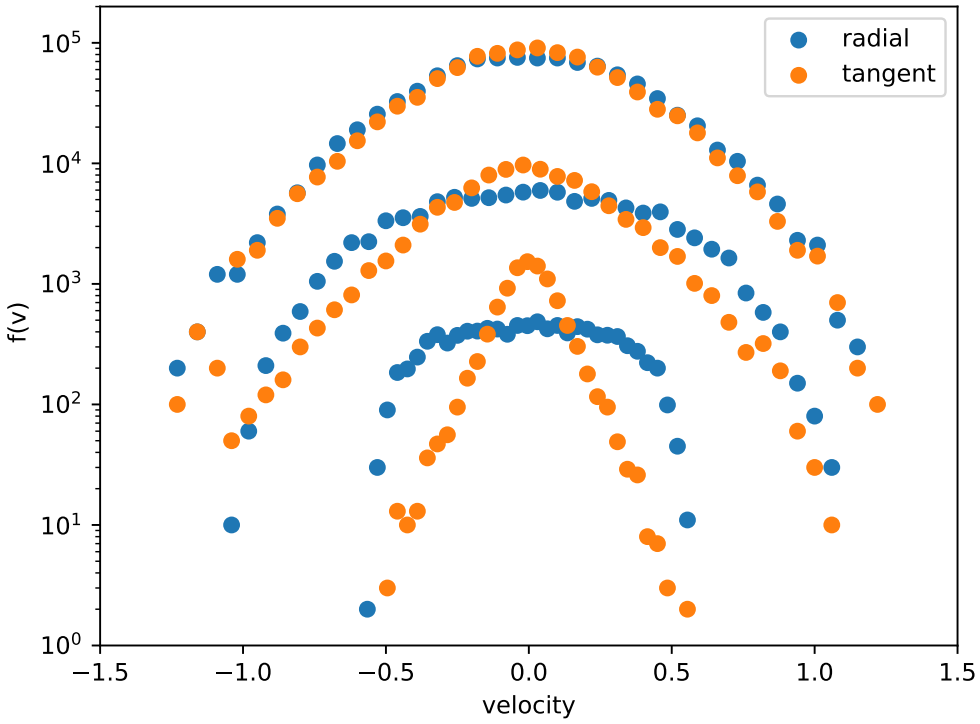

Figure 5.11: The three radial bins data for radial and tangential velocities in the explicit energy exchange simulation. The three radial bins were chosen near the slope of $\gamma_0 = -1.7, -2.4 - 3.0$ (From top to bottom), and the $\gamma_0 = -1.7, -2.4$ data were shifted vertically for easy reading. Each data point represents the number of particles within a velocity bin $\Delta v = 0.07$.

5.3.2 fitting and parameter estimation for the velocity data

When fitting our radial and tangential velocity distribution model to the real simulation data, we adopt error-bars on these data. We assume that the horizontal (velocity) error for each data point corresponds to the width of velocity bin Δv,

while the vertical (frequency) errors are taken as the square root of the counts in each velocity bin. This assumption is based on considering the particles in each velocity bin follow a Poisson distribution. In total, we have four parameters to fit for radial or tangential velocity distribution data: the normalization factor $N_r(N_t)$, the radial distance a, the potential $\phi(a)$, the parameter λ.

From an ideal perspective, if our model is the truth, when fitting the radial and tangential data independently in each bin, there should be two constraints for the fitting parameters of the data: first, since the three radial bins data are taken from one halo structure, the value of λ for the three radial bins should be the same; second, for each radial bin, the fitting parameters (a, ϕ) for the radial and tangential data should also be the same. Instead of fitting the radial and tangential data independently, we choose to jointly fit the radial and tangential data for each bin by using the same values of a and $\phi(a)$ in the fitting algorithm, i.e. we define the total logarithmic likelihood function as the sum of the radial and tangential parts

$$\begin{aligned} &ln\mathcal{L}(\text{rad and tan data}|N_r, N_t, a, \phi(a), \lambda) \\ &= ln\mathcal{L}_1(\text{rad data}|N_r, a, \phi(a), \lambda) + ln\mathcal{L}_2(\text{tan data}|N_t, a, \phi(a), \lambda) \end{aligned} \tag{5.17}$$

where `rad` and `tan` data represent the radial and tangential velocity data in each radial bin. With this joint fitting, the second constraint could be easily implemented. Then, we employ Bayesian inference with flat priors and MCMC sampling method to explore the posterior distributions of parameters given the velocity data from each radial bin. We use 300 random walkers, and each walker takes 5000 steps. After excluding 10% of the samples in the burning phase, we finally obtain the samples that can be used to analyze our model. The contour plots of these MCMC samples are shown in Appendix.7.4.

The fitting parameters for each bin in the collapse simulation data are presented in Table.5.1. We show the median values as well as the upper and lower bound that enclose 68% of the MCMC samples. The normalization factors increase with γ_0, showing a positive correlation. The median values of radial distance a and potential $\phi(a)$ are reasonable, as they exhibit growth and decrease respectively with increasing γ_0. Additionally, for comparison with the fitting potential, we also show the local escape kinetic energy $v_{max}^2/2$ for each bin, where v_{max} represents the maximum velocity ($\approx$ local escape velocity) of each bin. Ideally, the fitting potential should be equal to local escape kinetic energy, represented by $\phi \approx v_{max}^2/2$. We could see from Table.5.1 that the fitting potential is approximately equal to the local escape energy. This supports the self-consistency of the fitting $\phi(a)$ in different radial bins. It is noteworthy that our model appears to violate the first constraint mentioned above, as the fitting λ values are not uniform. However, in practice, due to the size of radial bins and the limitation of particle numbers in the simulation, some flexibility in adhering to these constraints is expected.

To be more explicit, we present the fitting results to the three radial bins of collapse simulation in Fig.5.12. From top to bottom, we present the data and fits for the bins with $\gamma_0 = -1.6, -2.0, -2.4$. In each plot, we show both the radial and tangential velocity data along with the corresponding error-bars, as mentioned above. The solid blue curve represents the radial velocity distribution, while the solid red curve represents the tangential velocity distribution, both predicted by the

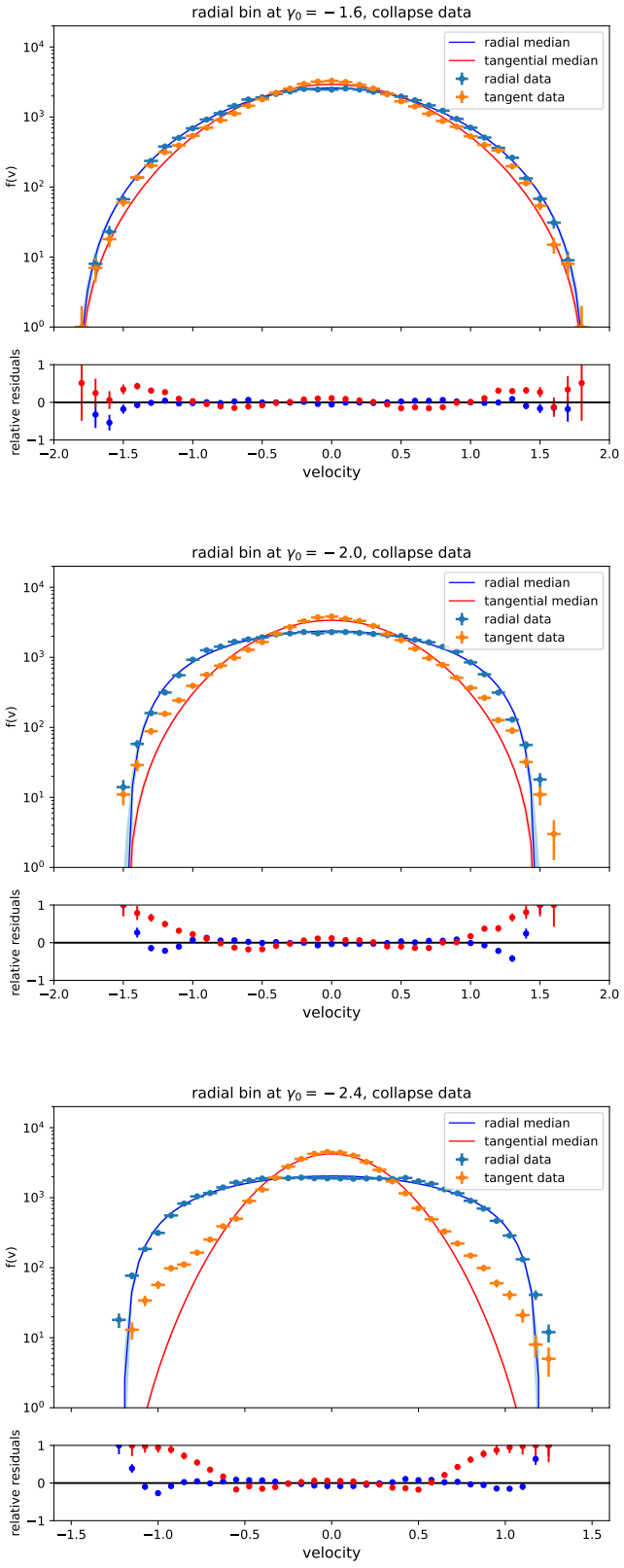

Figure 5.12: The radial and tangential velocity fitting results to the three radial bins in the cold collapse simulation. From top to bottom are respectively $\gamma_0 = -1.6, -2.0, -2.4$. The radial data and the median radial distributions are colored blue, while the tangential results are colored red. The 1-sigma band of radial distributions are colored shallow blue, and tangential bands are colored shallow red. The relative residuals are also given for the radial (colored blue) and tangential data (colored red).

	$\gamma_0 = -1.6$	$\gamma_0 = -2.0$	$\gamma_0 = -2.4$
N_r	$185.114^{+34.140}_{-27.785}$	122091^{+67844}_{-50666}	$1064057^{+678118}_{-448879}$
N_t	$38.782^{+7.105}_{-5.800}$	21814^{+12125}_{-9034}	115227^{+73459}_{-48646}
a	$1.033^{+0.033}_{-0.030}$	$4.601^{+0.635}_{-0.643}$	$9.175^{+1.480}_{-1.361}$
$\phi(a)$	$1.684^{+0.024}_{-0.024}$	$1.095^{+0.014}_{-0.010}$	$0.724^{+0.007}_{-0.006}$
$v_{max}^2/2$	1.805	1.280	0.781
λ	$0.770^{+0.010}_{-0.009}$	$1.953^{+0.259}_{-0.259}$	$1.996^{+0.318}_{-0.292}$

Table 5.1: The best estimated parameters for the three radial bins in the collapse simulation. We show the median values with upper and lower bounds enclosing 68% of the MCMC samples. Additionally, we display the local escape energy $v_{max}^2/2$ for each bin as reference to compare with the potential.

median values of the MCMC samples. Additionally, we include the 1-sigma band of the velocity distribution predicted by the MCMC samples. The band is colored in shallow blue for the radial fit and shallow red for the tangential fit, though it may be relatively small for some bins. The relative residuals, defined as the difference between the data and the solid curves, are calculated as

$$\frac{\text{data} - \text{solid curve}}{\text{data}} \tag{5.18}$$

are also shown in the bottom of each subplot in Fig.5.12. The blue and red dots respectively represent the radial and tangential relative residuals. We can see from Fig.5.12, our model gives a good fit to all three bins especially for the radial data, despite some residuals remaining. The radial fits of our model are much better than the tangential fits. Our model only performs well in the low velocity regime of tangential data and underestimate their high velocity tails. The relative residuals increase as γ_0 and velocity increase. Nevertheless, as expected, the radial and tangential velocity converge to each other at higher velocities. The smaller the value of γ_0, the higher the similarity of radial and tangential velocity distributions.

We have also shown the fitting parameters of the three radial bins for the explicit energy exchange simulation data in Table.5.2. Similar to the situation with the collapse simulation data, we also show the upper and lower bounds that encompass 68% of the MCMC samples, together with the median values. As γ_0 rises, so do the normalization factors. The median of radial distance a and potential $\phi(a)$ are following a good trend along with γ_0. The fitting $\phi(a)$ in different radial bins are also self-consistent since $\phi \approx v_{max}^2/2$ in each bin. The fitted bands of the radial bin at $\gamma_0 = -3$ is quite large compare to the other two radial bins. In addition, because fitting λ vary among different bins, we can also observe that our model appears to break the first constraint, similarly to the case in the collapse simulation.

We also plot the fitting results for the explicit energy exchange simulation data in Fig.5.13. From top to bottom are respectively the $\gamma_0 = -1.7, -2.4, -3.0$ bins data and fits. As in the collapse simulation case, we also show the tangential and radial velocity data along with the previously mentioned error bars in each plot.

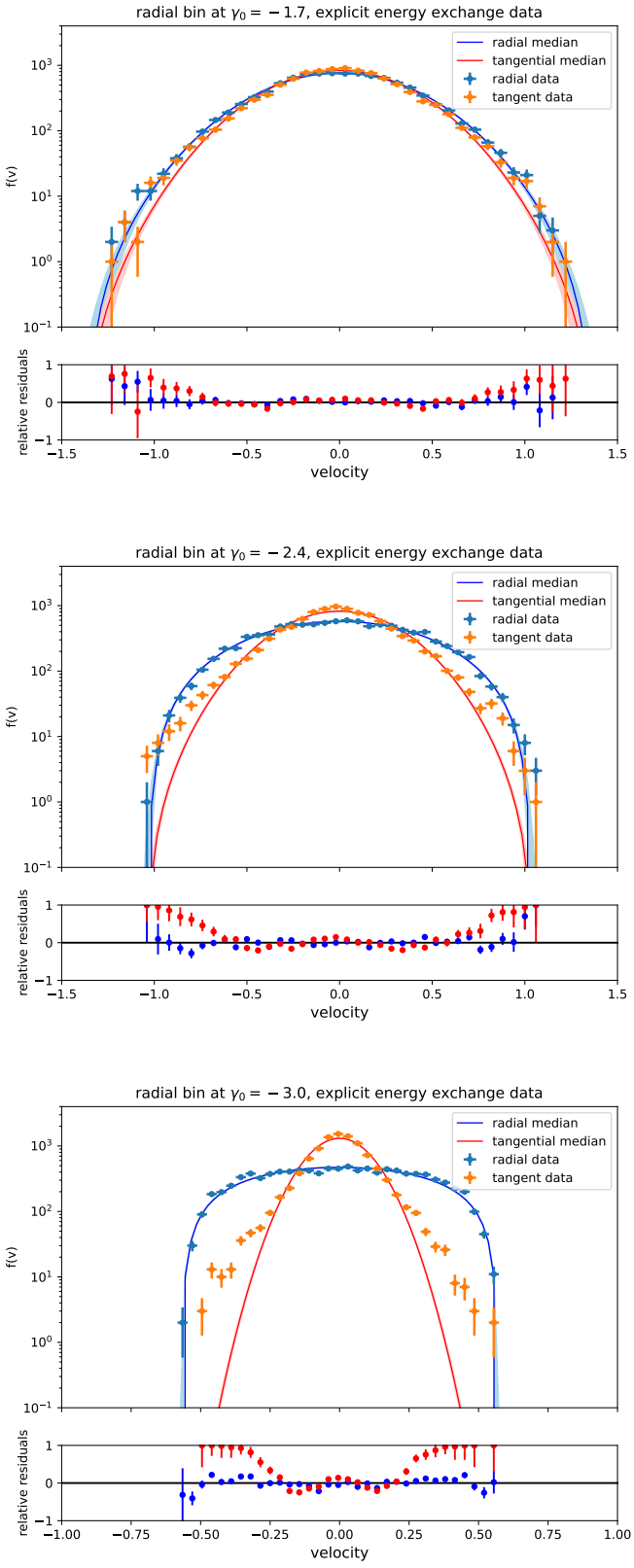

Figure 5.13: The radial and tangential velocity fitting results to the three radial bins in the explicit energy exchange simulation. From top to bottom are respectively $\gamma_0 = -1.7, -2.4 - 3.0$. The radial data and the median radial distributions are colored in blue, while the tangential results are colored in red. The 1-sigma band of radial distributions are colored in shallow blue, and tangential bands are colored in shallow red. The relative residuals are also given for the radial (colored in blue) and tangential data(colored in red).

	$\gamma_0 = -1.7$	$\gamma_0 = -2.4$	$\gamma_0 = -3.0$
N_r	$2.776\,^{+6.585}_{-1.559}$	$3107\,^{+762}_{-913}$	$83211678\,^{+393502366}_{-71717150}$
N_t	$0.363\,^{+0.855}_{-0.204}$	$342.9\,^{+84.6}_{-100.2}$	$3249348\,^{+15434273}_{-2798681}$
a	$0.737\,^{+0.070}_{-0.057}$	$2.370\,^{+0.112}_{-0.132}$	$38.039\,^{+29.741}_{-18.075}$
$\phi(a)$	$0.936\,^{+0.078}_{-0.104}$	$0.539\,^{+0.017}_{-0.007}$	$0.164\,^{+0.001}_{-0.001}$
$v^2_{max}/2$	0.832	0.562	0.174
λ	$0.404\,^{+0.013}_{-0.007}$	$0.631\,^{+0.023}_{-0.029}$	$2.875\,^{+2.259}_{-1.361}$

Table 5.2: The best estimate parameters for the three radial bins in the explicit energy exchange simulation. We show the median values along with upper and lower bounds that enclose 68% of the MCMC samples. In addition, we also show the local escape energy $v^2_{max}/2$ for each bin as reference for comparison with the potential.

The radial and tangential velocity distributions predicted by the median value of the fitting parameters are also shown by the solid blue and red curves. We present the 1-sigma band and relative residuals with the same setup in the collapse simulation case. We can also see from Fig.5.13 that the situation is almost the same to the collapse simulation case. The patterns are repeating. Our model provides a fair fit to all three bins, particularly for the radial data, while it fails again on predicting the high velocity tails of the tangential data. As γ_0 and velocity increase, the relative residuals also increase.

Although there are slight differences, the similarity of the data and fits in both cold collapse and explicit energy exchange simulation reveals an universal dark matter velocity distributions. The basic trends and structures of dark matter velocity distributions were captured by our model. The data suggests that our model could be relevant to describe the distribution of dark matter particles, especially for the radial velocity distributions. In principle, we could use the fitted a and the normalized potential $\phi(a)/\lambda^2$ of three radial bins in each simulation to reproduce the density profiles of the original simulated halo. However, the discrepancy of fitting λ to three bins add large uncertainties on the normalized potential $\phi(a)/\lambda^2$. So, we will leave this as a problem that needs to be addressed in the future.

5.4 Conclusion and discussion

In this paper, we have suggested and analysed a phenomenological model of spherically symmetric anisotropy dark matter phase space distribution function as presented in Eq.(5.1). We first introduced our distribution function and demonstrated their predictions on integrated quantities, which are typically analysed in numerical simulations, namely the density profile (5.6), the anistropy (5.9) and phase space density (5.13). In addition, we also give the velocity magnitude (5.8), the radial and tangential velocity distributions in analytical forms (5.15) (5.16). To assess the utility of our velocity distributions, we have respectively compared with radial and

tangential velocity data which were extracted from different radial bins of equilibrium dark matter halos. We verify our results in two different simulation schemes, the cold collapse and explicit energy exchange which effectively cover a wide range of possible equilibrium processes. The fits show good performance and the results are promising, especially for the radial data (across the whole velocity range) and the lower velocity regime of tangential data. There is agreement in estimating the relevant parameters of the radial and tangential velocity data.

Despite the advantages of providing good fits to the velocity distributions, there are also some potentially important limitations to our model that we wish to address. Our model faces the first challenge in predicting the pseudo phase space density, which does not follow a single, unbroken power law. The second limitation arises when comparing with the data, as significant deviations are observed, especially in the high-velocity tails of tangential data. Additionally, the predicted parameter λ differs among three bins of the same halo. These observations could indicate that our model is missing some additional features of dark matter halos. However, it is essential to verify this issue using another independent simulation program since the error could originate from the data rather than the model. If these limitations have been confirmed by other simulations, we should explore possible ways to improve our model. Our model only uses the linear order of binding energy ϵ and exponent Q, which represents the simplest case. One could consider using ϵ^n or Q^n in the exponent of (5.1) with $n \geq 0$. Introducing non-linearity could potentially compensate for these limitations. Furthermore, the r_0/r factor in our phase space distribution (5.1) could also be a simplification of some complicated function involving integrated quantities such as ϵ and Q. If r_0/r could be replaced by functions of integrated quantities, the model would be much plausible, indicating its adherence to the Jeans theorem and transcending a mere phenomenological model.

Chapter 6

Summary and outlook

Black holes and dark matter are both crucial subjects within the current physics community. Due to limitations in observational precision, numerous mysteries persist, requiring further exploration. Additionally, there are no definitive results regarding the true nature of black holes and dark matter on the theoretical front. Studying the phenomenology of black holes and dark matter can serve as a bridge between theory and observations. This approach enables us to glean insights for the development of both theory and experiments.

6.1 Summary of this thesis

In this thesis, we have delved into various phenomenological aspects of two well-known alternative black holes beyond GR. The alternative black holes under investigation are the rotating regular black hole and the rotating hairy black hole, intricately connected to two renowned theorems in classical GR: the singularity theorem and the no hair theorem. These black hole metrics serve as significant avenues for exploring the potential violation of these theorems and extending our understanding beyond GR. The phenomenological aspects we have explored encompass superradiance, quasinormal modes, and energy extraction via the magnetic reconnection mechanism. Superradiance has been investigated using the matching-asymptotic method, quasinormal modes have been computed through the continued fraction method, and the Comisso-Asenjo formalism has been employed to study magnetic reconnection occurring within the ergosphere. These phenomena hold profound implications on the theoretical front, and, concurrently, they bear the potential for future observational confirmation. Our application of these phenomenological studies extends to both types of alternative black holes. Through our investigations, we aim to contribute not only to the theoretical understanding of these exotic black holes but also to pave the way for potential observations in the future.

In the study of rotating regular black holes using the approximation method, we have derived the effective horizons and subsequently examined the behavior of scalar fields around such black holes. In relation to the phenomenon of superradiance, our findings indicate that the regular parameter plays a significant role in the amplification of incident scalar waves. Notably, an increase in the regular parameter leads to the extension of the cutoff frequency for superradiance modes to higher values. When it comes to quasinormal modes, the influence of the regular

parameter becomes pronounced only when the spin of the black hole is sufficiently high. Furthermore, a larger value of the regular parameter has the effect of lowering the threshold and enhancing the power and efficiency associated with the extraction of energy through the Comisso-Asenjo magnetic reconnection mechanism.

For the study of rotating hairy black holes, we also employed an approximation method for the horizons. Subsequently, we delved into the gravitational perturbations surrounding this black hole. It is not straightforward to directly use Teukolsky equations to describe the gravitational perturbation around non-GR black holes. However, leveraging the assumption of the smallness of the effective charge Q_{effect}, we could managed to employ the Teukolsky equations to describe the gravitational perturbations around rotating hairy black holes. Two hairy parameters of rotating hairy black holes exert a combined influence on superradiance modes. Their impact becomes pronounced only when the frequencies of gravitational waves close to the critical threshold. As for the quasinormal modes, the hairy parameters exhibit no significant alteration to the overall trend in quasinormal modes concerning black hole spin. Nonetheless, they do introduce slight variations in the slopes of both real and imaginary parts of the quasinormal modes. In the context of energy extraction through magnetic reconnection phenomena, the combinations of hairy parameters leading to a larger black hole spin expand the parameter spaces, enhancing the power and efficiency of energy extraction.

Additionally, we have proposed and investigated a phenomenological model of dark matter distributions. Given the absence of a satisfactory theory for predicting the distributions of dark matter halos in simulations, we utilize an phenomenological model of phase space distribution to comprehensively describe the universal properties and the velocity distributions observed in simulations. Initially, we present the analytical properties of our model, including a NFW-like density profile. Subsequently, we compare the velocity magnitude distribution and velocity component distributions with simulation data. Regarding the velocity magnitude distribution, our model exhibits a relatively more pronounced suppression in the high-velocity tails, resulting in a superior fit compared to the standard halo model. Furthermore, we compare the analytical formulas of radial and tangential velocity distribution with the velocity data extracted from radial bins of two simulation schemes. The fitting results demonstrate the excellent performance of our model for the radial velocity data across the entire velocity range and the lower velocity regime of tangential data. This suggests that our model provides a helpful tool for describing the intricate features of dark matter distributions.

6.2 Outlook for future studies

While these interesting results and findings are listed above, there is still plenty of room for improvement and extension in our research.

In our study on superradiance and quasinormal modes of two alternative black hole scenarios, we employed an approximation for the horizons, thereby limiting the parameter spaces available for exploration. However, a more comprehensive approach would involve a fully numerical investigation [227, 228, 229], allowing us to extend the range of parameter spaces and providing our results as a calibration or verification for numerical findings. Additionally, while our studies were based

on the linear perturbations of black hole, it has been suggested that the nonlinear quasinormal mode originating from high order perturbations of black hole spacetime would be detectable in future ground-based and space-based gravitaional detectors [22]. The approximation method used in our studies could extend to the studies of nonlinear quasinormal modes of these two alternative balck holes. For energy extraction through magnetic reconnection, it is crucial to note that this phenomena occurs within the equatorial plane of black holes, typically accompanied by the presence of an accretion disk. The outflowing plasma carrying energy extracted from the black hole through magnetic reconnection has the potential to heat up the inner region of the accretion disk surrounding the black hole. This phenomenon may lead to a luminosity anomaly in observations of the accretion disk [230], presenting an opportunity for comparison with empirical data to verify the existence of these alternative black holes.

The phenomenological phase space distribution model we have proposed has room for improvement in both theoretical and simulation aspects. If our model were modified to satisfy the Jeans theorem, it would become a more appealing representation for dark matter distribution. Additionally, it is crucial to validate the significant limitations of our model through other simulations. Moreover, our velocity distribution could be further applied to the analysis of dark matter direct detection experiments [30, 31, 32, 33]. This is especially noteworthy as our velocity magnitude and radial velocity distribution have already demonstrated excellent fitting, and they are also analytically derived.

Chapter 7

Appendix

7.1 The errors of approximation method for rotating regular black holes

In subsection.3.1.2, we used the analytically approximation to solve the Delta function (3.4). To show the accuracy of this method, we plot the errors of high order solutions in Fig.7.1 as a function of black hole spin a, given different regular parameter k. We plot the errors up to the second order for event horizon and third order for inner horizon. The errors denoted as $E^i_\pm$ are computed by comparing to the numerical solutions $r^{num}_\pm$ of (3.4), i.e,

$$E^i_\pm = \frac{\left|r^i_\pm - r^{num}_\pm\right|}{r^{num}_\pm} \tag{7.1}$$

where $i = I, II, III$ represents the i-th order solution.

We can see from Fig.7.1, the approximation errors drop down as the order goes up for both event and inner horizon, besides that, we can see the errors of event horizon are tiny ($\ll 10^{-3}$) even in the first order although they are slowly going up along with the black hole spin. However, the errors of inner horizon are significantly large at first order, but they drop down quickly as the order and black hole spin goes up.

From the order of magnitude, the errors of inner horizon are significantly larger than that of event horizons $E^i_- \gg E^i_+$ even in the high spin regime. Therefore, we shall focus on the inner horizon errors E^i_-, because it will dominate the errors of our approximation results. We plot a horizontal line $E^i_- = 10^{-2}$ and a vertical line $a = 0.1$. We would like to control the errors such that they always below 10^{-2} from $a = 0.1$ to 0.9. Then the regular parameter k should be chosen not greater than $0.01M$, and third order solutions are sufficient for our goal.

The final equation to compute the amplification factor and quasinormal modes are (3.38) and (3.49) respectively, the essential quantities Q, ξ, $\alpha_n, \beta_n, \gamma_n$ for these equations are all proportional to $\hat{r}_+$, $\hat{r}_+$, ω or their quadratic. The accuracy of amplification factor and quasinormal modes, because of using the approximation solutions (3.12) and (3.13), are therefore in the order of $(E^{III}_-)^{2l+2}$ and E^{III}_-, respectively. So, the approximation has almost no effect in amplification factor, while the accuracy of quasinormal modes are always higher than 10^{-2}, even 10^{-6} when $a \gtrsim 0.3$, provided with the regular parameter $k \leq 0.01M$.

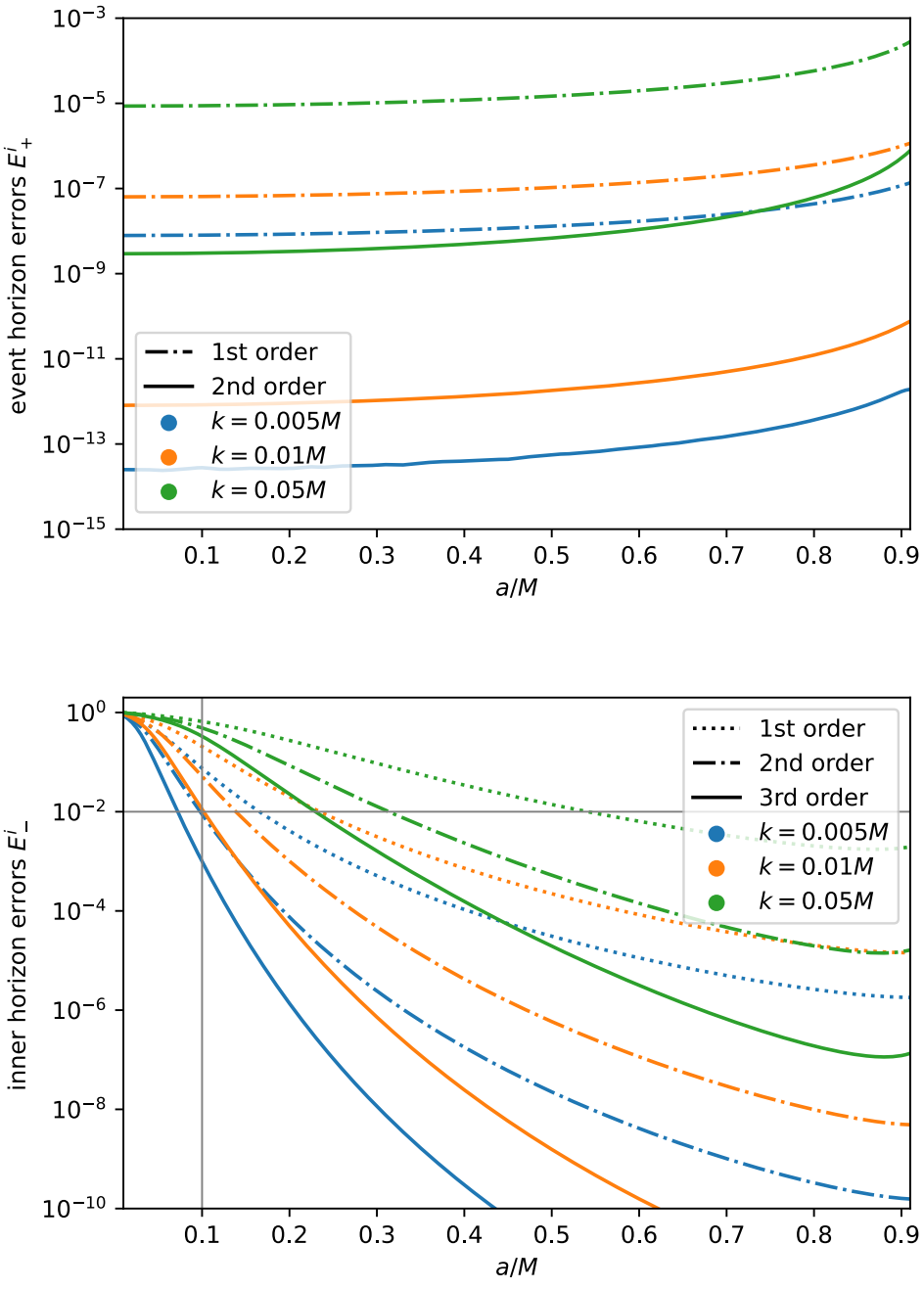

Figure 7.1: upper and lower plots are respectively the errors of high order event horizon and inner horizon, with regular parameter $k = 0.005, 0.01, 0.05$ and black hole spin $a = 0.01$ to 0.91.

7.2 The errors of approximation method for rotating hairy black holes

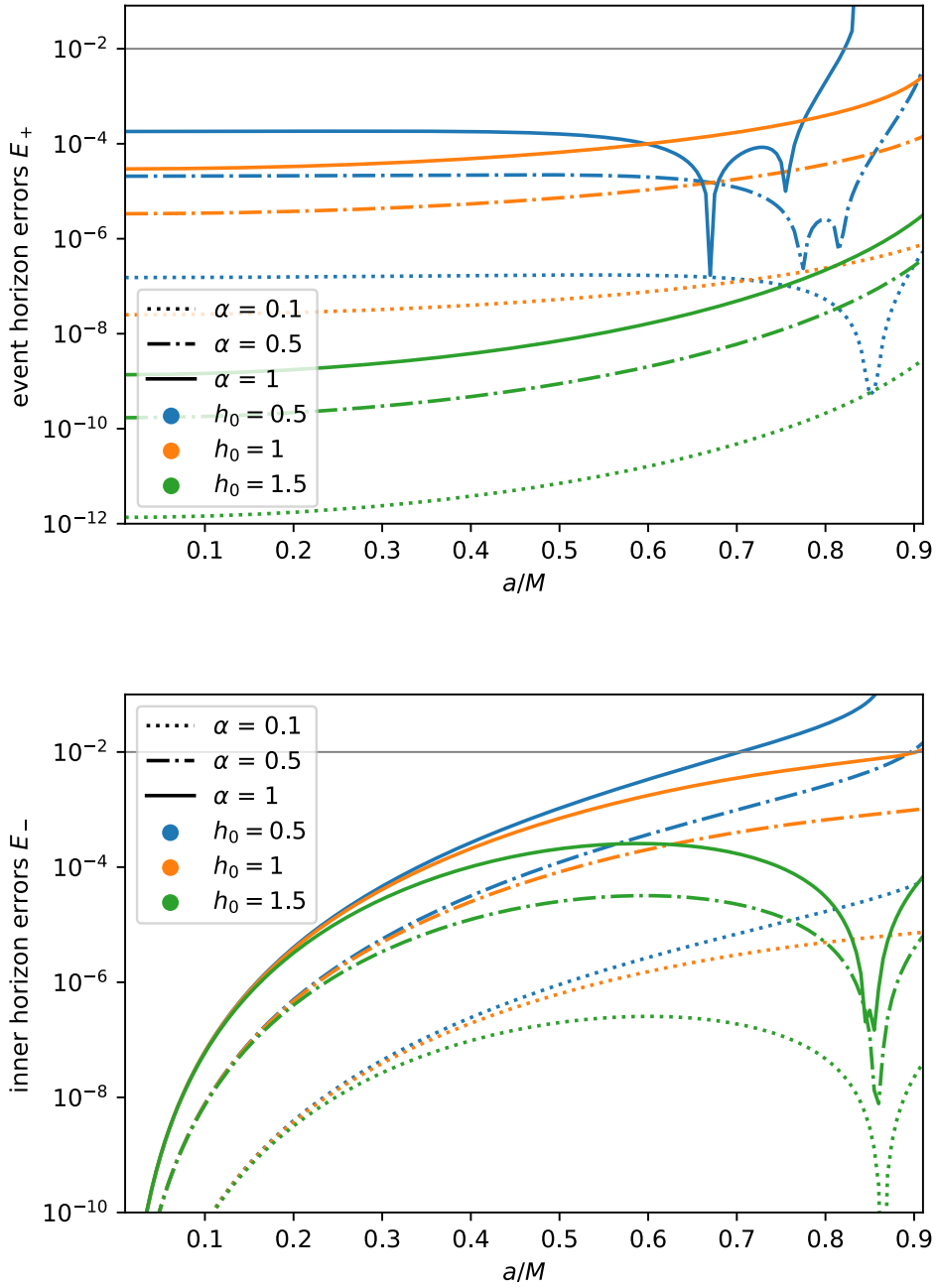

Figure 7.2: Upper and lower plots are respectively the errors of second order event horizon and inner horizon, with parameter $\alpha = 0.1, 0.5, 1$, $l_0 = 0.5, 1, 1.5$ and black hole spin $a = 0.01$ to 0.91.

In subsection.3.2.2, we used the analytical approximation to solve the Delta function (3.51). To show the accuracy of this method, we plot the errors of the second order solutions in Fig.7.2 as a function of the spin a of the black hole at

different parameters α, h_0. The errors, denoted as $E_\pm$, are calculated by comparison with the numerical solutions $r_\pm^{num}$ of (3.51), i.e,

$$E_\pm = \frac{\left|\hat{r}_\pm - r_\pm^{num}\right|}{r_\pm^{num}} \tag{7.2}$$

We can see from Fig.7.2, the approximation errors for both the event horizon and the inner horizon increase with spin. There is some oscillation for the event horizon errors as the black hole spin approaches higher values. We want to control the errors so that they never increase above 10^{-2} within the spin intervals $a = 0.01$ to 0.9. Therefore, we draw a horizontal line $E_\pm = 10^{-2}$ in Fig.7.2. Then the parameters α, h_0, a should be chosen within a certain range so that the approximation works well, and for this purpose second order solutions are sufficient.

It is true that the original Delta function depends not only on the roots, but everywhere in the radial distance. However, replacing the original Delta function (which is a transcendental function) with a quadratic function gives a very good approximation for $r \gtrsim 2M \approx \hat{r}_+$ (see Fig.7.3), i.e., outside the event horizon, since all perturbations occur in the region $r \gtrsim 2M$. The errors are calculated by

$$\frac{\Delta_{approx} - \Delta_{original}}{\Delta_{original}} \tag{7.3}$$

where Δ_{approx} is given by Eq.(3.58) and $\Delta_{original}$ is the exact Delta function in metric (4.23). We can clearly see that the errors decrease rapidly as r becomes large. The larger α and smaller h_0, the larger the errors. The spin has only a small effect. The errors go below a few percent when $r \gtrsim 2M$. One can also notice that the Δ_{approx} is always slightly larger than the $\Delta_{original}$.

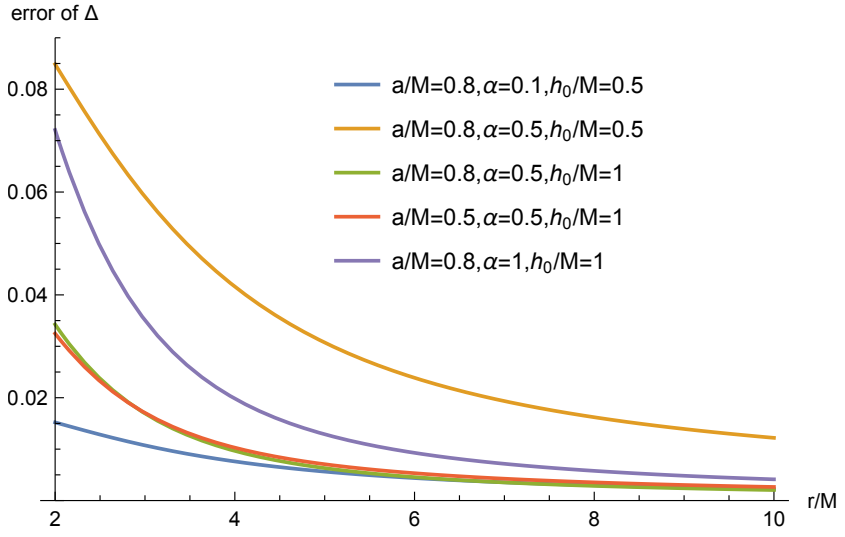

Figure 7.3: The relative error of Delta as a function of radial distance. We plot the errors with several combinations of black spin a, α and h_0 as references. These combination values will were used in this work.

For a quadratic function Eq.(3.58), the roots determine its behavior everywhere outside the event horizon. Moreover, the final equation for calculating the amplification factor and quasinormal modes are (3.82) and (3.94) respectively, the essential

quantities Q, k, $\alpha_n, \beta_n, \gamma_n$ for these equations are all proportional to $\hat{r}_+$, $\hat{r}_-$ or their quadratic. Therefore, the accuracy of amplification factor and quasinormal modes, because of using the approximation solutions (3.56) and (3.57), are therefore in the order of $(E_\pm)^{2l+2}$ and $E_\pm$, respectively. Choosing the parameters within a certain range $\alpha \in [0, 0.5], h_0 \in [0.5, 2], a \in [0.01, 0.9]$, the errors of amplification factor and quasinormal modes are always below the order of 10^{-4l+4} and 10^{-2}, respectively.

7.3 Special functions used in this thesis

- Gamma function
$$\Gamma(x) = (x-1)! \tag{7.4}$$

- Hypergeometric functions
$$F(a,b;c;x) = \sum_{n=0}^{\infty} \frac{a^n b^n}{c^n} \frac{x^n}{n!}, \quad \text{for} |x| < 1. \tag{7.5}$$

- Confluent hypergeometric function
$$U(a,b,x) = \frac{\Gamma(1-b)}{\Gamma(a-b+1)} M(a,b,x) + \frac{\Gamma(b-1)}{\Gamma(a)} x^{1-b} M(a-b+1, 2-b, x) \tag{7.6}$$
where $M(a,b,x)$ is the Kummer function, defined as
$$M(a,b,x) = \sum_{n=0}^{\infty} \frac{a^n}{b^n} \frac{x^n}{n!} \tag{7.7}$$

- Error function
$$\text{erf}(x) = \frac{2}{\sqrt{\pi}} \int_0^x e^{-t^2} dt \tag{7.8}$$

- Imaginary error function
$$\text{erfi}(x) = -i \, \text{erf}(i \, x) \tag{7.9}$$

- Dawson integral
$$\text{DawsonF}(x) = e^{-x^2} \int_0^x e^{t^2} dt \tag{7.10}$$

7.4 Contour plot of MCMC samples

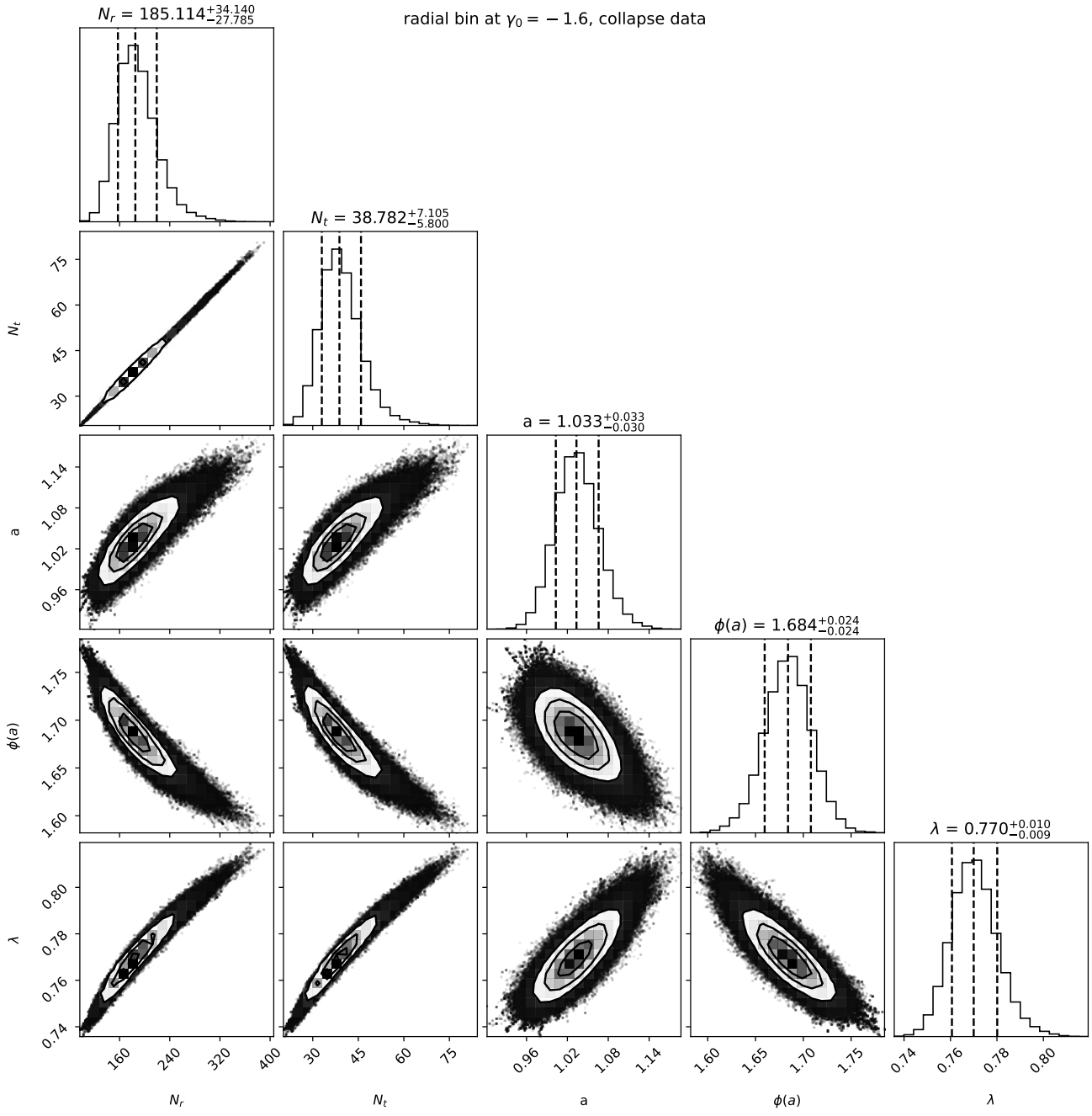

Figure 7.4: The contour plots show the MCMC samples for the posterior of radial bin $\gamma_0 = -1.6$ in the collapse simulation. The contours on the plots represent the regions enclosing 16%, 50%, and 84% of the samples. The values displayed above each subplot are the median values, along with the upper and lower bounds enclosing 68% of the samples.

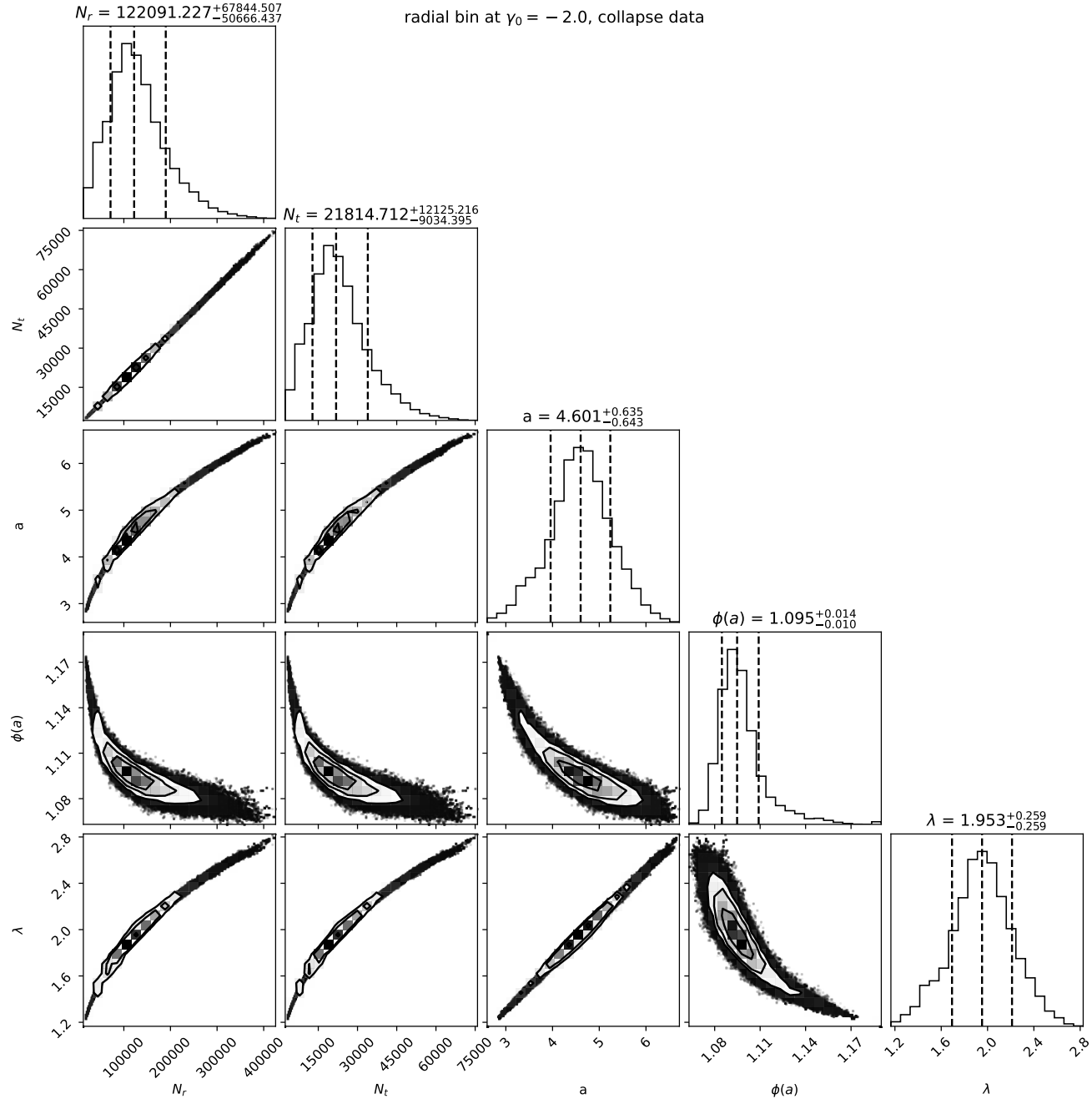

Figure 7.5: The contour plots show the MCMC samples for the posterior of radial bin $\gamma_0 = -2.0$ in the collapse simulation. The contours on the plots represent the regions enclosing 16%, 50%, and 84% of the samples. The values displayed above each subplot are the median values, along with the upper and lower bounds enclosing 68% of the samples.

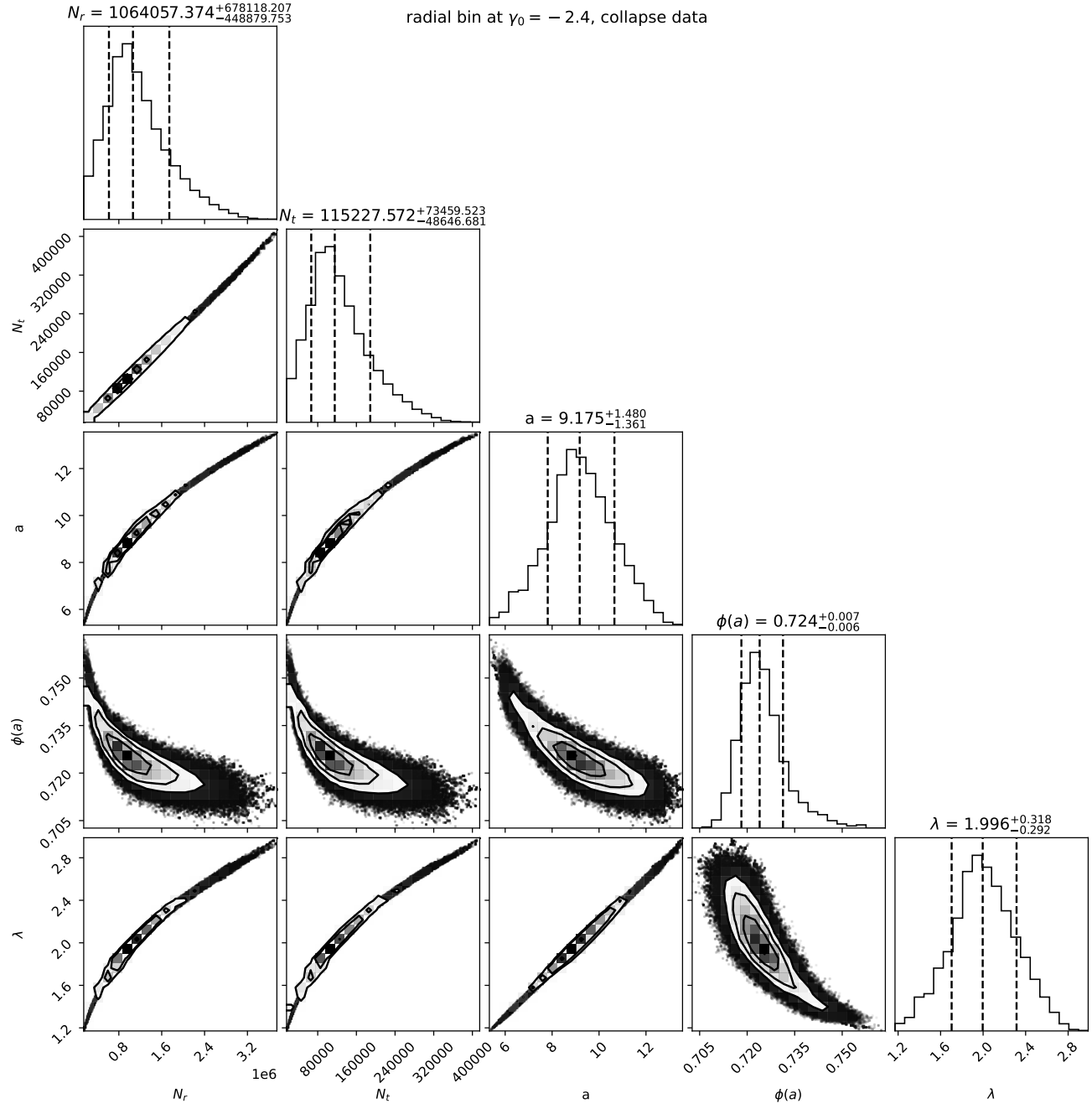

Figure 7.6: The contour plots show the MCMC samples for the posterior of radial bin $\gamma_0 = -2.4$ in the collapse simulation. The contours on the plots represent the regions enclosing 16%, 50%, and 84% of the samples. The values displayed above each subplot are the median values, along with the upper and lower bounds enclosing 68% of the samples.

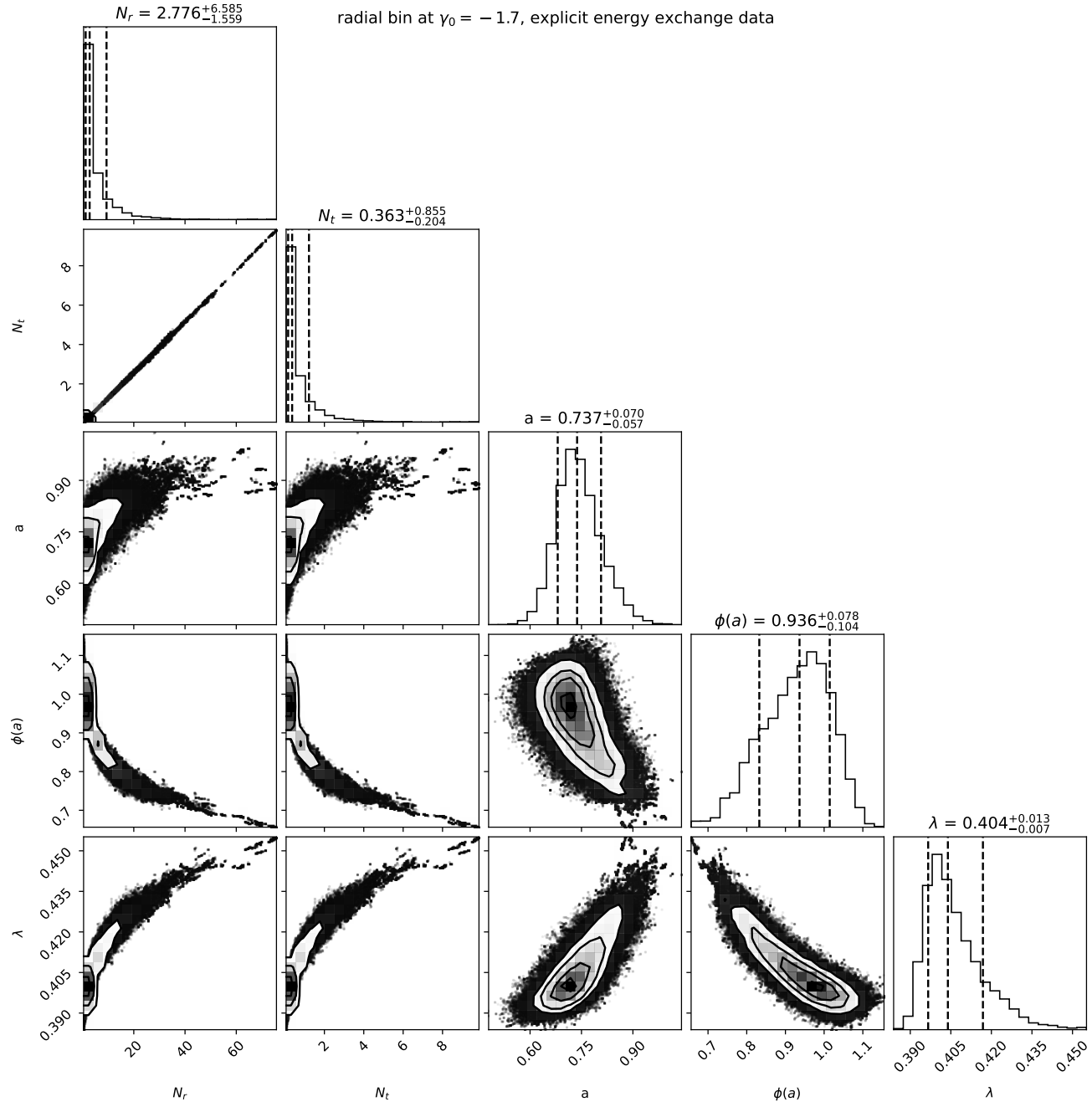

Figure 7.7: The contour plots show the MCMC samples for the posterior of radial bin $\gamma_0 = -1.7$ in the explicit energy exchange simulation. The contours on the plots represent the regions enclosing 16%, 50%, and 84% of the samples. The values displayed above each subplot are the median values, along with the upper and lower bounds enclosing 68% of the samples.

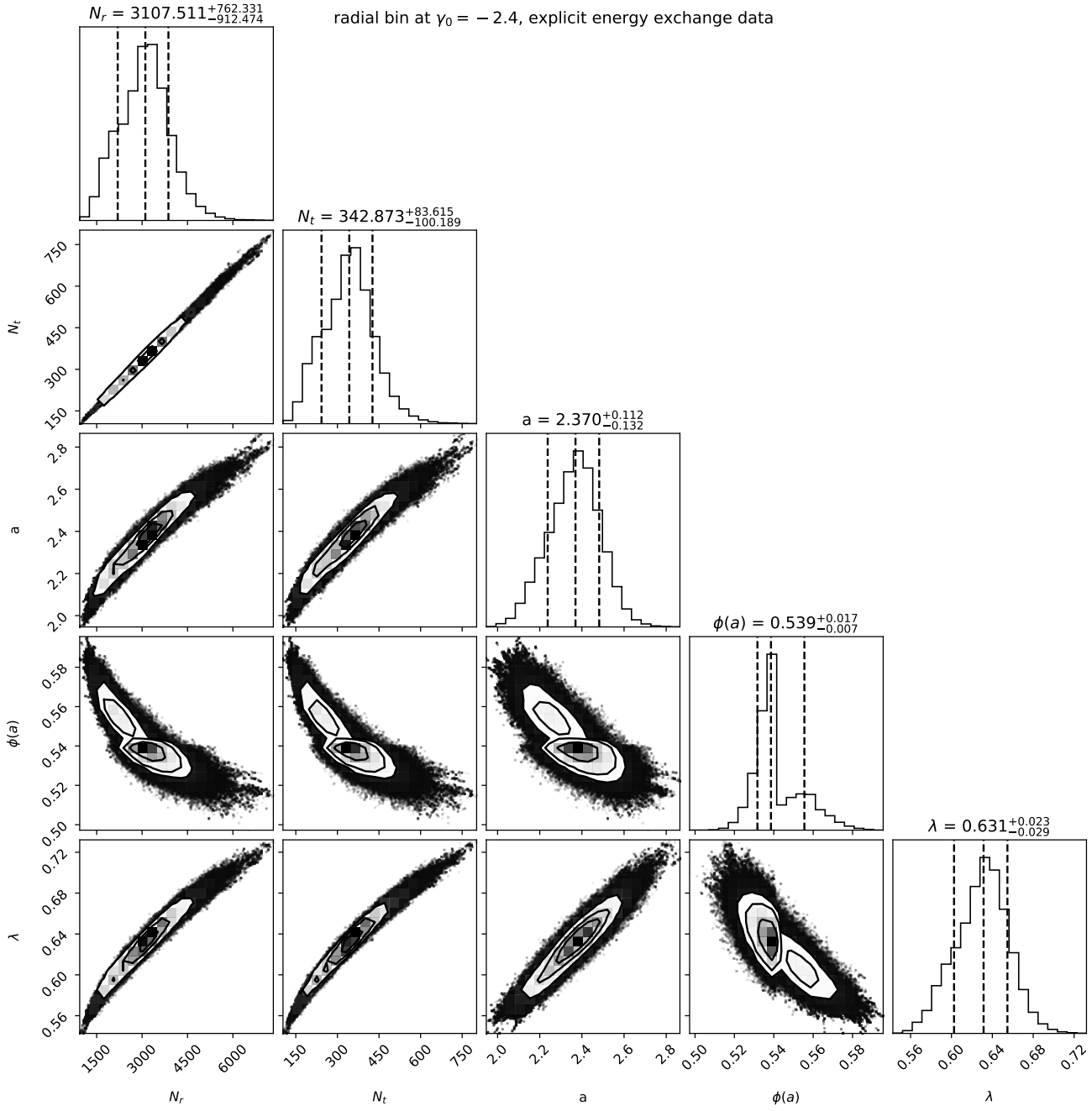

Figure 7.8: The contour plots show the MCMC samples for the posterior of radial bin $\gamma_0 = -2.4$ in the explicit energy exchange simulation. The contours on the plots represent the regions enclosing 16%, 50%, and 84% of the samples. The values displayed above each subplot are the median values, along with the upper and lower bounds enclosing 68% of the samples.

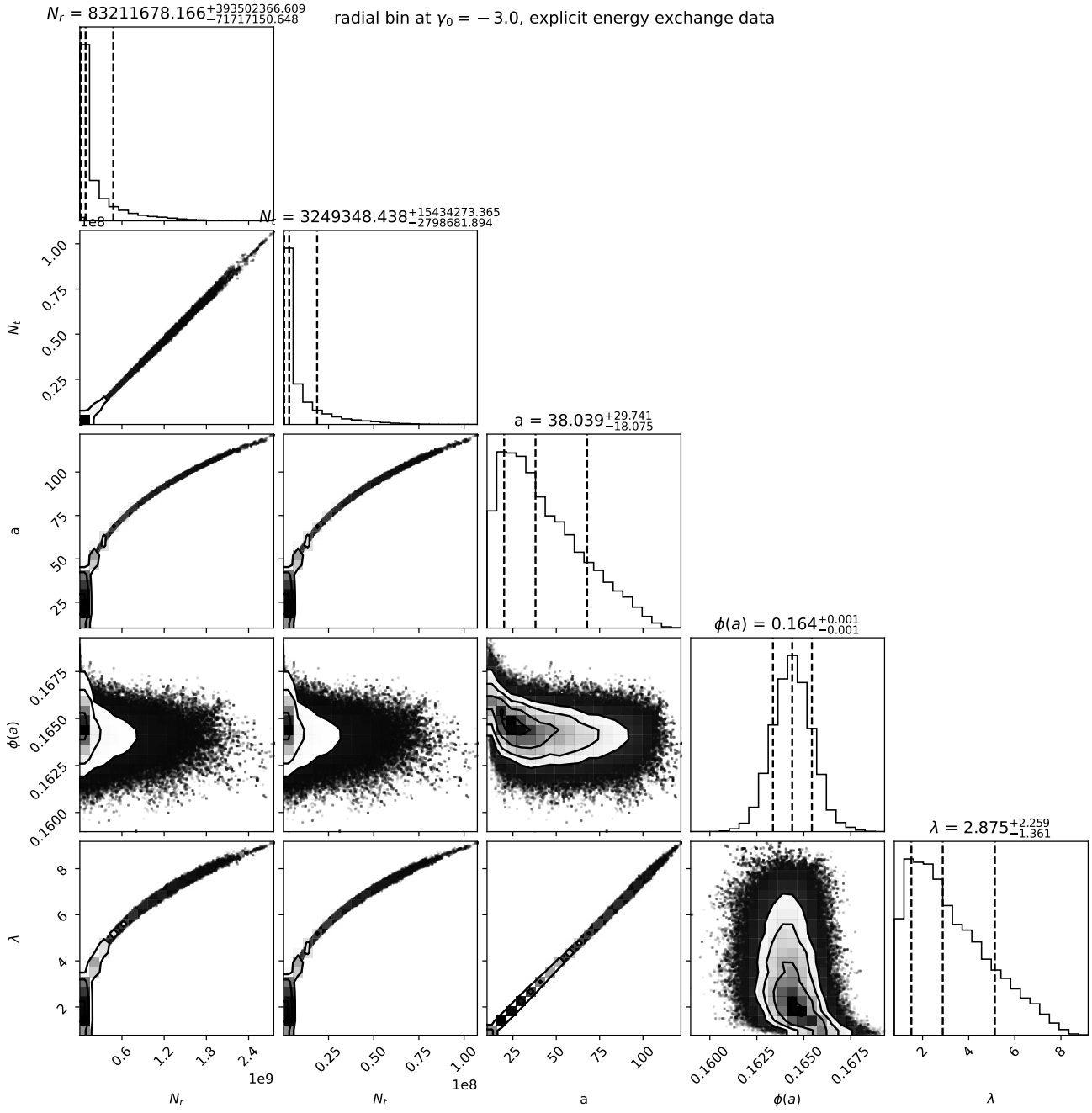

Figure 7.9: The contour plots show the MCMC samples for the posterior of radial bin $\gamma_0 = -3.0$ in the explicit energy exchange simulation. The contours on the plots represent the regions enclosing 16%, 50%, and 84% of the samples. The values displayed above each subplot are the median values, along with the upper and lower bounds enclosing 68% of the samples.

Bibliography

[1] B. P. Abbott *et al.*, (LIGO Scientific, Virgo), Phys. Rev. Lett. 116, 061102 (2016).

[2] K. Akiyama *et al.*, (Event Horizon Telescope), Astrophys. J. Lett. 875, L1 (2019).

[3] R. Penrose, Phys. Rev. Lett. 14, 57 (1965).

[4] S. W. Hawking, Phys. Rev. D. 14, 2460 (1976).

[5] B. Carter, Phys. Rev. Lett. 26, 331 (1971).

[6] S. W. Hawking, Comm. Math. Phys. 25, 152 (1972).

[7] D. C. Robinson, Phys. Rev. Lett. 34, 905 (1975).

[8] P. O. Mazur, Journal of Physics A Mathematical General. 15, 3173 (1982).

[9] J. D. Bekenstein, Phys. Rev. D. 51, 6608 (1995).

[10] H. Culetu, arXiv:1305.5964.

[11] H. Culetu, Int. J. Theor. Phys. 54, 2855 (2015).

[12] H. Culetu, Phys. Dark Univ. 14, 1 (2016).

[13] A. Simpson and M. Visser, Universe. 6, 8 (2019).

[14] S. G. Ghosh, Eur. Phys. J. C. 75, 532 (2015).

[15] A. Simpson and M. Visser, JCAP. 03, 03 (2022).

[16] A. Simpson and M. Visser, Phys. Rev. D. 105, 064065 (2022).

[17] J. Ovalle, R. Casadio, E. Contreras and A. Sotomayor, Phys. Dark Univ. 31, 100744 (2021).

[18] E. Contreras, J. Ovalle, R. Casadio, Phys. Rev. D. 103, 044020 (2021).

[19] P. Amaro-Seoane *et al.*, arXiv:1702.00786.

[20] M. Punturo *et al.*, Class. Quant. Grav. 27, 194002 (2010).

[21] I. Ota and C. Chirenti, Phys. Rev. D. 105, 044015 (2022).

[22] S. Yi, A. Kuntz, E. Barausse, E. Berti, M. H. Y. Cheung, K. Kritos and A. Maselli, arXiv:2403.09767.

[23] A. Arvanitaki, M. Baryakhtar and X. Huang, Phys. Rev. D. 91, 084011 (2015).

[24] D. Baumann, G. Bertone, J. Stout and G. M. Tomaselli, Phys. Rev. Lett. 128, 221102 (2022).

[25] L. Comisso and F. A. Asenjo, Phys. Rev. D. 103, 023014 (2021).

[26] N. Aghanim *et al.*, (Planck), Astron. Astrophys. 641, A1 (2020); Astron. Astrophys. 641, A6 (2020).

[27] A. Arbey and F. Mahmoudi, Prog. Part. Nucl. Phys. 119, 103865 (2021).

[28] M. Misiaszek and N. Rossi, arXiv:2310.20472.

[29] J. Hecht, Nature. 537, S194 (2016).

[30] A. M. Green, JCAP. 10, 034 (2010).

[31] A. Hryczuk, E. Karukes, L. Roszkowski and M. Talia, JHEP. 07, 081 (2020).

[32] J. Liu, X. Chen and X. Ji, Nature Phys. 13, 212 (2017).

[33] J. Billard, *et al.*, Rept. Prog. Phys. 85, 056201 (2022).

[34] J. F. Navarro, C. S. Frenk, S. D. M. White, ApJ. 462, 563, (1996).

[35] S. Cole and C. Lacey, MRNAS. 281, 716 (1996).

[36] R. G. Carlberg, ApJ. 485, L13 (1997).

[37] R. Wojtak, E. Lokas, S. Gottlöber, G. Mamon, MNRAS. 361, L1 (2005).

[38] J. E. Taylor and J. F. Navarro, ApJ. 563, 483 (2001).

[39] S. H. Hansen, B. Moore, M. Zemp and J. Stadel, JCAP. 01, 014 (2006).

[40] J. F. Navarro *et al.*, MNRAS. 402, 21 (2010)

[41] T. Padmanabhan, Physics Reports. 188, 285 (1990).

[42] T. Padmanabhan, MNRAS. 278, L29 (1996).

[43] P. He, D. B. Kang, MNRAS. 406, 2678 (2010).

[44] J. Sánchez Almeida, Universe 8, 214 (2022).

[45] M. Vogelsberger *et al.*, MNRAS. 395, 797 (2009).

[46] M. Kuhlen *et al.*, JCAP. 1002, 030 (2010).

[47] F. S. Ling, E. Nezri, E. Athanassoula and R. Teyssier, JCAP. 1002, 012 (2010).

[48] M. Fairbairn and T. Schwetz, JCAP. 0901, 037 (2009).

[49] S. W. Hawking, R, Penrose, *The Nature of Space and Time*, Princeton University Press, (1996).

[50] D. Clowe, A. Gonzalez and M. Markevitch, Astrophys. J. **604** 596 (2004).

[51] M. Markevitch *et al.*, Astrophys. J. **606** 819 (2004).

[52] M. Bradac *et al.*, Astrophys. J. **687** 959 (2008).

[53] B. P. Abbott *et al.*, (LIGO Scientific, Virgo), Phys. Rev. D. 100, 104036 (2019).

[54] B. P. Abbott *et al.*, (LIGO Scientific, Virgo), Phys. Rev. Lett. 119, 161101 (2017).

[55] K. Akiyama *et al.*, (Event Horizon Telescope), 2022a, Astrophys. J. Lett. 930, L15.

[56] N. Birrell and P. Davies, Quantum Fields in Curved Space, (Cambridge Univ. Press, Cambridge, UK, (1984).

[57] A. G. Riess, et al, Astron.J. 116, 1009 (1998).

[58] S. Perlmutter, *et al.*, (Supernova Cosmology Project), Astrophys.J. 517, 565 (1999).

[59] S. M. Carroll, Living Rev. Rel. 4, 1 (2001).

[60] J. M. Bardeen, in Conference Proceedings of GR5, Tbilisi, USSR. 174, (1968).

[61] E. Ayon-Beato, A.Garcia, Gen. Relativ. Gravity. 37, 635 (2005).

[62] L. Balart, E.C. Vagenas, Phys. Rev. D. 90, 124045 (2014).

[63] C. Bambi, L. Modesto, Phys. Lett. B. 721, 329 (2013).

[64] L. Modesto, P. Nicolini, Phys. Rev. D. 82, 104035 (2010).

[65] M. R. Brown, Quantum Gravity 2*. 439 (1980).

[66] A. H. Guth, Phys. Rev. D. 23, 347 (1981).

[67] A. D. Linde, Phys. Lett. B. 108, 389 (1982).

[68] A. Albrecht and P. J. Steinhardt, Phys. Rev. Lett. 48, 1220 (1982).

[69] R. R. Caldwell, R. Dave, and P. J. Steinhardt, Phys. Rev. Lett. 80, 1582 (1998).

[70] E. G. M. Ferreira, Astron. Astrophys. Rev. 29, 7 (2021).

[71] R. Brito, V. Cardoso, and P. Pani, Lect. Notes Phys. 906, 237 (2015).

[72] W. East, Phys. Rev. Lett. 121, 131104 (2018).

[73] A. Arvanitaki, *et al.*, Phys.Rev.D. 91, 084011 (2015).

[74] R. C. F. Hugo, A. R. H. Carlos, Phys. Rev. D. 97, 084003 (2018).

[75] T. Kolyvaris, M. Koukouvaou, A. Machattou and E. Papantonopoulos, Phys. Rev. D. 98, 024045 (2018).

[76] V. P. Frolov and A. Zelnikov, Phys. Rev. D. 98, 084035 (2018).

[77] M. F. Wondrak, P. Nicolini and J. W. Moffat, JCAP 12, 021 (2018).

[78] K. Destounis, Phys. Rev. D. 100, 044054 (2019).

[79] M. Khodadi, A. Talebian and H. Firouzjahi, arXiv:2002.10496.

[80] E. Franzin, S. Liberati and M. Oi, Phys.Rev.D. 103, 104034 (2021).

[81] M. Khodadi, Phys. Rev. D. 103, 064051 (2021).

[82] W. X. Chen and Y. G. Zheng, arXiv:2103.04239.

[83] B. Cuadros-Melgar, R. D. B. Fontana and J. de Oliveira, Phys. Rev. D. 104, 104039 (2021).

[84] M. Khodadi and R. Pourkhodabakhshi, Phys. Lett. B. 823, 136775 (2021).

[85] M. G. Richarte, É. L. Martins and J. C. Fabris, Phys. Rev. D. 105, 064043 (2022).

[86] S. Alexander, G. Gabadadze, L. Jenks and N. Yunes, arXiv:2201.02220.

[87] G. Mascher, K. Destounis, K. D. Kokkotas, Phys. Rev. D. 105, 084052 (2022).

[88] T. Ishii, Y. Kaku and K. Murata, JHEP 10, 024 (2022).

[89] S. K. Jha and A. Rahaman, arXiv:2208.13176.

[90] H. Yang and Y. G. Miao, arXiv:2211.15130.

[91] R. Penrose and R. M. Floyd, Nature Phy. 229, 177 (1971).

[92] T. Piran, J. Shaham, and J. Katz, Astrophys. J. Lett. 196, L107 (1975).

[93] R. D. Blandford and R. L. Znajek, MNRAS. 179, 443 (1977).

[94] M. Khodadi, Phys. Rev. D. 105, 023025 (2022).

[95] S. W. Wei, H. M. Wang, Y. P. Zhang and Y. X. Liu, JCAP 04, 050 (2022).

[96] E. Franzin, S. Liberati, J. Mazza, R. Dey and S. Chakrabort, Phys. Rev. D. 105, 124051 (2022).

[97] M. Khodadi and R. Pourkhodabakhshi, Phys. Rev. D. 106, 084047 (2022).

[98] R. Ghosh, M. Rahman and A. K. Mishra, arXiv:2209.12291.

[99] R. A. Konoplya, *et al.*, Phys. Rev. D. 97, 084044 (2018).

[100] S. A. Teukolsky, Astrophys. J. 185, 635 (1973).

[101] A. Starobinski, Zh. Eksp. Teor. Fiz. 64, 48 (1973).

[102] A. Starobinski and S. M. Churilov, Zh. Eksp. Teor. Fiz. 65, 3 (1973).

[103] K. D. Kokkotas and B. G. Schmidt, Living Rev. Rel. 2, 2 (1999).

[104] E. Berti, V. Cardoso and A. O. Starinets, Class. Quant. Grav. 26, 163001 (2009).

[105] R. A. Konoplya and A.V. Zhidenko, Rev. Mod. Phys. 83, 793 (2011).

[106] P. H. C. Siqueira and M. Richartz, Phys. Rev. D. 106, 024046 (2022).

[107] A. K. Mishra, A. Ghosh and S. Chakraborty, Eur. Phys. J. C. 82, 820 (2022).

[108] R. G. Daghigh, M. D. Green and J. C. Morey, arXiv:2209.09324.

[109] E. W. Leaver, Proc. Roy. Soc. Lond. A 402, 285 (1985).

[110] H. P. Nollert, Phys. Rev. D. 47, 5253 (1993).

[111] R. A. Konoplya and A. V. Zhidenko, Phys. Rev. D. 73, 124040 (2006).

[112] S. R. Dolan, Phys. Rev. D. 76, 084001 (2007).

[113] C. A. R. Herdeiro, E. Radu, Int. J. Mod. Phys. D. 24, 1542014 (2015).

[114] J. Ovalle, Phys. Rev. D. 95, 104019 (2017).

[115] J. Ovalle, Phys. Lett. B. 788, 213 (2019).

[116] S. U. Islam, S. G. Ghosh, Phys. Rev. D. 103 124052 (2021).

[117] M. Afrin, R. Kumar and S. G. Ghosh, MNRAS. 504, 5927 (2021).

[118] R. T. Cavalcanti, R. C. de Paiva and R. da Rocha, Eur. Phys. J. Plus 137, 1185 (2022).

[119] S. Vagnozzi, *et al.*, arXiv:2205.07787.

[120] S. K. Jha and A. Rahaman, arXiv:2205.06052.

[121] S. Mahapatra and I. Banerjee, arXiv:2208.05796.

[122] J. Abadie, *et al.*, Phys. Rev. D. 83, 122005 (2011).

[123] O. Dreyer, *et al.*, Class. Quantum Grav. 21, 787 (2004).

[124] R. Roy, S. Vagnozzi and L. Visinelli, Phys. Rev. D. 105, 083002 (2022).

[125] Y. Chen, R. Roy, S. Vagnozzi and L. Visinelli, Phys. Rev. D. 106, 043021 (2022).

[126] E. Franzin, S. Liberati, J. Mazza, R. Dey and S. Chakraborty, Phys. Rev. D. 105, 124051 (2022).

[127] R. Dey, S. Biswas and S. Chakraborty, Phys. Rev. D. 103, 084019 (2021). H. Yang and Y. G. Miao, arXiv:2211.15130.

[128] Zeldovich, JETP Lett. 14, 180 (1971); JETP 35, 1085 (1972);

[129] T. Torres, etc, Nature Phys. 13, 833 (2017).

[130] M. C. Braidotti,etc, Phys. Rev. Lett. 128, 013901 (2022).

[131] Zhen Li, Phys.Rev.D. 107 044013 (2023).

[132] A. L. Dudley and J. D. Finley, III, J. Math. Phys. 20, 311 (1979).

[133] K. D. Kokkotas, Nuov Cim B. 108, 991 (1993).

[134] E. Berti and K. D. Kokkotas, Phys. Rev. D. 71 (2005), 124008.

[135] R. Brito, V. Cardoso and P. Pani, Class. Quant. Grav. 32, 134001 (2015).

[136] M. Abramowitz and I. A. Stegun, Handbook of Mathematical Functions with Formulas, Graphs, and Mathematical Tables, New York, (1965).

[137] D. N. Page, Phys.Rev. D. 13, 198 (1976).

[138] D. N. Page, Phys. Rev. D. 13, 198 (1976).

[139] E. Berti, V. Cardoso and C. M. Will, Phys. Rev. D. 73, 064030 (2006).

[140] S. W. Hawking and R. Penrose, Proc. Roy. Soc. Lond. A. 314, 529 (1970).

[141] S. Hayward, Phys. Rev. Lett. 96, 031103 (2006).

[142] C. Lan, H. Yang, Y. Guo, and Y.-G. Miao, arXiv:2303.11696v2.

[143] X. Li, Y. Ling, and Y.-G. Shen, Int. J. Mod. Phys. D. 22, 1342016 (2013).

[144] H. Culetu, J. Phys.: Conf. Ser. 845, 012006 (2017).

[145] H. Culetu, Int. J. Mod. Phys. D. 31, 2250124 (2022).

[146] H. Culetu, Phys. Lett. B. 839, 127775 (2023).

[147] C. Bambi and L. Modesto, Phys. Lett. B. 721, 329 (2013).

[148] M. Amir and S. G. Ghosh, Phys. Rev. D. 94, 024054 (2016).

[149] R. Kumar and S. G. Ghosh, Class. Quant. Grav. 38, 8 (2021).

[150] R. Kumar, A. Kumar and S. G. Ghosh, Astrophys. J. 896, 89 (2020).

[151] F. Sarikulov, F. Atamurotov, A. Abdujabbarov, and B. Ahmedov, Eur. Phys. J. C 82, 771 (2022).

[152] Z. Li, Phys. Rev. D. 107, 044013 (2023).

[153] W. Daughton, V. Roytershteyn, B. Albright, H. Karimabadi, L. Yin, and K. J. Bowers, Phys. Rev. Lett. 103, 065004 (2009).

[154] A. Bhattacharjee, Y.-M. Huang, H. Yang, and B. Rogers, Phys. Plasmas 16, 112102 (2009).

[155] K. Parfrey, A. Philippov and B. Cerutti, Phys. Rev. Lett. 122, 035101 (2019).

[156] S. S. Komissarov, Mon. Not. Roy. Astron. Soc. 359, 801 (2005).

[157] B. Ripperda, F. Bacchini and A. Philippov, Astrophys. J. 900, 100 (2020).

[158] A. Bransgrove, B. Ripperda and A. Philippov, Phys. Rev. Lett. 127, 055101 (2021).

[159] L. Comisso, M. Lingam, Y.-M. Huang, and A. Bhattacharjee, Phys. Plasmas 23, 100702 (2016)

[160] D. A. Uzdensky and N. F. Loureiro, Phys. Rev. Lett. 116, 105003 (2016)

[161] L. Comisso, M. Lingam, Y.-M. Huang, and A. Bhattacharjee, Astrophys. J. 850, 142 (2017).

[162] S. Koide and K. Arai, Aprophys. J. 682, 1124 (2008).

[163] R. Penrose and R. M. Floyd, Nature. 229, 177 (1971).

[164] T. Piran, J. Shaham, and J. Katz, Astrophys. J. Lett. 196, L107 (1975).

[165] R. D. Blandford and R. L. Znajek, MNRAS. 179, 433 (1977).

[166] S. W. Wei, H. M. Wang, Y. P. Zhang, and Y. X. Liu, JCAP 04, 050 (2022).

[167] W. Liu, Astrophys. J. 925, 149 (2022).

[168] M. Khodadi, Phys. Rev. D. 105, 023025 (2022).

[169] A. Carleo, G. Lambiase, and L. Mastrototaro, Eur. Phys. J. C 82, 776 (2022).

[170] C. H. Wang, C. Q. Pang and S. W. Wei, Phys. Rev. D. 106, 124050 (2022).

[171] J. M. Bardeen, W. H. Press, and S. A. Teukolsky, Astrophys. J. 178, 347 (1972).

[172] F. A. Asenjo and L. Comisso, Phys. Rev. Lett. 118, 055101 (2017).

[173] Y.-H. Liu, M. Hesse, F. Guo, W. Daughton, H. Li, P. A. Cassak, and M.A. Shay, Phys. Rev. Lett. 118, 085101 (2017).

[174] L. Comisso and A. Bhattacharjee, J. Plasma Phys. 82, 595820601 (2016).

[175] L. Comisso and L. Sironi, Astrophys. J. 886, 122 (2019).

[176] D. A. Uzdensky, N. F. Loureiro, and A. A. Schekochihin, Phys. Rev. Lett. 105, 235002 (2010).

[177] L. Comisso and D. Grasso, Phys. Plasmas 23, 032111 (2016).

[178] D. Macdonald and K. S. Thorne, MNRAS. 198, 345 (1982).

[179] K. S. Thorne, R. H. Price, and D. A. MacDonald, Black Holes: The Membrane Paradigm (Yale University, New Haven, CT, 1986).

[180] S. S. Komissarov, MNRAS. 326, L41 (2001).

[181] A. Tchekhovskoy, R. Narayan, and J. C. McKinney, Astrophys. J. 711, 50 (2010).

[182] Filippo Camilloni *et al.*, JCAP 07, 032 (2022).

[183] Z. Li, Phys. Lett. B. 841, 137902 (2023).

[184] V. Vertogradov and D. Kudryavcev, arXiv:2303.01413.

[185] Z. Li, X. K. Guo and F. Yuan, arXiv:2304.08831.

[186] M. Vogelsberger, F. Marinacci, P. Torrey and E. Puchwein, Nature Rev. Phys. 2, 42 (2020).

[187] R. E. Angulo, O. Hahn, Living Rev Comput Astrophys. 8, 1 (2022).

[188] B. Moore, F. Governato, T. Quinn, J. Stadel, G. Lake, ApJ. 499, 5 (1998).

[189] J. Diemand, B. Moore, J. Stadel, MNRAS. 353, 624 (2004).

[190] Y. P. Jing, ApJ. 535, 30 (2000).

[191] Dan Coe, arXiv:1005.0411

[192] C. O. Wright and T. G. Brainerd, ApJ. 534 34 (2000).

[193] H. S. Dúmet-Montoya, G. B. Caminha, and M. Makler, A&A 560, A86 (2013).

[194] H. Haghi, A. Khodadadi, A. Ghari, A. H. Zonoozi and P. Kroupa, MNRAS 477, 4187 (2018).

[195] M. G. Aartsen *et al.*, [IceCube], Eur. Phys. J. C 77, 627 (2017).

[196] A. S. Eddington, MNRAS, 76, 572 (1916).

[197] T. Lacroix, M. Stref and J. Lavalle, JCAP. 09, 040 (2018).

[198] S. H. Hansen, D. Egli, L. Hollenstein and C. Salzmann, New Astron. 10, 379 (2005).

[199] S. H. Hansen, M. Sparre, APJ. 75 100 (2012).

[200] A. Eilersen A, S. H. Hansen, X. Zhang, MNRAS. 467, 2061 (2017).

[201] L. Beraldo e Silva, G. A. Mamon, M. Duarte, R. Wojtak, S. Peirani and G. Boué, MNRAS. 452, 944 (2015).

[202] I. R. King, Astron. J. 71, 64 (1966).

[203] M. Lisanti, L. E. Strigari, J. G. Wacker and R. H. Wechsler, Phys. Rev. D. 83, 023519 (2011).

[204] Y. Y. Mao, L. E. Strigari, R. H. Wechsler, H. Y. Wu and O. Hahn, Astrophys. J. 764, 35 (2013).

[205] T. M. Callingham, M. Cautun, A. J. Deason, C. S. Frenk, R. J. J. Grand, F. Marinacci, R. Pakmor, MNRAS. 495, 12 (2020).

[206] N. Bozorgnia *et al.*, JCAP 05, 024 (2016).

[207] M. Fairbairn and T. Schwetz, JCAP 01, 037 (2009).

[208] P. Bhattacharjee, S. Chaudhury, S. Kundu and S. Majumdar, Phys. Rev. D. 87, 083525 (2013).

[209] S. Mandal, S. Majumdar, V. Rentala and R. Basu Thakur, Phys. Rev. D. 100, no.2, 023002 (2019).

[210] B. J. Kavanagh and A. M. Green, Phys. Rev. Lett. 111, no.3, 031302 (2013).

[211] S. K. Lee, JCAP. 03, 047 (2014).

[212] B. J. Kavanagh, JCAP. 07, 019 (2015).

[213] J. Binney, S. Tremaine, Galactic Dynamics, Princeton University Press, Princeton, NJ, USA (2008).

[214] R. Wojtak, *et al.*, MNRAS. **388**, 815 (2008).

[215] J. Hjorth, L. L. R. Williams, APJ. 722, 851 (2010).

[216] L. L. R. Williams, J. Hjorth, APJ. 722, 856 (2010).

[217] L. Posti, J. Binney, C. Nipoti, L. Ciotti, MNRAS, 447, 3060 (2015).

[218] T. Piffl, Z. Penoyre and J. Binney, MNRAS, 451, 639 (2015).

[219] J. Binney, E. Vasiliev, MNRAS, 520, 1832 (2023).

[220] L. Osipkov, Soviet Astronomy Letters 5, 42–44 (1979).

[221] D. Merritt, Astron. J. 90, 1027 (1985).

[222] W. Dehnen and D. McLaughlin, MNRAS. 363, 1057 (2005).

[223] C. G. Austin *et al.*, Astrophys. J. 634, 756 (2005).

[224] K. B. Schmidt, S. H. Hansen and A. V. Maccio', Astrophys. J. Lett. 689, L33 (2008).

[225] V. Springel, *et al.*, MNRAS. 391, 1685 (2008)

[226] M. Sparre and S. H. Hansen, JCAP. 10, 049 (2012)

[227] H. Zhu, J. L. Ripley, A. Cárdenas-Avendaño and F. Pretorius, Phys. Rev. D. 109, 044010 (2024).

[228] G. Lingetti, arXiv:2309.15246.

[229] H. Roussille, D. Langlois and K. Noui, JCAP. 01, 054 (2024).

[230] J. R. Weaver and K. Horne, MNRAS. 512, 899 (2022).